Preparation and Characterization of Tungsten Tips Suitable for Molecular Electronics Studies

Anne-Sophie Lucier
Center for the Physics of Materials
Department of Physics
McGill University
Montréal, Québec
Canada
February 2004

A thesis submitted to McGill University
in partial fulfillment of the requirements of the degree of
Master of Science

Contents

List of Figures

List of Tables

Abstract

A technique for preparing tips with a radius of a few nanometers from tungsten wire is investigated. The sharp shape is obtained by electrochemical etching; further tip processing and characterization is done in ultra-high vacuum. Tips are cleaned through a high temperature annealing process and their sharpness can be quickly estimated from their field emission behaviour. Sufficiently sharp tips are imaged with a field ion microscope; full atomic characterization of the tip apex can be obtained from an analysis of the resulting images and field evaporation can be used to atomically engineer the tip apex into a desired configuration. Starting from single crystal, (111) oriented tungsten wire, a sharp tip terminating in three atoms can be fabricated; due to its geometry and its stability, this apex configuration is well suited for applications as an atomically defined electrical contact in a single molecule conductivity experiment.

Résumé

Une méthode servant à préparer des pointes de quelques nanomètres de rayon à partir d'un fil de tungstène est étudiée. La forme effilée est obtenue par attaque électrolytique et les traitements additionnels sont effectués en ultravide. Les pointes sont nettoyées par chauffage et la finesse de leur sommet peut être facilement estimée à partir de leur comportement en émission de champ. Les pointes suffisamment aiguës sont observées avec un microscope ionique et une analyse des images obtenues permet une caractérisation de leur apex à l'échelle atomique. De plus, le phénomène d'évaporation par effet de champ peut être utilisé pour sculpter, atome par atome, la structure de l'apex. À partir d'un fil de tungstène monocristallin d'orientation (111), une pointe ayant trois atomes à son sommet peut être fabriquée; grâce à la géométrie et à la stabilité de son apex, cette pointe peut servir de contact électrique bien défini dans une expérience visant à mesurer la conductibilité d'une molécule.

Acknowledgments

I would like to thank my supervisor, Dr. Peter Grütter, for presenting me with the opportunity to work on this project in such a stimulating research environment. I am very grateful to him for his advice and guidance, and for his unfailing enthusiasm.

This work would not have been possible without the help of Dr. Henrik Mortensen and Yan Sun, my research partners. Their patience when explaining to me how to run our complex ultra-high vacuum system was very much appreciated. Discussing novel ideas and experimental challenges with them was a pleasure.

I am indebted to Mark Orchard-Webb for the time he spent helping me with the three dimensional atom by atom reconstruction of the tips from my FIM images. His programming expertise and the interest he showed in my work were invaluable to me. Special thanks also go to Robert Gagnon for his assistance in acquiring SEM images.

Furthermore, I would like to acknowledge financial support from NSERC through a Postgraduate Scholarship.

Finally, thanks to the other members of the SPM research group for providing a pleasant working atmosphere, and to my friends in the physics department, in particular Josianne Lefebvre, Mark Orchard-Webb, Julie Lainesse, Marc Saint-Laurent, Sophie Avesque, Alexis Gagnon-Morris and Sebastian Gliga, for making my graduate studies so much more enjoyable. I am grateful to Mark Roseman for being so encouraging and caring even thousands of kilometers away, to Pierrette Lucier-Marquis for her unparalleled thoughtfulness and kindness, and to my parents for their faithful love and support.

1

Introduction

Since the birth of the transistor at Bell Labs in the 1940's, tremendous efforts and resources have been devoted to producing new generations of semiconductor devices which are smaller, faster and cheaper than their predecessors. However, this continual miniaturization is quickly reaching an imposing limit; semiconductor devices below 10 nm require prohibitively expensive fabrication techniques and exhibit quantum effects which dramatically alter their desired electronic properties. In response to these issues, an increasing amount of attention has been paid to the emerging field of molecular electronics [4–6]. This novel technology seeks to utilize individual molecules as building blocks for nanometer sized electrical circuits. At this scale, the laws of physics and chemistry merge, and quantum properties rule. Developing a comprehensive understanding of this strange new world and successfully exploiting its resources could lead to great technological and scientific advances.

A crucial first step in the development of such molecular structures is a systematic study of the electrical properties of single molecules. To achieve this ambitious research goal, fine electrical contacts must be attached to each end of a molecule so that the electrical behaviour of the molecule at the nanoscopic level can be recorded and examined from the macroscopic world; however, wiring a single molecule into an electrical circuit represents a significant challenge due to the small size of the components involved. Many studies on the electrical properties of molecules have been conducted over the past few years and techniques employing break junctions, scanning probe tips, nanopores, electron beam deposition and nanolithography have been developed to electrically contact a single molecule or a molecular monolayer [4, 7–

10]. Since discrepancies exist between reported conductivities for identical molecules, and since these conductivities disagree with theoretical calculations of electron transport in similar nanoscopic systems by several orders of magnitude, it is believed that the observed electrical properties of such molecular devices are not inherent to the molecule itself, but are rather determined by the nature of the molecule-electrode junction [8, 9]. To gain insight into the electrical properties of single molecules, it is thus necessary to devise an experiment in which the geometry of the molecular device is well defined at the atomic level; using atomically characterized electrodes to contact a molecule can then lead to a meaningful comparison with theoretical predictions on single molecule conductivity [10, 11].

In order to understand the electrical behaviour of single molecules, we propose to measure the conductivity of a well defined two-terminal molecular device using a combined scanning tunneling microscope (STM), atomic force microscope (AFM) and field ion microscope (FIM) in an ultra-high vacuum (UHV) environment. As illustrated in figure 1.1, the STM tip plays the role of the top electrode, while the bottom electrode is provided by an atomically flat metallic surface evaporated onto a flexible cantilever beam. The investigated molecule sits on the metallic substrate, and the STM tip can be carefully brought into contact with the molecule through the action of a piezo tube; by applying a voltage to the tip, the current flowing through the molecule can be detected. Since a laser beam probes the deflection of the cantilever beam, the force exerted on the molecule by the tip can be recorded by AFM techniques; electromechanical measurements on the molecule can thus also be performed. As shown in figure 1.1, the chief advantage of this combined STM/AFM/FIM setup is that the tip apex can be atomically characterized by FIM imaging prior to its use in a single molecule conductivity experiment since, thanks to piezoelectric motors, the AFM sample stage can be quickly retracted, thus exposing a screen on which the FIM image of the tip apex can be observed. Once the geometry of the top electrode is well defined, the microscope can switch back to the STM/AFM configuration; the tip then locates a single molecule on the substrate in STM imaging mode before mea-

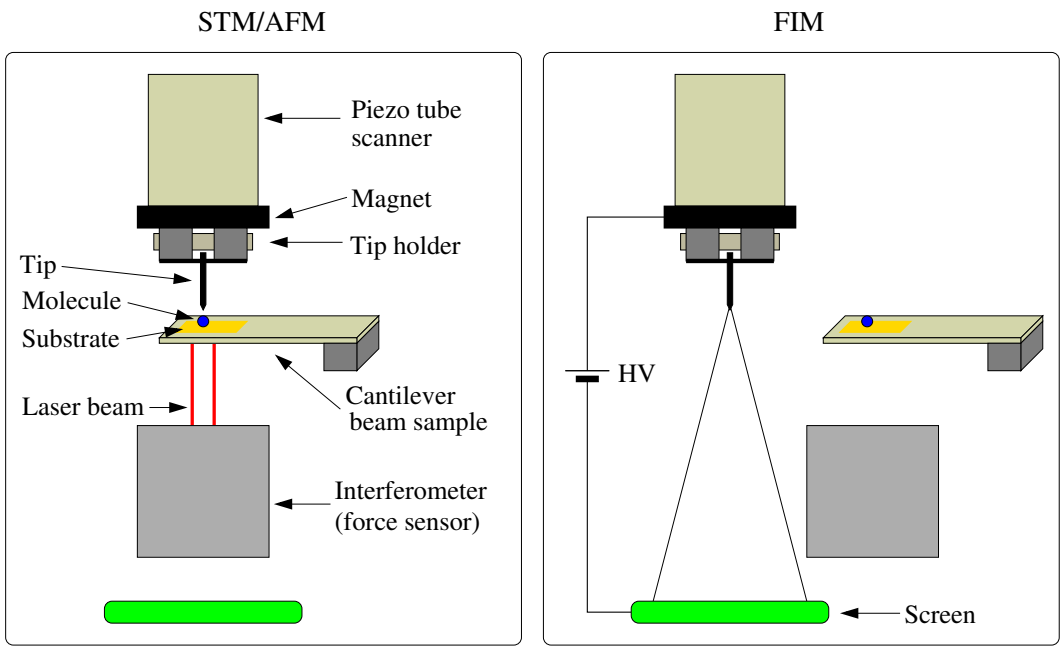

Figure 1.1: Schematic representation of our combined UHV STM/AFM/FIM system. Using piezoelectric motors, the sample stage can be quickly retracted to switch from the STM/AFM mode to the FIM mode. With this unique setup, single molecule conductivity measurements can be performed in the STM/AFM mode using a tip which can be atomically characterized in the FIM mode. (This drawing was adapted from [1].)

suring its electrical properties in AFM/STM spectroscopic mode. Initial experiments will use the C_{60} molecule, as this fullerene has already been extensively studied, and a gold (111) substrate, since nice large atomically flat terraces can be obtained by evaporation. The top electrode will consist in an atomically defined tungsten tip, since tungsten tips are relatively easy to prepare and are stiff enough to withstand the mechanical stress imposed by the high electrical fields which prevail during FIM imaging.

This thesis discusses the various steps involved in the preparation and characterization of a suitable top electrode for our two-terminal molecular device. Since the tungsten tip will be used for STM imaging as well as for probing electrical properties of a single molecule, the main requirements for this electrode are the following: it should be very sharp and free of contamination, it should have an atomically stable apex and

it should be fully structurally characterized before being brought into contact with the molecule. A tip fabrication technique fulfilling these requirements has been developed and several tip characterization tools have been explored to assess the success of the preparation process; the various results obtained on polycrystalline tungsten tips and on single crystal, (111) oriented tungsten tips are presented throughout this thesis.

The description of the preparation and characterization of our tungsten tips is divided in three chapters. The formation of a sharp tip shaped electrode through the electrochemical etching of a cylindrical tungsten wire is explained in chapter 2, along with a discussion on how a high temperature annealing treatment in UHV can effectively clean the surface of a freshly etched tip; some attention is also given to the consequences of this annealing treatment on the tip apex shape. Once the tip is annealed in UHV, it is possible to verify its sharpness and to estimate its apex radius by monitoring *in situ* its field emission characteristics; such analysis is the focus of chapter 3. Finally, the tips which reveal a sharp enough apex during field emission measurements can be transferred to the UHV STM/AFM/FIM chamber, where the atomic structure of their apex can be observed with the microscope in FIM mode. Chapter 4 provides a detailed description of the working principle and capabilities of the FIM and demonstrates how the analysis of FIM images can lead to a full atomic characterization of the tip apex. Since FIM also allows the removal of individual atoms from the tip apex surface by field evaporation, ultimate control on the electrode apex shape can be achieved; such engineering of the apex into an atomic configuration which is optimal for molecular electronics studies is illustrated in chapter 4.

2

Preparation of Tungsten Tips

Although there exist various well defined techniques for preparing suitable STM and FIM tips, it appears that the mastering of tip fabrication remains an art more than a science. It is considered to be one of the trickiest steps in the realization of a successful STM experiment, as one can often blame the tip when faced with lousy images. Ideally, an STM tip should be extremely sharp, possibly terminating in a single atom, in order to resolve details at the atomic level; it should have a small aspect ratio to reduce mechanical vibration while scanning, have a stable atomic configuration at its apex to yield reliable and reproducible images, and be clean to ensure a stable tunnel junction, since the presence of contaminants like oxides or etching byproducts could alter its metallic behaviour. As will be discussed in chapter 4, the specifics of our FIM setup enforce the sharpness requirement for our tips; only tips with an apex radius of a few nanometers will produce a FIM image, and will thus be atomically characterized and engineered. This chapter will provide a detailed explanation of the method employed to prepare our tips, from the electrochemical etching to the annealing in UHV, along with a survey of the various problems encountered and an overview of other existing tip preparation techniques.

2.1 Electrochemical Etching : From a Wire to a Tip

Electrochemical etching of a metal wire is a routinely used technique to generate good STM tips. The basic idea is to dip a small diameter metal wire into an electrolyte solution in which a counter electrode is sitting and to apply a AC or DC voltage

between these two electrodes until enough dissolution of the wire has happened so that it displays a sharp tip shape. The choice of the electrolyte and of the voltage applied depends on the material used to make the tip; convenient tables regrouping this information can be found in references [3, 12–14]. Many other techniques exist to prepare STM tips; a quick overview of these will be presented in section 2.1.5.

Among the reasons why tungsten (W) is such a popular material for the production of STM tips is that an extremely sharp tip can be obtained in a single electrochemical step using fairly mild chemicals. The drawback is that due to its poor resistance to oxidation, the tungsten tip will most likely undergo surface contamination; however, a proper annealing treatment in UHV can provide a quick and efficient solution to this problem (section 2.2).

2.1.1 Setting Up for the Electrochemical Etching

Our W tips were made from either a 0.1 mm diameter polycrystalline wire or a 0.13 mm diameter single crystal, (111) oriented wire. The differences between these two types of W tips will be discussed in detail in chapter 4. The first step involved in tip preparation is illustrated in figure 2.1. Two pieces of W wire must be cut: one about 1.5 cm long and the other about 4 mm long. The small piece, which

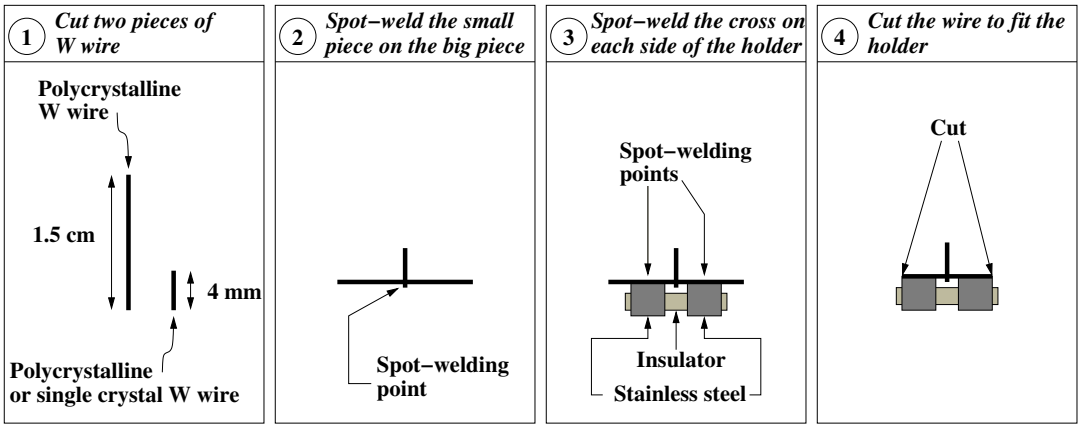

Figure 2.1: Instructions on how to mount the tip on the tip holder

will become the tip, has to be spot-welded onto the center of the bigger piece at a 90^o angle; the resulting cross will in turn be spot-welded on both electrically isolated sides of the tip holder, with the tip wire pointing up. Considering the very high cost of single crystal wire, one should always make sure to use polycrystalline wire for the bigger piece! Any wire protruding from the sides of the tip holder should be cut off. The overall length of the tip wire is quite critical, not for the etching itself, but for its use in the STM since the piezo tube controlling the approach of the tip towards the sample has a limited range of motion. Too short a tip will not reach the sample within a tunneling distance, and too long a tip will crash while scanning since the piezo will be incapable of following the sample's topography. A good rule of thumb is that if the tip length (once etched) is roughly equal to the height of the tip holder it is sitting on ($\sim$ 2.5 mm), then it will be appropriate for use in our STM.

The experimental setup we use for the electrochemical etching of our W tips is shown in figure 2.2. The tip holder is magnetically held onto the etching station

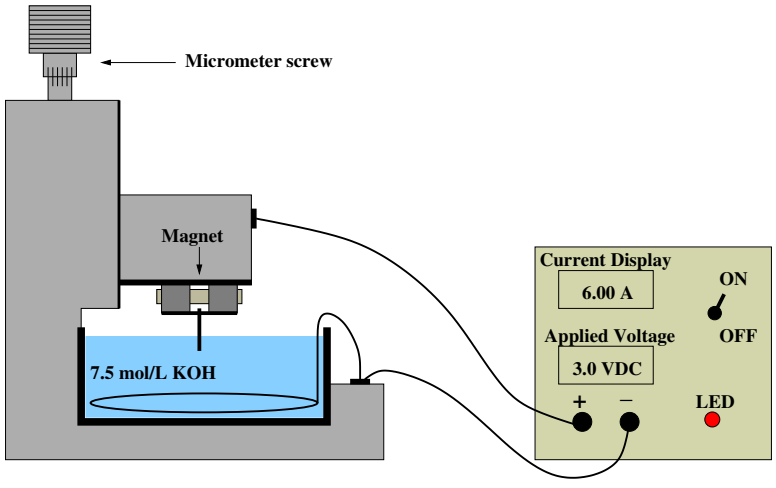

Figure 2.2: The electrochemical etching station

and can be moved vertically using a micrometer screw; it is thus possible to easily and precisely control the length of the wire immersed in the solution. We usually set this length to be 0.5 mm. The counter electrode is a loop of steel sitting at

the bottom of the solution container; however, other geometries such as a rod-like shape are also perfectly acceptable [15]. The most common electrolytes used for W etching are $NaOH$ and KOH; the community seems divided as to which one is best [3, 12–14, 16–18], but we used a freshly prepared 7.5 mol/L KOH solution, which yielded satisfying results. The tip and the counter electrode are connected to a controller which serves several purposes: it lights up an LED when the end of the tip wire touches the solution, which gives a convenient reference point from which the immersed length can be measured, it provides the bias voltage necessary to generate the etching reaction – in our case, we use 3.0 V_{DC} – and it monitors the current between the anode and the cathode in order to quickly switch off the voltage when the etching is completed. The latter point is extremely important, as the cut-off time of the etching circuit greatly affects the shape of the tip; this will be discussed later. Note that a large working distance optical microscope sits in front of the setup so that the tip etching can be carefully observed.

2.1.2 Understanding the Electrochemical Reaction

The overall reaction governing this particular electrochemical etching is the following [19]:

$$\textit{cathode}: \quad 6H_2O + 6e^- \rightarrow 3H_2(g) + 6OH^- \tag{2.1}$$

$$\textit{anode}: \quad \underline{W(s) + 8OH^- \rightarrow WO_4^{2-} + 4H_2O + 6e^-} \tag{2.2}$$

$$W(s) + 2OH^- + 2H_2O \rightarrow WO_4^{2-} + 3H_2(g) \tag{2.3}$$

The etching takes place at the air/electrolyte interface, and as one can learn from equation 2.2, the tungsten undergoes an oxidative dissolution to tungstate anions (WO_4^{2-}), which are soluble in water. However, the actual reaction is more complex than it appears [19]: the tungsten is first oxidized to intermediate tungsten oxides; these are in turn non-electrochemically dissolved to yield these soluble tungstate anions which show greatest stability in a basic medium. The reaction also involves the reduction of water; bubbles of gaseous hydrogen and OH^- ions are thus produced at the cathode (equation 2.1).

One can wonder how this reaction actually generates a tip shape out of a cylindrical wire. The explanation [19] roots in the fact that capillary forces yield the formation of a meniscus of solution around the tip wire when it is immersed into the electrolyte. The shape of the meniscus plays a very important role in determining the final shape of the tip as the etching rate at the top of the meniscus is a lot slower than at the bottom. This can be explained by the presence of a concentration gradient due to the diffusion of OH^- ions to the tip. Furthermore, the soluble tungstate produced during the reaction flows towards the lower end of the tip wire, generating a dense viscous layer which prevents this region from being etched away. Thus, a necking phenomenon is observed in the meniscus where the etching rate is enhanced. At some point, this part of the wire becomes so thin its tensile strength cannot sustain the weight of the lower end of the wire; the latter breaks off and a sharp tip is left behind. This is commonly referred to as the "drop-off" method, and it is illustrated in figure 2.3.

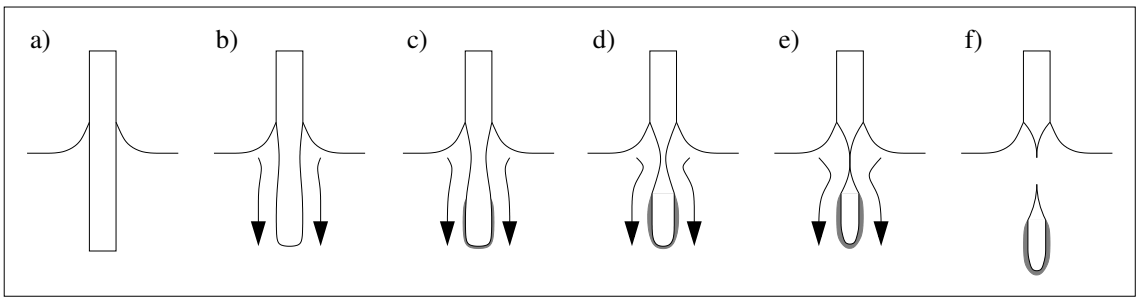

Figure 2.3: Illustration of the drop-off method. a) shows the formation of the meniscus. b) to e) illustrate the flow of WO_4^{2-} towards the lower end of the wire, the formation of a dense layer of WO_4^{2-} around the bottom of the wire and the necking phenomenon in the meniscus. In f), the lower part breaks off: the drop-off has occurred.

Once the etching is completed, it is imperative that the tip should be cleaned immediately by carefully dipping it for a few seconds in distilled water, and by rinsing it with acetone and ethanol. The purpose of this step is to remove residues left by the etching process. The tip should then be gently dried with clean compressed nitrogen gas.

2.1.3 Maximizing the Chances of Success

If the electrochemical etching is successful and followed by the cleaning procedure described above, the freshly made W tip observed under an optical microscope should resemble the tip presented in figure 2.4. It should reveal a smooth surface and have

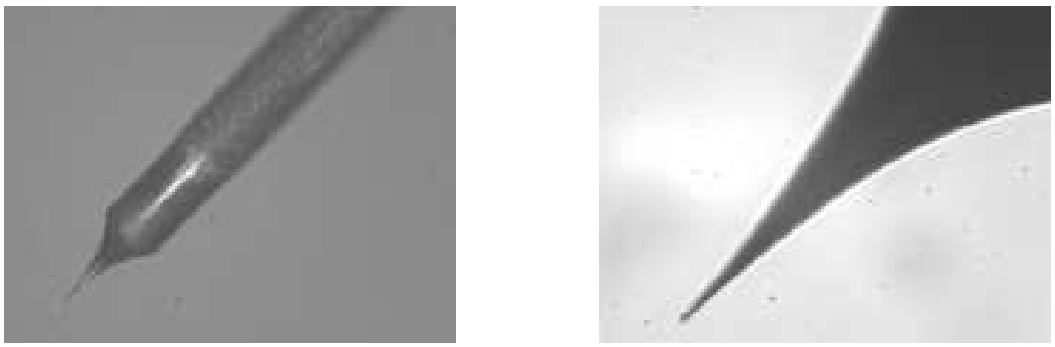

Figure 2.4: Freshly electrochemically etched tungsten tip observed under an optical microscope with a 10X magnification on the left and a 50X magnification on the right.

a very sharp end that cannot be resolved. Note that on the left image of figure 2.4, the part of the wire close to the tip appears more reflective than the rest of it. This is due to a pre-etching operation [20], during which 1 mm of the wire is immersed in the electrolyte and etched for 5 seconds, followed by the cleaning steps explained before. The pre-etching, while not removing a significant amount of material, leaves a much smoother and cleaner wire to etch; this seems to improve the quality and reproducibility of the subsequent "real" etching step [21] .

At this point, one must understand that not all etched tips will look as nice as the one shown in figure 2.4. Many times, the electrochemical etching does not go as smoothly as described above; in fact, about 40% of our freshly etched tips have to be discarded due to obvious gross flaws. To get a reasonable success rate, *many* factors have to be well controlled [19, 22]; the optimal etching conditions are discussed below.

The Etch Cut-Off Time

As was mentioned before, the time interval between the actual drop-off and the switching off of the circuit is crucial. Many authors agree to say that the longer this interval is, the more blunt the tip will become [19, 22–24]. This is because the electrochemical

reaction does not stop after the drop-off occurs, so if the applied voltage is not turned off right away, the sharp end of the tip will be etched away.

People have been concerned with this issue for many decades and have designed all kinds of electronic devices to minimize the switching off delay [19, 25–27]. They relied on the following principle: as the etching progresses, the current between the anode and the cathode decreases in a linear manner since the cross-sectional area of the wire decreases, but when the drop-off happens, the current falls abruptly, reflecting the loss of an considerable amount of material at the anode. These electronic devices thus monitor the current (or the differential signal of the current [26]), and switch off the circuit when a sudden drop in the current is detected. In our case, the current is usually between 4 and 9 A at the beginning of the etching process and decreases steadily until it reaches about 1.5 A, at which point the drop off happens and the circuit switches off. The whole etching operation requires a couple of minutes. Of course, the magnitude of the current and the etching time vary with the applied voltage, the diameter of the wire, the length of wire immersed in solution and the electrolyte concentration.

A smart alternative solution to this time delay issue would be to design the etching station in such a way that the part of the wire that drops off can be rescued and used as the tip [28]. As can be seen from figure 2.3, two tips are actually produced. The advantage of using the lower one is that it disconnects from the circuit as soon as it drops, so there is no need to worry about over-etching it and thus no need for an automatic shutting off system.

The Shape of the Meniscus

The discussion surrounding figure 2.3 made it clear that the meniscus shape directly influences the tip shape. The shorter the meniscus, the smaller the aspect ratio of the resulting tip and a small aspect ratio is desirable to limit the vibration of the tip in a STM experiment [16, 19, 26, 28]. Note that it is possible to fine tune the height of the meniscus before starting the etching reaction by carefully playing with the micrometer screw.

One can also imagine that a symmetric meniscus will yield a symmetric tip. This is achieved when the angle between the immersed wire and the air/electrolyte interface is close to 90^o (see figure 2.2). However, this is not an easy task; lots of practice is required to be able to mount the tip wire truly perpendicularly onto the tip holder (figure 2.1). Figure 2.5 shows scanning electron microscope (SEM) images of two tips etched at different angles with respect to the air/electrolyte interface. The left image shows a tip etched perpendicularly to the liquid surface and its shape exhibits remarkable symmetry, while the tip in the right image illustrates the effect of an asymmetric meniscus. It would be preferred to etch the tip symmetrically, since

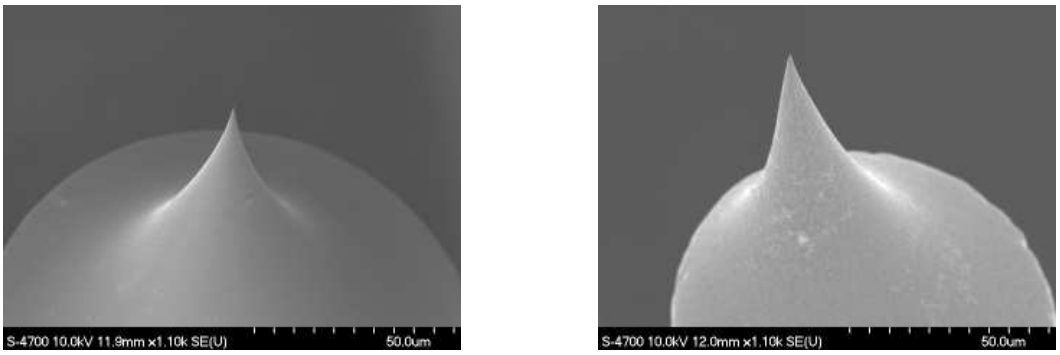

Figure 2.5: SEM images showing the effect that the symmetry of the meniscus has on the tip shape. Left: tip obtained from a symmetric meniscus. Right: tip obtained from an asymmetric meniscus.

asymmetric etching will result in lateral forces at the breaking point, which may lead to undesired phenomena such as bending of the tip near the apex.

Perhaps the most problematic issue we encountered was to make sure the shape of the meniscus would stay intact while the wire was being etched. Our experiments revealed that if the meniscus gets destroyed during the process, the drop-off will most likely not occur and some oddly shaped wire will result. An obvious first precaution to take is to keep the solution as vibration free as possible [22]; to this end, our etching station was sitting on a toroidal air bladder.

As demonstrated in equation 2.1, hydrogen bubbles develop at the counter electrode; these bubbles often migrate towards the anode and cause a considerable disturbance in the meniscus area. A suggested solution to this problem is to shield the cathode from the anode, either by placing the counter electrode in a separate beaker connected through a bridge [20, 23], or by surrounding it with a glass tube [15]. One also has to watch for dirt particles from the surrounding air that will undoubtedly deposit at the surface of the electrolyte; these particles follow the liquid flow and start spinning around the etching neck. If they get too close to the wire, they can also destroy the meniscus.

Another factor to take into account is the concentration of the electrolyte. The dilemma is the following: a low concentration will imply a long etching time, which increases the chance of having dirt particles and hydrogen bubbles disturbing the meniscus, whereas a high concentration will yield an etching reaction that is faster but so violent that the quick change in cross-sectional area of the wire will often be sufficient to cause the meniscus to drop. A compromise has to be made and a trial and error approach will help in determining the appropriate concentration. For our particular setup and etching conditions, we developed a quick rule of thumb: if the starting etching current was above 9 A, the reaction would most certainly be too violent; we would turn off the applied voltage right away and dilute the solution.

The Applied Voltage

Some thought should be given about the choice of the applied voltage when electrochemically etching tungsten tips, since it appears to have an influence on their overall shape.

The most striking effect associated with the use of an AC voltage is the abundant formation of gas bubbles around the specimen surface [15, 24, 29, 30]. As as result, the formation of the protective layer around the lower part of the wire (figure 2.3) is disturbed, yielding a delocalized electrolytic attack [15], and the bubbles also cause the etching to extend above the air/electrolyte interface. Consequently, tips with a long taper length, which are not ideal for STM use, will be produced. However, it

has been demonstrated [29, 30] that one can take advantage of this bubble stream if the tip is oriented upwards in the solution; in this reverse electrochemical etching configuration, the directional bubble flow affects the local etching rate in a way that enhances tip sharpening.

A low DC voltage tends to generate a strong necking effect, thus encouraging a very localized electrolytic action. Sharp tips with a pronounced concave shape are produced, making them perfectly suitable for an STM experiment. With a high DC voltage however, the drop-off is quite improbable since the high reaction rate will quickly etch the lower part of the wire before a significant neck can be created [15]. Moreover, a voltage above 4 V could apparently lead to the growth of a notably thick oxide layer on the tip [19]. From these claims, we expect that our low DC voltage of 3 V should be close to optimal.

The Length of the Wire Immersed in Solution

The length of the immersed part of the wire is another determining parameter in the final tip shape. It is quite intuitive to understand that too small a dipping length will not yield a necking phenomenon [21]. However, contradiction exists among authors as to whether or not the quality of the tip increases with the dipping length. It was reported [19] that the longer the submerged wire, the larger the radius of curvature of the tip. The explanation is that as the length increases, the weight of the part hanging below the neck increases as well; this can cause a premature drop-off and thus possibly produce blunt tips. On the other hand, it was also claimed [16] that a longer immersed wire yields a sharper tip. We found that a dipping length of 0.5 mm generally gave good results, but this is a clear example that there are still open questions in the field and that more systematic experimental studies should be pursued.

2.1.4 A Comparison: Electrochemical Etching of Iridium Tips

Although tungsten is probably the most widely used material to prepare tips for STM applications in UHV, other metals could offer certain advantages. Iridium is

an interesting candidate since it is a very stiff material that is much more inert to oxidation than tungsten. On the other hand, its lower chemical reactivity makes it harder to etch and often requires the use of dangerous chemicals [3, 13, 14]. A method using relatively benign electrolytes has nonetheless been suggested [31] and, out of curiosity, we applied it to a 0.25 mm diameter polycrystalline iridium wire.

The technique advises the use of a $CaCl_2$ solution of 30% to 50% saturated concentration, an AC voltage between 20 and 30 V, a graphite counter electrode and a dipping length of 3 mm. Since the drop-off phenomenon does not occur in this reaction, the voltage has to be turned off manually when the electrochemical activity stops. The parameters that gave us the best results were a 40% saturated concentration and an AC voltage of 20 V. In contrast to the etching of tungsten tips, the starting current is very low – in our case, it was around 0.4 A – and the time elapsed until there is no more noticeable activity in the solution is very long – up to 45 minutes. A typical iridium tip made using this procedure is shown in figure 2.6. An

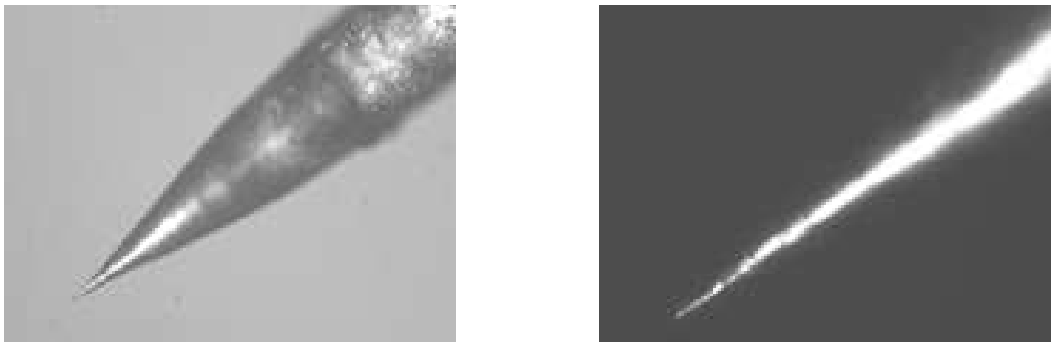

Figure 2.6: Freshly electrochemically etched iridium tip observed under an optical microscope with a 10X magnification on the left and a 50X magnification on the right.

interesting feature is the overall shape of iridium tips. The absence of a pronounced curvature along the tip shank is quite common from AC etching and the lack of a strong necking effect. This is made obvious in figure 2.7, where SEM images show the differences in shape between a tungsten tip (left) and an iridium tip (right). One can notice how much more concave the shape is in the case of tungsten.

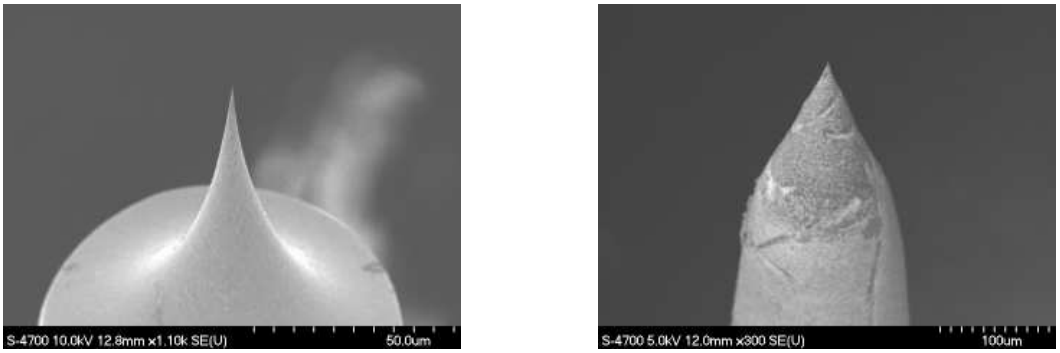

Figure 2.7: SEM images comparing the overall shape of two electrochemically etched tips. The left image shows a tungsten tip and the right image, an iridium tip. (Please note the difference in magnification and scale between theses two images.)

As pointed out in section 2.1.3, the use of AC voltages involves gas bubbles formation; this turned out to be a major problem in the preparation of iridium tips. The bubbles would sometimes climb up high enough on the wire to actually touch the tip holder; this would generate important current fluctuations and disturb the etching process. The froth of bubbles would also interfere with the monitoring of the reaction through an optical microscope. A solution to this problem is to use the same electrolyte, but in an acetone saturated solution. The addition of acetone has been reported to control bubble formation [32] and we did see a major improvement upon resorting to this modification.

Since we decided to concentrate on tungsten as the tip material, we did not push further our experiments on iridium wire. From our various optical microscope and SEM observations, we suspect that the procedure suggested above does not yield sharp tips. Information is available in the literature about further etching or polishing steps that can be done to achieve an apex radius of a few nanometers on platinum or platinum/iridium tips [15, 32, 33]. These techniques would probably also work on iridium tips since etching recipes for iridium and platinum are similar [3, 13, 31].

2.1.5 Other Ways of Making Sharp Tips

"Possibly there are as many tip-preparation procedures as there are people making tips. [20]" This statement reflects the amazing variety of existing approaches to produce sharp tips and makes it clear that an exhaustive review of these techniques would be a rather tedious task. Researchers continue to innovate by creating their own procedures or by trying new combinations of known techniques. Useful descriptions of the most popular methods are available in references [15, 29, 34, 35]; only a quick overview of these techniques will be provided in this section.

As a general rule, tip-forming techniques tend to fall within one of the two following categories: mechanical procedures and physicochemical procedures. Mechanical procedures were popular in the early age of STM [29, 36] due to their simplicity and their ability to yield atomically resolved images. This category includes techniques such as cutting a metal wire at an angle with a wire cutter, a scissor or a razor blade [35, 37, 38], fragmenting bulk pieces of material into small pointy pieces [39], or grinding a metal rod in order to get a sharp tip shape [40]. Mechanical procedures usually leave a ragged surface at the end of the tip and the numerous tiny asperities protruding from the apex almost always guarantee atomic resolution on flat surfaces. Even a broken pencil lead managed to successfully image the structure of highly ordered pyrolytic graphite [41]! However, mechanically prepared tips display an irregular shape and a large macroscopic radius of curvature [34]. During STM imaging, they perform quite irreproducibly and often show poor stability particularly on rough surfaces; the presence of several minitips at their apex can also lead to multiple image signals and other artifacts [34, 35].

Physicochemical procedures can yield extremely sharp and symmetric tips in a more reproducible fashion than mechanical procedures and seem to be the methods of choice nowadays [15]. Electrochemical etching, either as described in this chapter or along with additional refinements [15, 18, 30], is probably the most popular tip preparation method. It is sometimes performed as a two-step procedure, where the second step consists in "zone electropolishing" the tip to further sharpen it in a

very controlled manner. During zone electropolishing, the tip is moved by a micromanipulator through a thin film of electrolyte contained in a loop of metal – which acts as the counter electrode – so that very small amounts of material can be removed locally [15, 35]. Note that this extra step was not required in our case, since very sharp tungsten tips could be obtained from our etching procedure. Various other physicochemical procedures exist; for example, sharp tips can be made by chemical vapor deposition [42] or electron beam deposition [43] onto pre-existing tips, as well as by ion milling [44]. Ultimate control on the tip apex shape can be achieved with field ion microscopy techniques, where consecutive field evaporation of single atoms can yield a particular atomic configuration of the apex. The specifics of this process will be addressed in chapter 4.

2.2 Annealing the Tungsten Tip in UHV

2.2.1 Why do Tungsten Tips Need Further Cleaning?

Tungsten tips resulting from a successful electrochemical etching process are quickly transferred to the preparation chamber of our UHV system for a further cleaning step, as their surface is inevitably covered with contaminants which cannot be removed by mere rinsing in water, acetone and ethanol.

It is well known that an oxide layer (mainly WO_3, which is also referred to as tungsten trioxide) develops on the tip shank during electrochemical etching [45, 46], but it is not quite understood how the growth of this amorphous layer relates to the tip etching parameters [20, 44]. As was briefly mentioned before, it has been suggested that a higher DC etching voltage could yield a particularly thick oxide layer [19], but authors who actually looked at this layer with a transmission electron microscope (TEM) agree to say that it is usually a few nanometers thick [20, 21, 44, 45, 47], regardless of the etching conditions. Using either TEM, Auger microscopy or energy dispersive x-ray analysis, the distribution of this oxide layer has been studied and there exists a great disparity between the various claims. Some authors noticed a more significant contamination around the tip apex [21, 38], while others observed a

higher degree of oxidation at the tip base (close to the unetched part of the wire) [46]; a uniform oxygen contamination along the tip has been reported as well [16]. Auger microscopy and energy dispersive x-ray analysis have also revealed the presence of other surface contaminants such as carbon, nitrogen, alkali metal hydroxides (e.g. KOH) and microcrystals (e.g. WO_3K), which are left on the tip from the electrochemical bath and exposure to the atmosphere [16, 17, 20, 38].

Although a firm understanding of the chemical changes happening on the tip surface during and after etching is still lacking, it is a well-grounded belief that freshly etched tungsten tips are not readily suitable for STM imaging or spectroscopy. The various contaminants listed above will undoubtedly cause instabilities in the tunnel junction, thus affecting the image quality and increasing the noise level [20, 22, 38, 48]. The presence of an insulating oxide layer can even lead to a tip crash, since the resistance of this layer is most likely greater than the tunnel gap resistance corresponding to the set current; this implies that the tip will touch the sample's surface before the desired current can be reached [16, 34, 44]. Sometimes a controlled tip crash may allow a more stable tunnel junction to be recovered, either by breaking the oxide layer covering the tip or by transferring some atoms from the sample to the tip [41, 45, 48]. However, since our experiments require a sharp atomically defined tip (see chapter 1), intentional crashing is not an option! There exist more appropriate, controllable and reproducible ways to remove the contaminants, in particular the undesired oxide layer. Some of these methods will be outlined in section 2.2.4, whereas sections 2.2.2 and 2.2.3 will focus on the annealing process, which is the method we chose to further clean our tungsten tips.

2.2.2 Experimental Details of the Annealing Process

Heating the tip at high temperatures in UHV is a very efficient way to desorb the contamination layer. At temperatures above 1000 K, the following reaction takes place [36, 49]:

$$2WO_3 + W \rightarrow 3WO_2\uparrow \tag{2.4}$$

From equation 2.4, it can be seen that the tungsten trioxide (WO_3) covering the tip will react with tungsten to form tungsten dioxide (WO_2); the latter is volatile and sublimates around 1075 K [36, 50]. A clean metallic tungsten surface is therefore left behind [17, 20, 36]. Another advantage of this annealing process is that it heals the crystallographic defects generated by the electrochemical etching and the drop-off, and it smoothes out the tip surface [21, 51, 52].

In order to proceed with this annealing operation in our UHV preparation chamber, the tip is brought to a heating stage using transfer arms and manipulators. Feedthroughs allow this heating stage to be connected to a current generator outside the chamber. When the tip sits in place, each side of the tip holder is contacted by a metallic clip, thus permitting the passing of a current through the polycrystalline tungsten wire spot-welded onto the holder (see figure 2.1). The tip, being spot-welded on this conducting wire, will be resistively heated. In our setup, there is no precise way to monitor the temperature reached by the tip; we use the color of the heated tip, from blackbody radiation, as a rough indication of its temperature. When performing the annealing, it is important to turn off all the external lights, switch off the ion pressure gauge and cover the unused window ports of the preparation chamber since it is easier to get a better feel for the glowing color in a dark environment.

Finding the optimal annealing parameters is quite a tricky task. It has been suggested that since the sublimation of WO_2 starts around 1075 K and that pure tungsten melts at the much higher temperature of 3683 K, there is no risk of blunting the tip when the WO_2 sublimes [20]. However, this statement is somewhat misleading, as the surface diffusion of tungsten atoms might start blunting the tip at much lower temperatures than the tungsten melting point. This particular issue will be addressed in greater detail in section 2.2.3. After trying various annealing temperatures and times, we found that the method yielding the best results was to first flash anneal the tip for 2 seconds at a bright orange glow, which would usually correspond to a current between 3.0 and 4.5 A, and then to lower the current to about 2.0 A for at least 5 minutes. Note that by "best results", we mean tips that would reproducibly

be clean but still sharp; a quick and convenient test for sharpness can be done right after annealing and will be explained in chapter 3. The goal of the first annealing step – what we called flash annealing – is to go to a high enough temperature to remove the oxide layer, but not too high nor for too long to induce substantial blunting of the tip. It has been reported that around 900 K, the tip just starts to glow [53] and thus exhibits a dark red color; between 1175 K and 1300 K, the tip has an orange glow [1, 21] and around 1375 K, the tip has a yellow glow [1]. Perception of colors is a very subjective matter and varies between individuals, but from the previous claims, we can deduce that our bright orange glow probably corresponds to a temperature close to 1300 K. The second annealing step, which consists in heating the tip at a much lower temperature for a longer time, is intended to allow other remaining impurities to desorb and also to degas the tip holder.

2.2.3 Consequences of the Annealing Process on the Tip Shape

Tip Blunting

While being quite successful at removing the contamination layer from the electrochemically etched tungsten tips [38, 53], the annealing process has been reported to routinely lead to the blunting of these heated tips [51–56]. In our quest for the sharpest tips, this effect is far from desirable and thus deserves some attention in order to be better understood and prevented.

The tip shape evolution during annealing in UHV is determined by the action of two mechanisms: surface diffusion and evaporation of tungsten atoms [52, 55, 56]. Surface diffusion is due to capillary forces and causes atoms to migrate from the tip apex to the tip shank, thus increasing the radius of curvature of the apex. Conversely, evaporation leads to an overall sharpening of the tip apex by removing material from the tip. Intuitively, the rate of change of the apex radius R during annealing should then correspond to the superposition of the blunting rate due to surface diffusion and the sharpening rate due to evaporation [56]:

$$(dR/dt)_{total} = (dR/dt)_{diffusion} - (dR/dt)_{evaporation} \tag{2.5}$$

However, evaporation is significant only at high temperatures; in the case of metal tips, a minimum temperature of about $0.7 \cdot T_m$ is required, where T_m is the melting temperature of the particular metal [56]. Therefore, for $T_{annealing} > 0.7 \cdot T_m$, the tip shape results from the competitive actions of both surface diffusion and evaporation as predicted by equation 2.5, whereas for $T_{annealing} < 0.7 \cdot T_m$, only surface diffusion plays a role in establishing the final tip shape and the term $(dR/dt)_{evaporation}$ can be ignored in equation 2.5 [55, 56].

At first sight, the case $T_{annealing} > 0.7 \cdot T_m$ looks appealing since it introduces the possibility of a decrease in tip radius. However, tip sharpening from such thermal treatment will happen only under very specific conditions. A closer look at equation 2.5 should help to clarify this point. Equation 2.5 suggests the existence of a limiting radius which is reached when $(dR/dt)_{total} = 0$ or, in other words, when there is an equilibrium between the surface diffusion rate and the evaporation rate. Only tips with a starting radius *above* this limiting radius value will get sharpened during a high temperature annealing process, but their final reduced radius will not reach values *below* this limiting radius value. Conversely, tips with a starting radius smaller than the limiting radius value will get dulled by such annealing process, but their final radius will not exceed this limiting value [52]. Experimental studies have demonstrated that this limiting radius exists and that its exact value depends on the tip material, the annealing temperature and the tip cone angle, but not on the tip radius [52, 55, 56]. For tungsten, the limiting radius is of the order of a tenth of a micron [55, 56]. Our electrochemically etched tungsten tips are usually much sharper than that and thus high temperature annealing would yield blunting of these tips. On the other hand, even if our tips had a starting radius greater than the limiting radius and got sharpened during the annealing, this sharpest achievable radius of a tenth of a micron is still way too large for our purposes (see chapter 1). From these arguments, we can reason that $T_{annealing} > 0.7 \cdot T_m$ is not an appropriate annealing condition for our tips.

Quantitative studies [54, 55] of the tip shape evolution due to surface diffusion alone (i.e. $T_{annealing} < 0.7 \cdot T_m$) revealed that the radius of curvature of the tip apex (R) increases with the duration of the thermal treatment (t) following the scaling law

$$R \sim t^{\frac{1}{4}} \tag{2.6}$$

It has also been reported that the blunting rate increases with the annealing temperature [52], and that the self-diffusion flux of atoms is proportional to the chemical potential gradient, which in turn is proportional to the surface curvature gradient [54, 55]. The latter observations and equation 2.6 make it quite clear that a short annealing time at a a reasonably low temperature will limit tip blunting. This is especially important when a really sharp tip is annealed, since the high surface curvature gradient of a sharp apex favors a particularly quick migration of atoms towards the shank. Our flash annealing procedure described in section 2.2.2 meets these requirements: the annealing time is short (2 seconds), and the claimed temperature of 1300 K, while high enough to sublimate the oxide layer, is still well below $0.7 \cdot T_m$ (note that $0.7 \cdot T_m \simeq 2580$ K for tungsten.) One might argue though that a short annealing time will not be efficient enough to remove all of the oxide layer present on the tip shank. This is a definitive possibility, but one should keep in mind that the last traces of contamination can be easily removed by field evaporation during the FIM process (see chapter 4). We find it better to use a short annealing time and to perfect the tip cleaning with FIM, rather than to take the risk of dulling our tips by annealing them for too long.

As a closure to this section, figure 2.8 illustrates how annealing can occasion tip blunting. Figure 2.8a) shows an SEM image of an annealed polycrystalline tip used for FIM. This tip displays a 40 nm diameter protuberance lying on top of a 170 nm diameter spherical feature; a small neck is also visible under this sphere. Figure 2.8b) presents the same tip after two further annealing treatments. One can notice that the sharp protuberance and the neck have disappeared, and that the tip apex now has a 250 nm diameter (note the different magnification on this image). To verify these observations, the tip has then been rotated by 90^o in the SEM chamber and is shown

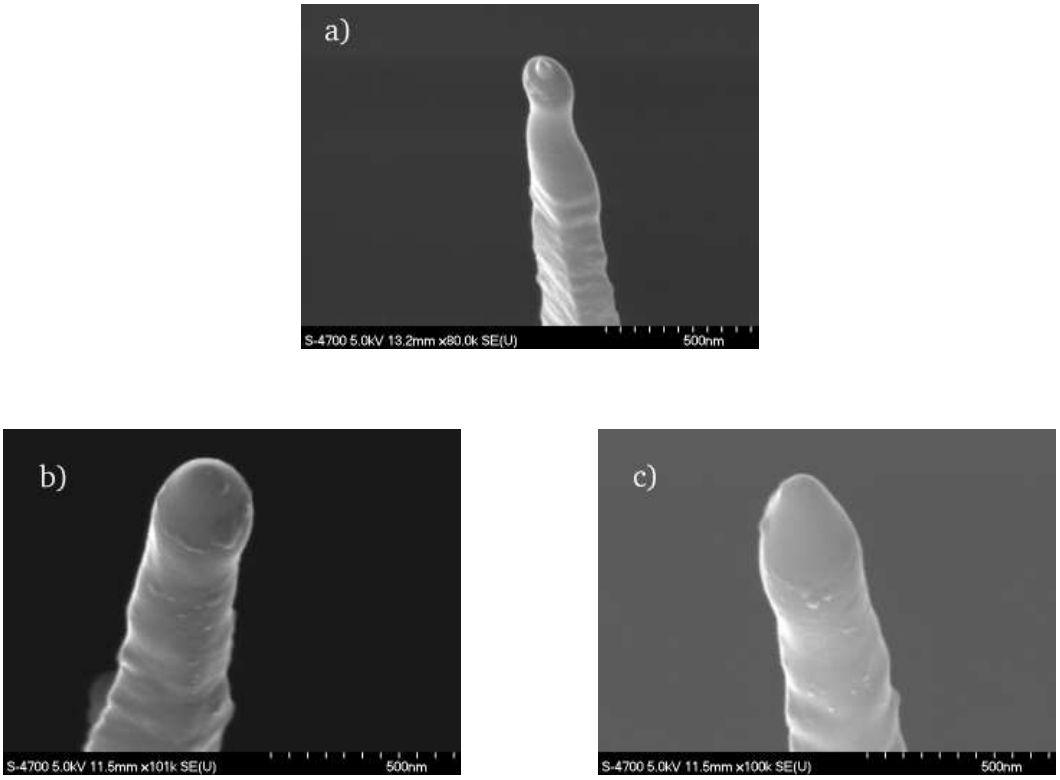

Figure 2.8: Illustration of tip blunting by surface diffusion of tungsten atoms from the apex to the shank during annealing. a) Tip before the additional heating treatments. b) Tip after the additional heating treatments, displaying an overall blunting of the apex. c) 90^o rotation of the blunted tip.

in figure 2.8c); the characteristics displayed in figure 2.8b) apply here as well. This is an example demonstrating that the heat induced self-diffusion of atoms from the apex to the shank lead to an overall blunting of the tip. Note that the tip shown in figure 2.8a) was annealed following our optimal procedure described in section 2.2.2 and exhibited a sharp enough apex to be a suitable specimen for field ion microscopy studies. It is the undergoing of two further similar annealing steps that caused the significant dulling of this tip.

Unexpected Tip Shapes

Occasionally, tips submitted to the annealing treatment described previously would reveal unexpected profiles when imaged under the SEM. One of the "irregularities"

observed is shown in figure 2.9 and consists on a little ball sitting at the tip apex. The left image displays a (111) oriented tungsten tip and the right image presents a polycrystalline tungsten tip; both tips exhibits a similar apex shape. We can offer two hypotheses to explain how such a ball-like structure could potentially be generated.

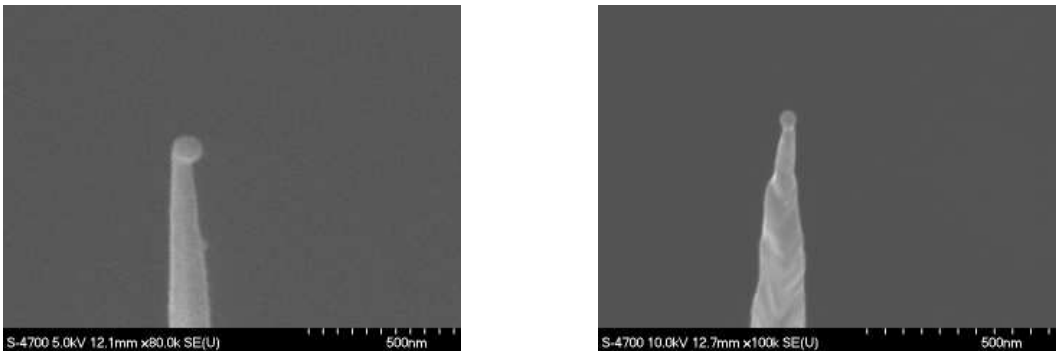

Figure 2.9: SEM images of a single crystal (111) oriented tungsten tip (left) and a polycrystalline tungsten tip (right) displaying a little ball at their apices after an annealing treatment.

Our first hypothesis is that this shape is defined as the tip is annealed. As was pointed out earlier, the atomic surface diffusion flux induced on the tip during annealing is proportional to the surface curvature gradient. Since the surface curvature at the tip apex is far more pronounced than the surface curvature along the shank, the flux of atoms leaving the apex will be greater than the flux of atoms diffusing along the shank. Computer simulations of tip profile variations have demonstrated that this diffusion flux dynamics causes the creation of a bulbous apex region and the possible formation of a neck under the apex [55]. A similar effect has been observed experimentally by other authors [20] who annealed their tips for 30 seconds by electron bombardment. They claim that "local heating" is responsible for the formation of a neck under the apex and that the ball-like structure is simply a molten apex; however, they do not clarify the causes and mechanisms of this local heating, nor do they mention their annealing temperature. While their experimental findings coincide with ours, we believe the surface diffusion flux dynamics explanation to be a more plausible and satisfying way to interpret the tip shape displayed in figure 2.9.

Our second hypothesis is that the ball-like structure is a result of the electrochemical etching process. Several authors [13, 15, 19, 22, 24] have reported the presence of severe deformations such as balls, bent points or dislocations at the apex of tips that were electrochemically etched but not annealed. This phenomenon has been observed to become more significant as the length of the wire immersed in the electrolyte solution increases, which suggests the following explanation. Remember that as the etching progresses, a neck is formed and the drop-off occurs when the weight of the lower part of the wire exceeds the tensile strength of the neck (section 2.1.2). When the lower part of the wire falls, the downward force that was acting on the neck during the etching is suddenly removed and the mechanical energy stored in the neck is released; this energy is thought to be sufficient to cause a slight recoil of the tip or a local melting of the apex [19, 24], thus justifying the presence of a little ball at the very end of the tip. As the length of the immersed wire increases, the weight of the stub hanging below the neck increases as well; under these conditions, many dislocations can result in the tip structure from the larger stress applied by the hanging piece of wire and the deformations induced by the drop-off are expected to be more important, which corresponds to the findings of the authors cited above.

In our case, it is hard to tell with certainty which hypothesis could best explain the tip shape shown in figure 2.9 since these SEM pictures were taken after the annealing of the tips; there is thus no way to know how these tips looked like right after the electrochemical etching. Other tips have been imaged under the SEM after being electrochemically etched, but no ball-like structure has been observed. However, this does not yet rule out the possibility of the drop-off causing this apex shape. Indeed, this shape has been observed only twice during the scope of our studies, which indicates that whether it is due to the annealing or the etching, it is not a very common phenomenon. We think that by using a short annealing time, we limit the effects of the surface diffusion, and by dipping a short length of wire in the electrolyte, we minimize the amount of energy released at the break off; in both cases, the likelihood of obtaining a ball-like structure at the apex is kept rather small.

Further studies in which the annealing time and the dipping length would be varied in a systematic fashion could help us gain some insight on the true causes of this "unusual" tip shape.

Another unexpected tip shape is presented in figure 2.10. These SEM images show two different views of the same polycrystalline tungsten tip which was electrochemically etched and annealed following our usual procedure. As can be seen on

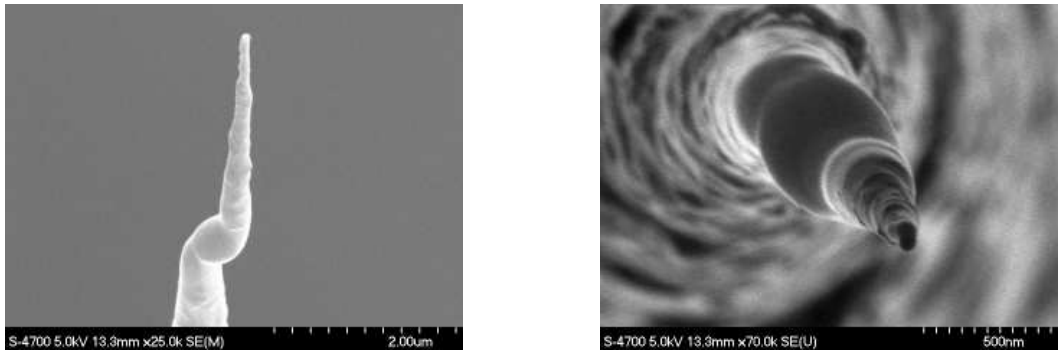

Figure 2.10: Two different views of a polycrystalline tungsten tip showing severe deformations along with a variation in the surface texture.

the left image, the tip displays two obvious bent points located a couple of microns under its apex, and the right image shows how smooth the surface is nearby these bent points in comparison with the rest of the tip. A rugged surface is typical for an electrochemically etched polycrystalline tungsten tip because it is composed of variously oriented crystallites, so this unusually smooth area suggests that some rearrangement of atoms happened. Again, this rearrangement is most likely an effect of the annealing process, during which atomic surface diffusion was enhanced around the bent points due to their high surface curvature gradient. We can only speculate as to why these two bent points appeared in the first place. A possible explanation is that the polycrystalline wire used to etch this tip had some pre-existing defects or weaknesses at these particular sites; these weak points were then more susceptible to suffer from plastic deformations when the drop-off occurred.

From the two examples presented in this section, one can learn that a routine electrochemical etching and UHV annealing with no observed irregularities can, from time to time, yield unintended tip features. The deformations can be due to either the etching or the annealing process, but they can also result from a combination of these two operations, since the heat induced surface diffusion of atoms will be directed according to the particular tip shape left by the etching. As a last comment on this topic, it is worth mentioning that tip deformations can occur under other circumstances than the ones mentioned above. Figure 2.11 illustrates this point; it shows a severely bent polycrystalline tungsten tip, but the deformation is not due to the electrochemical etching nor to the annealing since this tip was successfully used for FIM studies. Only very sharp tips can be imaged by FIM, so such a deformed

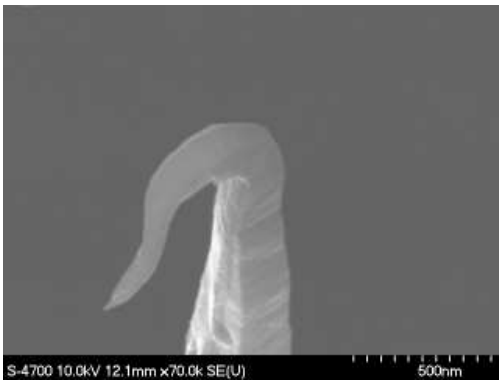

Figure 2.11: Severely bent polycrystalline tungsten tip. The deformation is most likely due to a tip crash during an STM spectroscopy experiment.

tip would not have been a suitable FIM candidate. The bending observed on this tip most likely happened later on, while performing an STM spectroscopy experiment on a gold substrate. The tip shape displayed in figure 2.11 is a typical indication of a tip crash [20, 22, 45], although the exact mechanism by which the crash causes the tip to curl while leaving the apex intact is not fully understood.

2.2.4 Other Tip Cleaning Methods

Although the annealing of freshly electrochemically etched tungsten tips is among the most widely used techniques to remove surface contaminants, other popular methods exist and will be shortly summarized in this section.

HF Chemical Cleaning

The idea behind this technique [48] is to dip the tip in hydrofluoric (HF) acid right after completion of the electrochemical etching to solubilize the tungsten oxides. Tungsten itself does not react with HF, but all of its oxides are soluble in a concentrated HF solution, so a clean tungsten tip should result from this treatment. The suggested dipping time is between 10 and 30 seconds, and the recommended concentration is 51% HF in water. The author has shown the efficiency of this technique by comparing the performance of treated and untreated tips in STM imaging and spectroscopy; treated tips turned out to have highly superior imaging capabilities and displayed a truly metallic behaviour in spectroscopy. Auger microscopy studies have also confirmed the ability of HF attack to remove oxides from the tip [46]. However, it has been reported that a similar HF chemical cleaning treatment, with a slightly lower solution concentration, gave quite irreproducible and unpredictable results [20]. It was also observed that HF cleaning leads to a significant blunting of the tip [17].

Ion Milling

Ion milling consists in directing argon ions to the tip surface in order to remove the contamination layer by sputtering. In a usual setup, the tip is either rotated in a flux of argon ions with the ion beam at a certain incident angle, or placed right under the ion beam so that its axis coincides with the beam. The bombardment time and flux energy vary with the particular geometry of the setup, but exposures of tens of minutes at a few keV are often encountered in literature [17, 22, 44]. Ion milling is an effective way to clean the tips and it has the advantage of further decreasing the radius of the tip apex since sputtering also removes tungsten atoms [22, 34, 44]. However, a short annealing step is usually necessary afterwards to heal the damage

caused by ion sputtering [51, 53]. It has been reported that multiple tips might result from the ion milling process on polycrystalline tips, due to the lamellar texture of polycrystalline tungsten wire [22, 44]. The formation of a neck just below the tip apex has also been observed and attributed to the trajectory of the ions and the local roughness of the tip surface [20].

Self-Sputtering

Cleaning the tip by self-sputtering has effects very similar to ion milling. Self-sputtering occurs when the UHV chamber is filled with neon at a pressure around 10^{-4} mbar, and a high negative voltage is applied to the tip. Under these conditions, the electric field at the tip apex will ionize the noble gas atoms and cause these positive ions to be accelerated back towards the tip, thus inducing sputtering. As with ion milling, self-sputtering leads to the removal of contaminants and to further sharpening of the tip. The difference is that this process can be conveniently monitored through the field emission current generated by the tip apex [20, 57]. One can then follow the evolution of the tip apex shape, as a higher field emission current corresponds to a sharper tip. Field emission will be discussed in detail in chapter 3.

Additional Annealing Techniques

Because of the potential tip blunting associated with the annealing process described before (sections 2.2.2 and 2.2.3), some refinements to this technique have been proposed. Annealing the tip in presence of an electric field with a high gradient or annealing the tip in an oxygen atmosphere are examples of methods which efficiently clean the tip while lowering the overall blunting rate. If properly mastered, they also allow the resharpening of a blunt tip inside the UHV preparation chamber. The prospect of recycling "bad tips" is quite appealing; more attention will therefore be given to these techniques in section 3.3.

2.3 Summing Up our Optimal Tip Preparation Technique

This section is intended as a convenient reference regrouping the various etching and annealing parameters which reproducibly yielded good tungsten tips using our particular setup. This tip preparation information is summarized in tables 2.1 and 2.2.

Etching Parameter	**Optimal Value or Procedure**
Tip wire diameter	0.1 mm polycrystalline wire, or 0.13 mm (111) oriented wire.
Electrolyte concentration	7.5 mol/L KOH (11 KOH pellets in 2.8 mL of water)
Applied voltage	3 V_{DC} (tip on positive bias)
Counter electrode	Steel loop
Pre-etching tip immersion length	1 mm
Pre-etching time	5 seconds
Etching tip immersion length	0.5 mm
Starting etch current	Between 4 and 9 A (Above 9 A, the etching is too violent and the meniscus is destroyed.)
Etching time	The etching is stopped automatically when the drop-off occurs. It usually takes a couple of minutes.
Monitoring of the reaction	Through an optical microscope
Cleaning procedure (after the pre-etching and for the final tip)	1) Dip in distilled water 2) Rinse with acetone and ethanol 3) Dry with compressed N_2 gas

Table 2.1: Summary of the parameters yielding the optimal electrochemical etching procedure for our tungsten tips.

Annealing Step	**Tip Color**	**Applied Current**	**Time**
1) Flash annealing	Bright orange	Between 3.0 and 4.5 A	2 seconds
2) Low current annealing	Not glowing	2.0 A	5 minutes

Table 2.2: Summary of the optimal UHV annealing two-step procedure for our tungsten tips.

Note that the tips produced by successfully following this procedure need to undergo further tests and treatments in the UHV system; they have to be checked for sharpness (chapter 3) and get their apex atomically engineered into a stable configuration (chapter 4) before being considered suitable for molecular electronics studies.

3

Field Emission: a Useful Tip Characterization Tool

Most of the tungsten tips prepared according to the etching and annealing techniques described in the previous chapter display a sharp enough apex to be suitable candidates for field ion microscopy studies (see chapter 4). However, about 25% of our tips do not meet the sharpness requirement imposed by our FIM setup; the resulting impossibility to atomically characterize their apex thus prevents us from taking a crucial step towards a meaningful single molecule conductivity measurement. The most probable explanations for these occasional encounters with tip radii larger than a few nanometers are a premature drop-off at the end of the etching process or a significant amount of surface diffusion of tip atoms induced by the annealing procedure.

The field ion microscope, although very elegant in the simplicity of its working principle, is labour intensive in practice; a lot of time and resources can be saved if FIM experiments are done only on tips that will *assuredly* yield useful FIM images. This most definitively suggests the need for the tips to undergo a "sharpness test" *before* being used for FIM studies. Fortunately, such a test exists; it relies on the physical phenomenon called field emission, which will be explained in section 3.1. Monitoring the field emission characteristics of the tip is a quick way to verify its sharpness and a more involved examination of the field emission data can even lead to the extraction of a tip radius value; this will be covered in section 3.2. Finally, some interesting techniques allowing a possible *in situ* resharpening of the tips that failed the sharpness test will be presented in section 3.3.

3.1 Field Emission Theory

Under the influence of a high electrostatic field, electrons can be emitted from a metallic surface into vacuum; this purely quantum mechanical phenomenon is called field emission.

3.1.1 Removing an Electron from a Metal Surface

To understand field emission, it is important to recall that the electrons in a metal reside in a potential well, mainly because of their attraction to the positive ions [58]. In an electrically neutral metal, this barrier can be crudely represented by an abrupt potential step that electrons cannot surmount, as illustrated in figure 3.1. The step height, as measured from the metal's Fermi level μ, is equal to the work function ϕ ; the latter is then defined as the minimum energy that an electron at the Fermi level must possess in order to escape into free space [2, 34].

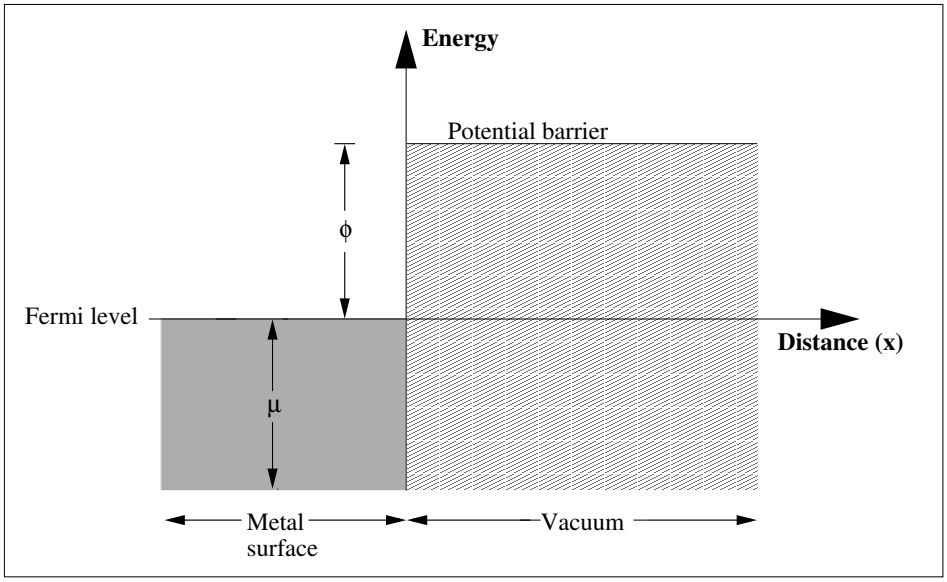

Figure 3.1: Potential energy diagram for electrons in a metal. The step height, calculated from the Fermi level μ, is equal to the metal's work function ϕ.

Two main effects contribute to the magnitude of the work function. The first contribution is called inner potential and is basically equal to the difference between

the chemical potential of the electron in the metal and its chemical potential in a far away, field-free vacuum [2]. The inner potential is a property of the metal and is path independent, which means that it does not display crystallographic anisotropy [59]. The second effect is the result of the electrostatic potentials present at the metal surface. When an electron passes through the metal surface, it has to travel in a quite inhomogeneous environment; even if the surface is practically electrically neutral, there is always a strong dipole layer where the crystal "terminates" [59]. In fact, one can easily imagine that since the atoms at the surface of the metal do not have as many nearest neighbours as the atoms in the bulk, the charge distribution at the surface must be quite different than in the bulk. Moreover, once the electron has exited the metal, it will experience an interaction with its image charge on the surface; note that this interaction is coulombic in nature, except when the electron is very close to the surface and exchange and correlation energies should be considered instead [2]. The strength of these surface electrostatic potentials varies with the surface structure, which explains why the work function for a particular metal differs from one crystallographic plane to another [2, 59]. Typical values of ϕ for metals are around 4 to 5 eV, and vary between planes by $\sim \pm 10$ % [59].

Two well known techniques, thermionic emission and photoemission, allow the emission of electrons from a metal into free space by providing them with enough energy to overcome the potential barrier at the metal surface. In thermionic emission, the metal is heated so that a significant amount of electrons acquire a high enough kinetic energy to escape the metal [58]. In photoemission, the metal is irradiated with photons of energy greater or equal to the work function, thus enabling electrons to freely flow out of the metal in proportion to the incoming photon density [59]. However, these two phenomena are fundamentally different from field emission. Field emission does not require the electrons to gain energy and hop over the potential barrier in order to be emitted in vacuum. *Field emission occurs when the applied external electrostatic field induces such a strong deformation in the potential barrier that unexcited electrons can tunnel through it* [2].

3.1.2 Towards the Fowler-Nordheim Equation

The effect of an applied electrostatic field on the shape of the potential barrier can be better understood from figure 3.2, which represents the potential energy diagram for electrons at a metal surface in the presence of an applied electrostatic field [2, 60].

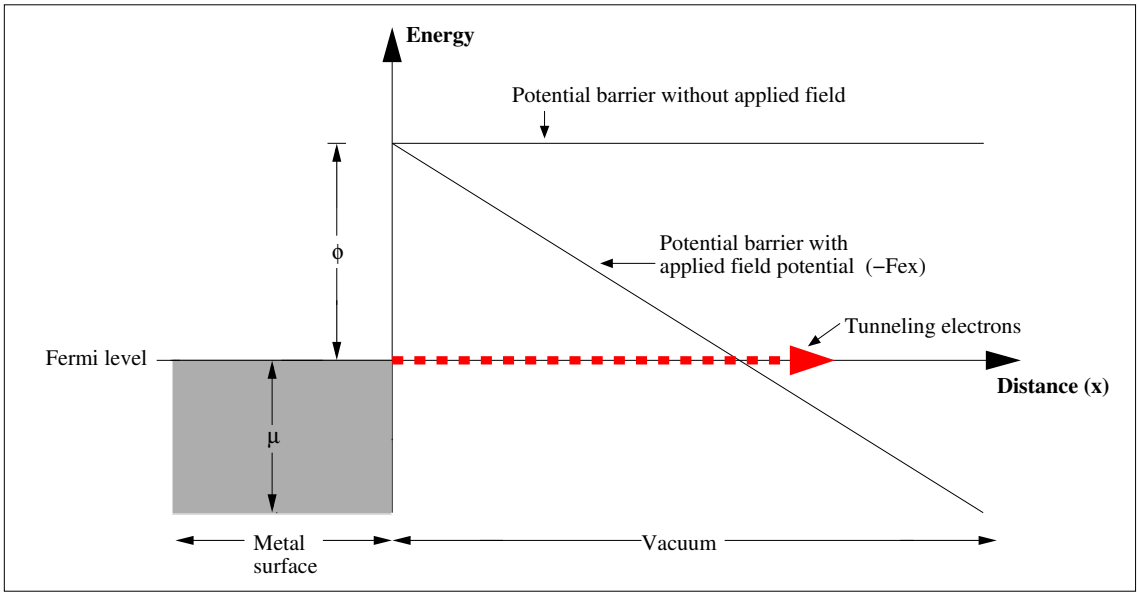

Figure 3.2: Potential energy diagram for electrons at a metal surface in the presence of an applied electrostatic field F.

The applied field potential has the form

$$U_{field}(x) = -Fex \tag{3.1}$$

where F is the applied field strength and e is the electronic charge. Taking the Fermi level μ to be the zero point of the energy axis, as is done in figure 3.2, the effective potential seen by the electrons is now

$$U_{effective}(x) = \phi - Fex \tag{3.2}$$

as opposed to the barrier potential seen when no field is applied, which is simply given by

$$U_{well}(x) = \phi \tag{3.3}$$

and represents the potential well depicted in figure 3.1. One can see right away that the external field considerably lowers the potential barrier; it now displays a triangular shape instead of a step-like shape. In order to escape from the metal, the electrons at the Fermi level have to tunnel through a distance corresponding to the barrier width, which here is equal to

$$x_{barrier} = \frac{\phi}{Fe} \tag{3.4}$$

One can wonder why any tunneling should occur in the first place or, in other words, why unexcited electrons would just happen to "leak out" through this barrier. This is not an intuitive phenomenon and it can only be explained by quantum mechanical arguments. From the Heisenberg uncertainty principle, we know that the wave nature of the electron implies inherent uncertainties in its particle properties [58]. If the uncertainty in the electron's position is of the order of the potential barrier width, there is a finite probability of finding this electron on the other side of the barrier; in such a case, we say that the electron has tunneled through it [2, 34].

From equation 3.4, it can be seen that a higher applied field yields a thinner barrier width; the tunneling probability thus increases with the field strength, which causes a corresponding enhancement in the field emission of electrons. Pioneering work in the understanding of field emission was done by Fowler and Nordheim in 1928 [61]; they derived the field emission current density i as a function of the metal's work function ϕ and the applied electrostatic field F. The procedure they used consisted in computing the barrier penetration probability, multiplying it by the arrival rate of electrons at the barrier and integrating over all electron energies smaller or equal to the Fermi level μ. The result is contained in the so-called Fowler-Nordheim equation:

$$i = \frac{e^3}{2\pi h} \frac{(\mu/\phi)^{1/2}}{\mu + \phi} F^2 \exp\left[-\frac{4}{3} \frac{\pi\sqrt{8m}}{eh} \frac{\phi^{3/2}}{F}\right] \tag{3.5}$$

where e is the electronic charge, h is Planck's constant and m is the mass of the electron. Inserting numerical values for the constants, we can express the current

density in A/cm^2 as follows:

$$i = 6.2 \times 10^{-6} \; \frac{(\mu/\phi)^{1/2}}{\mu + \phi} \; F^2 \exp\left[-6.8 \times 10^7 \; \frac{\phi^{3/2}}{F}\right] \qquad (\mathrm{A/cm^2}) \qquad (3.6)$$

for μ and ϕ in eV and F in V/cm.

Equation 3.6 refers strictly to the zero temperature limit; however, field emission is virtually temperature independent and the error involved in using this equation at ordinary temperatures is negligible [2, 61]. Furthermore, Fowler and Nordheim's calculation is based on the assumption that the emitter is a one-dimensional smooth infinite plane with a uniform work function [60]. However, it will be shown in section 3.2 that, to a certain extent, their results can also be readily applied to the case of a tip-shaped emitter.

3.1.3 Improving the Fowler-Nordheim Equation

For a more accurate description of the field emission phenomenon, one should also include the contribution of the coulombic interaction between the electron and its induced image charge on the metal surface as it tunnels through it [2, 60]. Classical electrostatics tells us that the image potential has the form

$$U_{image}(x) = -\frac{e^2}{4x} \qquad (3.7)$$

Of course, equation 3.7 breaks down when an electron is too close to the metal surface since the potential energy U_{image} diverges for small values of x. Near the surface, the electronic surface states of the metal should be explicitly considered in order to get a realistic expression for the potential. However, it turns out that the classical image potential contained in equation 3.7 is a good enough approximation to estimate the effect of an externally applied electrostatic field on the potential barrier [59].

The field emission potential energy diagram including the image potential is presented in figure 3.3 [2, 60]. Taking into account the additional contribution of the image potential, the barrier seen by the electrons when no field is applied is now given by

$$U_{well}(x) = \phi - \frac{e^2}{4x} \qquad (3.8)$$

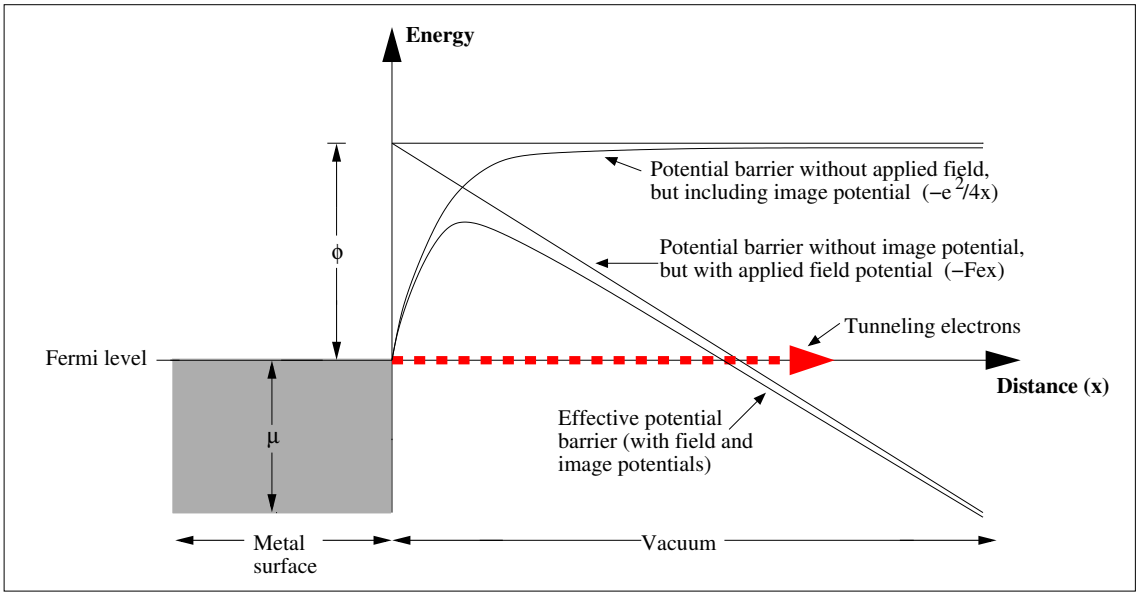

Figure 3.3: Potential energy diagram for electrons at a metal surface in the presence of an applied electrostatic field F, taking into account the image potential.

and figure 3.3 shows that this barrier has a softer shape than the step-like barrier illustrated in figure 3.1; the image potential somewhat rounds off the top corner of the barrier. Equation 3.8 thus replaces equation 3.3 and gives a more appropriate picture of the potential well in which the metal electrons are trapped. Equations 3.1 and 3.8 imply that the effective barrier seen by the electrons at a metal surface in the presence of an applied electric field when the image potential is considered becomes

$$U_{effective}(x) = \phi - \frac{e^2}{4x} - Fex \tag{3.9}$$

Figure 3.3 clearly indicates the effect of the image potential on the shape of the effective potential barrier. The effective potential barrier is lower and thinner than that obtained when neglecting image effects; note that the latter has been included in figure 3.3 for comparison purposes. From these observations, we conclude that since the tunneling probability is higher for a thinner barrier, the calculated current density emitted from the metal surface should be larger when the image potential is included.

Some corrections can be added to the Fowler-Nordheim equation (eq. 3.6) in order to account for the changes in field emission caused by this additional image potential. The derivation of the modified equation is the same as for equation 3.6, except that one has to consider a smaller potential barrier area when dealing with the computation of the barrier penetration probability [2]. The image correction factor has been calculated by Nordheim himself [61] and by other people as well [2]; whichever way the calculation was made, this factor, which depends on the applied field and on the work function of the surface, seemed to always take the form of a multiplicative correction α to the original Fowler-Nordheim exponent. α has been found to be a slowly varying function of the applied field F, which allows it to be treated as a constant in a standard application of the Folwer-Nordheim equation. Including a first order image correction, the equation governing field emission becomes [2]:

$$i = 6.2 \times 10^{-6} \; \frac{(\mu/\phi)^{1/2}}{\alpha^2(\mu+\phi)} \; F^2 \; \exp\left[-6.8 \times 10^7 \; \frac{\phi^{3/2}\alpha}{F}\right] \qquad (\mathrm{A/cm^2}) \qquad (3.10)$$

Knowing that α has a value comprised between 0 and 1, it can readily be seen that for a given field F, the current density i will be higher when calculated from equation 3.10 than when calculated from equation 3.6. In practice, the modified Fowler-Nordheim equation predicts that field emission will take place for values of the applied electrostatic field about 10 to 20 % lower than that required by the original Fowler-Nordheim equation [2].

Of course, further improvements can be made to the Fowler-Nordheim equation in order to better represent the effects of the various potentials present at a metal-vacuum interface; however, equation 3.10 offers a useful theoretical model for most field emission applications.

3.2 Field Emission as a Check for Tip Sharpness

The physical phenomenon of field emission described in section 3.1 proved to be an invaluable tool for the characterization of our tips, since it allowed us to gain some useful insight in the sharpness of our tungsten tips.

3.2.1 Relating Field Emission Data to Tip Sharpness

To understand the relationship between the tip radius and the field emission current, one has to remember that the electrostatic field at the surface of an object increases at regions of high curvature. If a voltage V is applied to a sphere of radius R, the field F at its surface is given by

$$F = \frac{V}{R} \tag{3.11}$$

If we now imagine that our tip is composed of a sphere connected to a conical shank, the resulting electrostatic field at the apex surface will be smaller than predicted by equation 3.11, since the presence of a shank yields a modification in the field lines distribution. The surface electrostatic field for a tip-shaped object can then be approximated by

$$F = \frac{V}{kR} \tag{3.12}$$

where k is the field reduction factor and R is the tip radius [2]. Let us assume for now that k does not depend on the tip radius and can take a fixed value; we will discuss the problematic issue of determining its true value in section 3.2.3. From equation 3.12, one can easily see that for a given applied voltage and field reduction factor, a smaller tip apex radius will yield a higher electrostatic field; we also know from the Fowler-Nordheim equation (eq. 3.6 and 3.10) that a higher electrostatic field will produce a higher field emission current density. If we multiply equation 3.10 by the total field emitting area a (in cm^2) and use equation 3.12 to express the electrostatic field F, we obtain the total field emitted current I (in A) as a function of the tip radius R (in cm):

$$I = a\ 6.2 \times 10^{-6}\ \frac{(\mu/\phi)^{1/2}}{\alpha^2(\mu+\phi)}\ \frac{V^2}{(kR)^2}\ \exp\left[-6.8 \times 10^7\ \frac{\phi^{3/2}\alpha k R}{V}\right] \qquad \text{(A)} \tag{3.13}$$

Equation 3.13 provides us with the explicit description of the relationship between tip sharpness and field emission data: for any tip voltage, the smaller the tip apex radius, the higher the total field emitted current. This principle is the key element behind our quick tip sharpness test.

3.2.2 The Quick Tip Sharpness Test

As was explained in the previous section, monitoring the field emission current drawn from our tungsten tips as a function of the applied voltage is a convenient way to characterize the sharpness of our tips. The experimental setup permitting the acquisition of such field emission data is quite simple. After annealing the tip in the preparation chamber of our UHV system, we leave the tip on the heating stage described in section 2.2.2; however, instead of having this stage connected to a current generator outside the chamber, we now connect it to a voltage supply allowing the tip to be negatively biased at voltages up to 2 kV. Inside the chamber, an oxygen-free copper plate is brought above the tip until the tip-plate distance is about 2.5 cm; this plate serves as the anode collecting the field emitted electrons and feedthroughs let this current be detected outside the chamber.

Equation 3.13 showed that for a given applied voltage, a smaller tip apex radius will yield a higher field emission current. In other words, for a tip to emit a predetermined current value, the required voltage will be lower in the case of a tip with a small apex radius than in the case of a tip with a larger apex radius [57]. Our sharpness test consists in slowly increasing the tip bias until a field emission current of 10 nA can be extracted from the tip. The voltage value allowing this current to be reached is thus a good indication of how sharp the tip is. In practice, we have found that the tips which could emit a current of 10 nA for an applied negative voltage smaller than 800 V were suitable candidates for FIM studies. This method, although not yielding a quantitative description of the tip sharpness, is a very useful diagnostic in determining whether a tip is sharp enough for FIM *before* actually trying to image it with FIM.

An interesting effect that was reported before [21] has been observed while we were testing our tips for sharpness. For tips that did not pass the sharpness test but were very close to (10 nA for 850 V, for example), we would apply a higher bias in order to extract field emission currents up to 5 μA for a couple of seconds and then decrease the bias. This extra treatment, sometimes after several repetitions, would often allow

to lower the voltage required to reach 10 nA by up to 200 V and thus permit these tips to pass the sharpness test! There are two possible explanations to this sudden apparent increase in tip sharpness. The first hypothesis is that drawing such high currents from our tips could result in further cleaning of these tips. One can imagine that a current of 5 μA flowing through the tip could yield an apex temperature high enough to sublimate some of the tungsten oxide that might be left even after the annealing process. Since an oxide layer represents an additional barrier for the field emitted electrons [20, 21], the removal of this layer would undoubtedly be detected as an increase in the field emission current. The second hypothesis is that the high current treatment could induce an atomic rearrangement at the tip apex. As will be explained in section 3.3.2, heating the tip apex in presence of an electric field can lead to the formation of a sharp asperity; the build-up of such a protrusion could then explain the observed change in field emission characteristics.

The quick tip sharpness test presented in this section can save one a lot of time by selecting beforehand the tips that are appropriate for FIM imaging. Furthermore, we saw that the high current treatment, applied once or repeatedly, is a worthwhile technique since it can sometimes help in reducing the voltage needed to extract 10 nA from our tips.

3.2.3 Estimating the Tip Radius from Fowler-Nordheim Plots

While the sharpness test by itself is sufficient to determine if a tip will satisfy the requirements of our FIM setup, a more detailed analysis of the field emission data can lead to a quantitative characterization of tip sharpness by allowing the extraction of a tip radius value.

Estimating the tip radius can be done through a direct application of the Fowler-Nordheim theory on field emission. If we divide equation 3.13 by V^2 and take the natural logarithm on both sides, we obtain:

$$\ln\frac{I}{V^2} = \ln\left[a\ 6.2\times10^{-6}\ \frac{(\mu/\phi)^{1/2}}{\alpha^2(\mu+\phi)(kR)^2}\right] - 6.8\times10^{7}\ \frac{\phi^{3/2}\alpha kR}{V} \tag{3.14}$$

where I is in A, V in V, a in cm^2, μ and ϕ in eV and R in cm. From equation 3.14, it can be seen that a plot of $\ln\frac{I}{V^2}$ versus $1/V$ will yield a straight line of slope $-6.8\times10^7\phi^{3/2}\alpha kR$. This particular way of graphing field emission data is called a Fowler-Nordheim plot and simply requires to record the total field emission current for various applied voltages. Provided that the values of ϕ, α and k are known, it is then a straightforward matter to evaluate the tip radius from the slope of a Fowler-Nordheim plot [2, 47, 51, 53, 62].

We obtained several Fowler-Nordheim plots from our field emission measurements on polycrystalline tungsten tips; some of them will be shown later in this section. It is important to first discuss the choice of appropriate values for ϕ, α and k before attempting to extract a tip radius from our plots.

As was mentioned in section 3.1.1, the work function ϕ of a particular material displays crystallographic anisotropy; it seems indeed rather intuitive that closely packed crystal faces would have a higher work function and thus a lower field emission than loosely packed planes [2]. By definition, a polycrystalline material is composed of many differently oriented crystallites; however, the fabrication process yielding polycrystalline wire – usually a wire drawing technique – results in a preferred grain orientation along the wire axis [2]. For bcc (body-centered cubic) metals like tungsten, this favored orientation is (110) [2, 12]; this has been confirmed for our polycrystalline tips by FIM measurements (see chapter 4). Since the topmost layer of atoms present on the apex of our polycrystalline tips obviously belongs to the (110) plane, it would be tempting to use the work function value corresponding to this particular plane in the analysis of our Fowler-Nordheim plots, as was done by some authors [47]. However, because the tip apex can be described as a spheroidal-looking surface composed of an arrangement of variously oriented flat facets, electrons will be field emitted from several crystallographic planes and not just from the plane perpendicular to the tip axis. Moreover, in the case of tungsten, the (110) plane happens to have the highest

work function ($\phi_{110} = 5.25$ eV [59]) and thus the lowest emission of all planes [2]; this enforces the idea that other adjacent planes with a lower work function (for example, $\phi_{100} = 4.63$ eV and $\phi_{111} = 4.47$ eV [59]) will contribute in great proportion to the total field emitted current. Therefore, our choice of using the average work function for tungsten ($\phi_{tungsten} = 4.5$ eV [50]), which is heavily weighted in favor of the strongly emitting planes [2], as an estimate of the overall work function of our tip apices seems quite reasonable. Note that the particular ordering of the numerous crystallographic planes present on the tip apex can be deduced from FIM images; this will be discussed in the following chapter.

It is common practice to take the image correction factor α to be unity when trying to evaluate the tip radius from Fowler-Nordheim plots [2, 51]. Setting $\alpha = 1$ comes down to ignoring the effect of the image potential described in section 3.1.3. This is acceptable for two reasons. Firstly, in most field emission applications, α actually turns out to be close to unity [2]; secondly, it should be understood that only a rough estimate of the tip radius can be obtained from a Fowler-Nordheim plot since an accurate determination of the values of ϕ, α and k depends to a certain extent on the exact tip apex geometry, which is of course unknown when field emission measurements are performed.

The field reduction factor k is probably the hardest parameter to estimate, since for very sharp tips in particular, its value is highly related to the tip shape and apex radius. In the quest for an appropriate k value, the tip can be modeled, for example, as a paraboloid of revolution, a hyperboloid, a sphere on an orthogonal cone or a sharp pyramidal protrusion on top of a larger hyperboloid base, and a corresponding expression for k can be derived [2, 12, 63]. However, these expressions yield different values of k and it is impossible to know which of these geometries apply to the tip until the tip has been observed under an SEM or a TEM. A systematic study of field emission characteristics along with electron microscopy imaging of several tips has been done and reveals that a value of $k \sim 5$ is adequate for most geometries encountered in practice [2]. Other experiments indicated that k is usually between

5 and 8 for slender tips, and its value can drop to about 3 when the tip is annealed at high temperatures because of the smooth bulbous apex resulting from blunting effects [12]. However, taking this range of values for k appears to be a reasonable estimate only for tips with a radius of at least 100 nm; for much sharper tips, it has been shown [21] that k becomes strongly dependent on the exact tip geometry and can reach values as high as 35. Therefore, from field emission measurements alone, only a range of possible radius values can be found for a particular tip by taking $k = 3$ and $k = 35$ as the lower and upper bounds for k.

As will be demonstrated in chapter 4, a refined tip radius value can be obtained from a FIM experiment; an analysis combining field emission *and* FIM data can thus lead to a useful tip apex characterization without having to resort to direct observation of the tip geometry through SEM and TEM. This is a very important requirement for our future experiments, since we will have to fully characterize our tips before using them for single molecule conductivity measurements, without of course the possibility of taking them out of the UHV system for SEM or TEM inspection.

Figure 3.4 shows a Fowler-Nordheim plot for a polycrystalline tungsten tip; the observed linearity indicates that our field emission data displays the Fowler-Nordheim behaviour predicted by equation 3.14. Using $\phi = 4.5$ eV and $\alpha = 1$, as was suggested in the above discussion, a value of $kR = 65$ nm can be extracted from the slope measurement. Taking $3 \leq k \leq 35$, we obtain for this particular tip a radius R between 2 and 22 nm. Note that the uncertainty on this calculated radius is completely dominated by our gross estimate of the ϕ, α and k values and not by the $I - V$ measurements themselves; this claim is supported by the very small scattering of the data points in this Fowler-Nordheim plot.

Two SEM pictures of this same polycrystalline tungsten tip taken after the field emission experiment are presented in figure 3.5. (The flag shaped feature observed close to the apex is most likely due to some surface contamination which could have happened during the transfer of the tip – in air – between the UHV preparation chamber and the SEM chamber.) From these two pictures showing the tip under

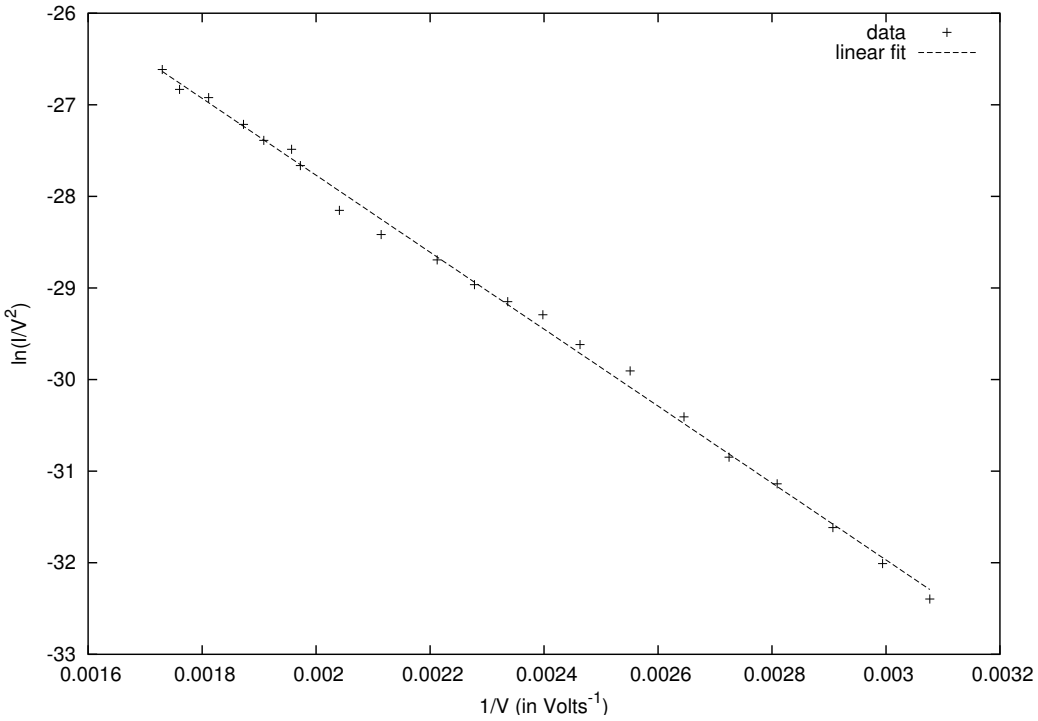

Figure 3.4: Fowler-Nordheim plot for the polycrystalline tungsten tip shown in figure 3.5. The straight line indicates a normal Fowler-Nordheim behaviour; a value of $kR = 65$ nm can be extracted from the slope measurement.

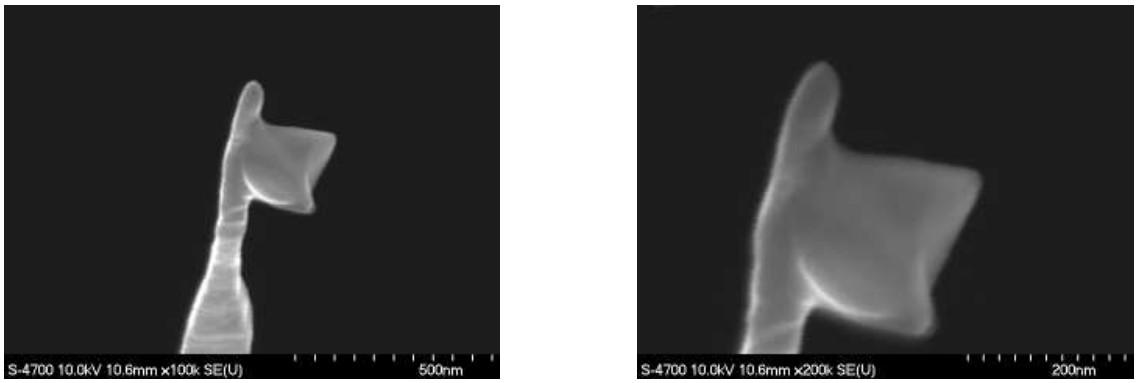

Figure 3.5: SEM images showing under two different magnifications the polycrystalline tungsten tip whose Fowler-Nordheim plot is presented in figure 3.4. From these images, the radius can be estimated to have a value $R \sim 20$ nm.

different magnifications, an apex radius value can be measured. We estimate this radius to be around 20 nm, which is towards the upper end of the range of radii predicted by the corresponding Fowler-Nordheim plot. Note however that it can prove difficult to relate the definition of the tip radius assumed by the Fowler-Nordheim analysis, which is that of a sphere partially buried in a conical shank, to the actual geometry of the tip as seen on the SEM pictures and thus to know precisely how to measure the radius from these pictures. Moreover, one can notice on the right image of figure 3.5 that the apex looks a little fuzzy; this is due to the drift of the tip during SEM imaging which becomes noticeable at this scale and which can then lead to an overestimate of the tip radius. One thing for sure is that choosing $k = 35$ severely underestimates the tip radius in this case; remember that this k value yielded a radius of 2 nm. This makes sense though, since this upper limit for k had been found for tips with an actual radius of 2.5 nm [21], which is obviously not the case here. This is a clear illustration of a limitation inherent to the analysis of Fowler-Nordheim plots; it is almost impossible to pick the right k value for a tip in order to find its radius unless the tip has been observed under an SEM or a TEM, at which point it becomes useless to estimate its radius from a Fowler-Nordheim plot since it can be measured directly from the SEM or TEM image.

Figure 3.6 presents another Fowler-Nordheim plot for a different polycrystalline tungsten tip. The straight line confirms once more a normal Fowler-Nordheim behaviour. In this case, a value of $kR = 137$ nm can be obtained from the linear fit, which results in a radius R between 4 and 46 nm. The corresponding SEM images showing this tip from two viewpoints are shown in figure 3.7; inspection of these pictures yields a radius value of about 40 nm. Again, the radius value obtained from the SEM images is among the larger radii predicted by the plot. However, it should be pointed out that this plot yielded a kR value twice as large as the kR value obtained from the Fowler-Nordheim plot in figure 3.4; this implies that, for a given k, the tip radii will scale proportionally. This is exactly what is observed from the

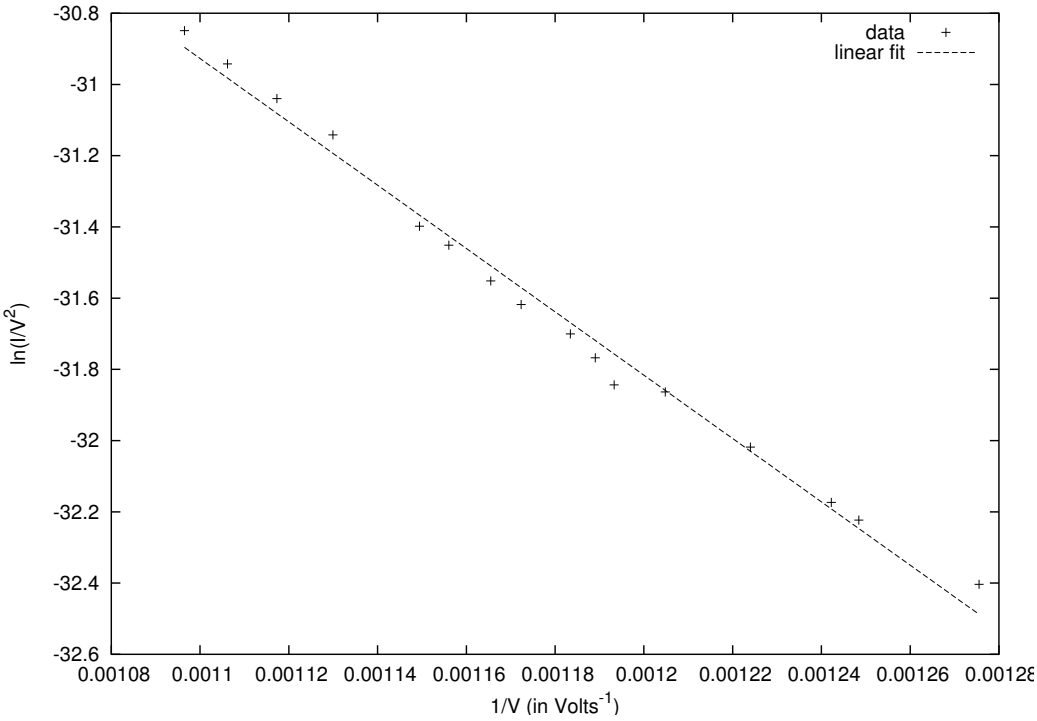

Figure 3.6: Fowler-Nordheim plot for the polycrystalline tungsten tip shown in figure 3.7. Again, the straight line indicates a normal Fowler-Nordheim behaviour; a value of $kR = 137$ nm can be extracted from the slope measurement.

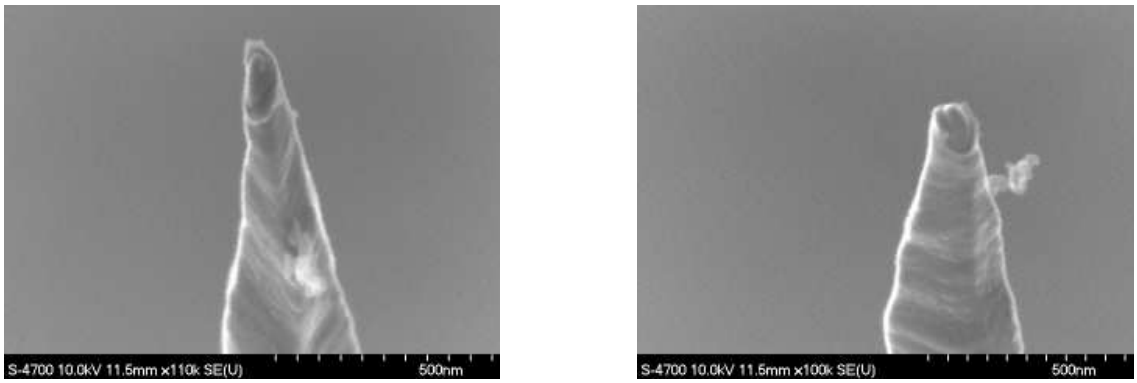

Figure 3.7: SEM images showing two different views of the polycrystalline tungsten tip whose Fowler-Nordheim plot is presented in figure 3.6. From these images, the radius can be estimated to have a value $R \sim 40$ nm.

SEM pictures; the tip in figure 3.7 has a radius twice as large as the tip in figure 3.5 ! Therefore, analysis of Fowler-Nordheim plots, while not necessarily providing us with an accurate value of the tip radius, is very powerful in that it allows a useful comparison between the sharpness of tips, which, due to consistency in preparation, we can assume to have similar geometry.

The latter point is further illustrated in figure 3.8, where Fowler-Nordheim plots corresponding to five different polycrystalline tungsten tips are presented together on the same graph. We know from equation 3.14 that a smaller slope on a Fowler-

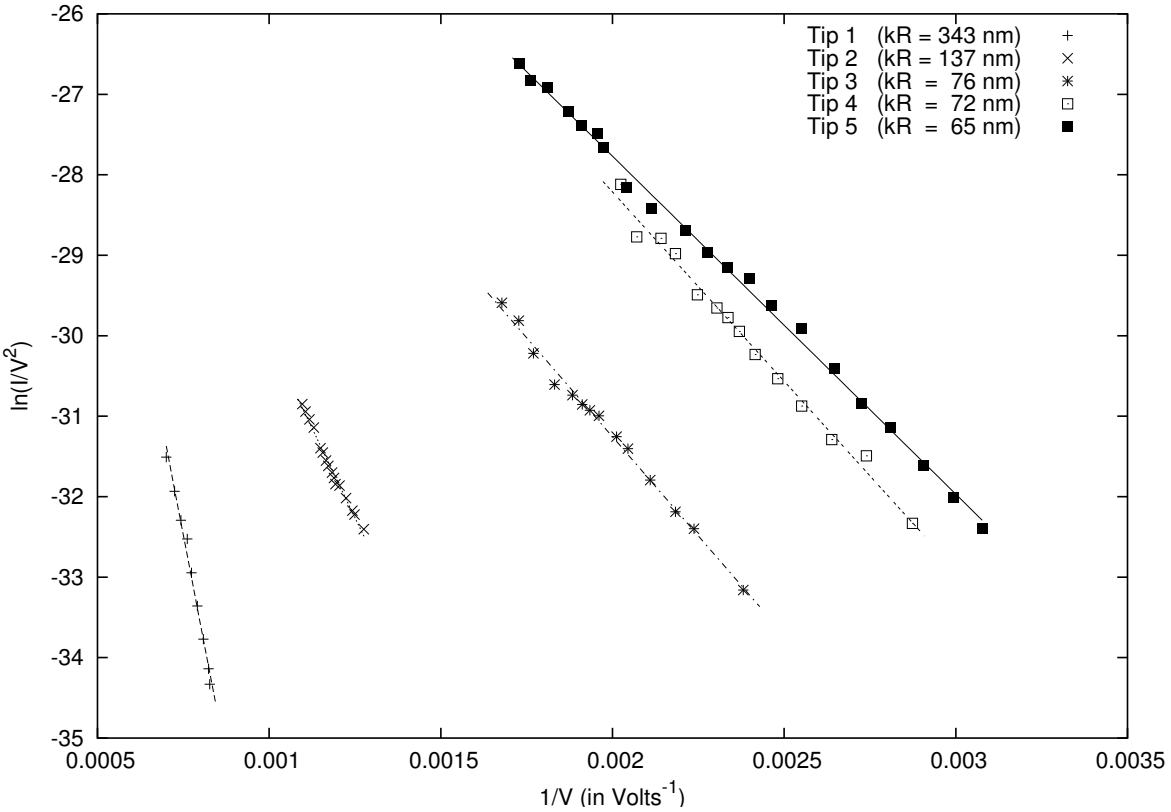

Figure 3.8: Fowler-Nordheim plots corresponding to five different polycrystalline tungsten tips. A smaller slope *and* a displacement of the plot from left to right are the signature of a sharper tip.

Nordheim plot is characteristic of a sharper emitter; a shift of the plot to higher values of $1/V$ (from left to right in figure 3.8) is also a clear indication of a sharp tip since this means that a current is emitted for lower applied voltages [20, 47, 64]. These two

phenomena are nicely combined in figure 3.8; it can be seen that the slope indeed decreases as the plot is shifted to the right. The leftmost curve thus corresponds to the largest tip radius, and the rightmost curve to the sharpest tip. The kR values extracted from the linear fits are given in the graph legend to allow for an easier comparison between the tips. Figure 3.8 is a clear example of a useful application of field emission theory regarding the characterization of our tungsten tips.

3.2.4 Limitations of the Fowler-Nordheim Theory

Upon recalling the assumptions on which the Fowler-Nordheim theory of field emission is based – the emitter is a one-dimensional smooth infinite plane with a uniform work function, one can wonder why this theory should at all apply to tip shaped emitters. It turns out that a planar metal-vacuum interface is a valid approximation for a tip shaped emitter as long as the potential barrier width through which emitted electrons tunnel (see figure 3.2 and 3.3) is markedly less than the radius of curvature of the emitter apex [65]. Combining equations 3.4 and 3.12, a coarse estimate of the barrier width can be obtained:

$$x_{barrier} = \frac{\phi kR}{Ve} \tag{3.15}$$

Note that equation 3.15 shows that for a fixed radius, the barrier width decreases when the applied voltage increases and for a fixed voltage, the barrier is smaller for a sharper tip; since a small barrier means a high field emission current, equation 3.15 is in agreement with the previous discussion on field emission. Using kR values similar to the ones displayed in figure 3.8 and computing $x_{barrier}$ from equation 3.15 for typical field emission voltages V ($\sim$ 0.3 to 2 kV), the potential barrier width can be estimated to less than an angstrom up to a few tens of angstroms. This rough calculation explains why the field emission characteristics of most tips tend to follow the Fowler-Nordheim theory; the tips encountered in practice usually have an apex radius of at least a few tens of nanometers, which is significantly larger than the barrier width. For these tips, it has been shown that the variation of the electrostatic field over the field emitting portion of the apex is quite small; this is why the apex can

be approximated by an equipotential surface, which is a well known property for a planar emitter [2, 65]. Moreover, the crystallographic anisotropy of the work function of such tips does not appear to cause an obvious violation of the one-dimensional planar approximation [65].

For ultra-sharp tips with a radius of a few nanometers only ($\sim 1 - 4$ nm), significant deviations from the Fowler-Nordheim theory are predicted, since in this case, the apex radius is close to or even less than the potential barrier width. The Fowler-Nordheim theory fails to properly describe the field emission behaviour of these tips since the electrostatic field at the apex surface cannot be considered uniform anymore [63] and thus the potential barrier becomes asymmetric; the simple expression for the image potential given in section 3.1.3 is also no longer appropriate. Corrections to the Fowler-Nordheim theory taking into account these modifications require extremely complex calculations and, to date, only preliminary work has been done [65]. Deviations from the typical Fowler-Nordheim behaviour have been experimentally observed for very sharp tips; it is usually detected as an unexpected curvature in the Fowler-Nordheim plots and attributed to the particular tip geometry or to the motion of atoms on the tip [64, 66, 67].

Examining equation 3.15, one could argue that a potential barrier considerably smaller than the radius of curvature of ultra-sharp tips could be obtained by simply applying a very large voltage to these tips; under such conditions, the field emission data should display a normal Fowler-Nordheim behaviour. In practice however, the high voltages required for such a scenario to happen would undoubtedly cause great damage to the tip apex since the large corresponding field emission currents would induce significant heating and surface diffusion. This therefore means that the useful range of $I - V$ measurements extracted from ultra-sharp tips cannot be analysed by the traditional Fowler-Nordheim theory alone; the application of this theory is then limited to tips with a somewhat larger apex radius.

3.3 Resharpening a Blunt Tip in situ

When one of our tungsten tips fails the sharpness test described in section 3.2.2, it is usually taken out of the UHV system so that the tip holder can be used for the preparation of a new tip. A lot of time could be saved if it was possible to somehow resharpen the blunt tip *in situ* (i.e. within the UHV chamber). As was mentioned in section 2.2.4, some procedures exist that do allow such "recycling" of blunt tips; a brief description of the most common of these resharpening methods follows.

3.3.1 Annealing the Tip in Oxygen Atmosphere

Tip sharpening can result from the interaction of tungsten with oxygen at high temperatures. When the tip is annealed in an oxygen atmosphere, the oxygen reacts with the tungsten atoms at the surface of the tip; this yields the formation of various tungsten oxides, which are volatile at these temperatures. This surface corrosion process leads to an overall removal of material from the tip, provided that the tungsten evaporation rate due to this oxygen treatment is higher than the blunting rate induced by the surface diffusion of atoms on the tip [52]. Therefore, sharpening of the tip will only happen for very specific oxygen pressures and annealing temperatures.

It has been demonstrated that optimal results can be obtained by introducing an oxygen pressure of 5×10^{-4} mbar in a UHV chamber through a gas inlet system and annealing the tip at 1300 K for a few minutes up to many hours; the length of the treatment depends on the initial tip shape and the desired final tip radius [68]. The tip temperature is a very critical parameter; too low a temperature will result in a slow reaction time with no significant sharpening and too high a temperature will cause an increase of the apex radius. It has been reported that the corrosion reaction happens at a preferential rate for certain crystallographic planes; this gives rise to a strong faceting of the tip surface [51, 68] and seems to lead to a particularly efficient sharpening of (111) oriented tungsten tips [68]. However, this method has been successfully used to sharpen polycrystalline tungsten tips as well [47]. Another consequence of the oxygen treatment is the occasional formation of several microtips

at the apex [47, 68]; note that this finger-like structure is not a desirable feature for our tips, as it can cause instabilities during STM experiments.

We tried to apply the surface corrosion technique described above in order to re-sharpen a (111) oriented tungsten tip which failed the sharpness test – a voltage of 1500 V was required to extract a field emission current of 10 nA from this tip. After annealing this tip in an oxygen atmosphere for one minute, its field emission characteristics were monitored again. This time, no field emission current was detected for voltages up to 2 kV, which means that the tip got blunt during the oxygen treatment. This is not so surprising since the annealing temperature, which is a critical parameter in this experiment, was simply estimated from the glowing color of the heated tip. In our case, further investigation of this technique would be worthwhile if we had a better way of controlling the tip temperature.

3.3.2 Creating a Sharp Asperity by the "Build-Up" Process

A popular method to sharpen a blunt tip consists in annealing the tungsten tip in the presence of an electric field with a high gradient in order to create a sharp asperity at the apex [53, 64, 66, 69]. While the oxygen treatment previously described leads to a sharpening of the tip by increasing the tungsten evaporation rate with respect to the surface diffusion rate, the field assisted annealing technique lowers the overall blunting rate by generating a surface diffusion flux opposite to the heat induced matter transport.

The mechanics of the field assisted annealing technique can be explained as follows [66, 69]. When a voltage is applied to a tip, a surface field gradient develops along the tip and this field gradient induces a surface diffusion flux from regions of low field strength to those of higher field strength; since the field increases with curvature, atoms are thus forced to move from the shank back to the apex. This counterbalances the self-diffusion of atoms caused by capillary forces, which was explained in section 2.2.3. For temperatures between 1600 and 1800 K and for an applied voltage of 2 to 3 kV, the directional effect of the applied electric field dominates over the matter transport due to capillary forces and from this, a sharp protrusion can

"build up" at the apex. More specifically, the local rearrangement of atoms leads to an enlargement of some low index planes; this enlargement self-terminates when two neighbouring planes meet each other and a sharp protrusion results from the intersection at the apex of the so-called "build-up" planes.

It has been reported that this "build-up" process works beautifully for (111) oriented tungsten tips; a three-atom protrusion could be routinely obtained from the meeting of the three {112} "build-up" planes (see chapter 4 for more information on the crystallography of (111) oriented tips) [66, 69]. However, the ease with which asperities can be created on the {111} family of planes might prevent this technique from being successfully applied to some other tip orientations: undesired side protrusions from the {111} planes have been observed when annealing a (310) oriented tungsten tip in an electric field [53]. The "build-up" technique also proved to be effective in the creation of sharp (100) oriented tungsten tips; in this case, the protrusion resulted from the intersection of four {110} planes [70].

The sharpening effect can be enhanced if the "build-up" process is combined to the oxygen treatment described in section 3.3.1. The resulting technique is called the corrosion-field process and leads to the formation of a pyramidal microtip erected on top of a support tip of larger radius; for a (111) oriented tungsten tip, this "teton tip" geometry usually ends with a single atom [36, 69].

3.3.3 Sharpening by Sputtering

Ion milling and self-sputtering, which are some of the tip cleaning methods explained in section 2.2.4, could also in principle allow a blunt tip to be resharpened *in situ* since they cause the removal of atoms from the tip surface [22, 34, 44, 64, 71]. However, because these techniques tend to create various defects on the tip surface and thus require a subsequent annealing step to heal out the damage, substantial blunting of the freshly sharpened tip could result if the annealing is not done in a very careful way.

4

Field Ion Microscopy: Study of the Tip at the Atomic Level

Once field emission measurements have confirmed that a particular tungsten tip is a suitable candidate for field ion microscopy studies, this tip is transferred from the preparation chamber of our UHV system into the FIM/STM/AFM chamber for further analysis. The purpose of imaging the tip apex with our field ion microscope is to provide us with a better understanding of its atomic structure and with the possibility of engineering it in a configuration which is optimal for molecular electronics experiments. These useful applications of the FIM in our tip preparation and characterization process will be discussed and illustrated in this chapter, but a thorough description of the field ion microscope will be presented first.

4.1 The Field Ion Microscope

The birth of the field ion microscope in the 1950's was a pivotal milestone in the progress of surface science experimental techniques: for the first time ever, humans could observe individual atoms! The field ion microscope's ability to routinely produce atomically resolved images of metals and alloys and, more recently, of some semiconductors and even ceramic materials lead to great advances in the analysis and understanding of solid surfaces and surface related phenomena [3]. To better appreciate the capabilities of the field ion microscope, this section is devoted to a description of the historical background and working principle of this truly revolutionary instrument.

4.1.1 Historical Introduction

Following the experimental observation of field emission from metals by Lilienfeld in 1922 [34] and the successful quantum mechanical treatment of this phenomenon by Fowler and Nordheim in 1928 [61], E. W. Müller invented in 1936 the first modern surface science instrument: the field emission microscope [60]. Since the advent of the field emission microscope was a crucial step towards the development of the field ion microscope, a brief overview of its basic mechanisms, useful applications and intrinsic limitations is presented below.

The field emission microscope (FEM) is amazingly simple in its design; it consists of a tip shaped emitter, which can be negatively biased to high enough voltages so that appreciable field emission currents can be extracted from it, and a conducting fluorescent screen, which is placed a few centimeters away from the tip apex and serves as the anode [12, 60]. As can be deduced from figures 3.2 and 3.3, the emitted electrons have little kinetic energy as they come out of the potential barrier; this implies that their trajectory tends to follow the field lines at the vicinity of the tip apex [2]. Consequently, the emitted electrons undergo an almost radial projection outward from the tip. The fluorescent screen collects these electrons and provides a convenient way to record a point-projected electron image of the apex surface, as each electron impinging on the screen generates a glowing spot.

The image magnification achievable by a FEM is determined by purely geometrical considerations and basically depends on the opening angle of the field lines at the tip apex; for a typical FEM experiment, the magnification reaches a factor of about a million [60]! Since the apex of the tip shaped emitter is composed of several facets with various crystallographic orientations and thus various work functions, and since the field emitted currents strongly depend on the work function value (eq. 3.5), the highly magnified FEM image will then represent the emission anisotropy corresponding to the crystal symmetry [2, 60]. Planes with a lower work function will emit larger currents and will therefore be imaged as brighter features on the screen, whereas planes with a higher work function will appear darker; this is how the image contrast

is generated in a FEM. This is illustrated in figure 4.1, where a FEM image of a tungsten tip is shown and the various crystallographic planes are indexed. Provided

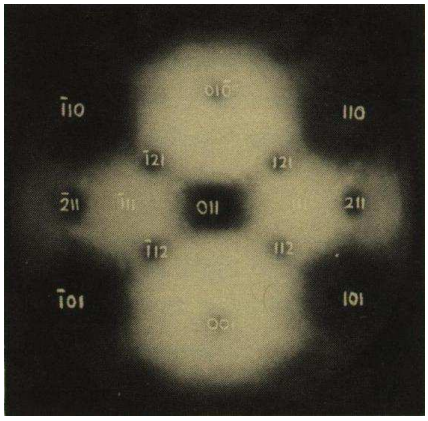

Figure 4.1: Field emission pattern of a clean tungsten tip indexed crystallographically (from reference [2]).

the FEM is operated in a UHV environment, a study of the work function distribution on the surface of a clean emitter can then be conducted. Since the field emitted currents are also affected by local variations in the surface electrostatic field, which are due to the presence of protuberances or asperities and to any abrupt changes in the local curvature of the apex, FEM readily allows the observation of surface disorder, dislocations, grain boundaries, adsorbates, and surface diffusion [2, 60, 72].

Although the FEM was unique in the late 1930's in that it allowed for the first time the visualization of various physical phenomena happening at surfaces, its lateral resolution was not high enough to yield images where atoms could be individually distinguished. The two intrinsic limitations on the resolution of the FEM are, in order of importance, the nonzero lateral component of the velocity of emitted electrons and the diffraction effects caused by the electrons' finite de Broglie wavelength [2, 3, 60]. The first limitation can be understood by remembering that most field emitted electrons originate from the vicinity of the Fermi level, since this is where the potential barrier is narrowest. These electrons thus have a kinetic energy which, while being small enough in comparison with the accelerating potential to somewhat constrain

the emitted electrons to follow the field lines, is not negligible and gives rise to a relatively large velocity component parallel to the emitting surface. Therefore, the statistical distribution of momenta transverse to the emission direction results in a spread in the trajectories of electrons coming from a particular point on the apex and reaching the screen [60]. Since electrons are fermions, their lateral velocity component cannot be reduced by cooling the tip; the electron energy thus imposes an inherent limitation on the resolution of the FEM [3], which is about 2 nm for a tip with an apex radius of 100 nm [2]. The second limitation on the resolution comes from the Heisenberg uncertainty principle; electrons emitted from a region of specified lateral width must display an uncertainty in their lateral momentum since there is a defined bound on the uncertainty of their position. Consequently, electrons emitted from a particular atomic site will diffract, thus limiting the resolving power of the FEM; the resolution on a tip with an apex radius of 100 nm imaged at 10 kV would not be better than 0.8 nm if diffraction effects alone were to be considered [2]. Combining both contributions vectorially [2, 60], one can predict the effective resolution of the FEM to be $\sim 2 - 2.5$ nm [3], which of course cannot lead to atomic imaging.

In 1941, while Müller was studying the adsorption of a layer of barium atoms on the surface of a tip, he realized that by reversing the polarity of the tip voltage and by increasing the applied field, desorption of positive barium ions from the apex surface would occur [3, 12, 73]. He then believed that the desorbed ions, which would follow the field lines, could generate a magnified image of the adsorption sites on a fluorescent screen [73]. Since adsorbed atoms are massive particles, and since they should have a very small lateral velocity component which can be further reduced by lowering the tip temperature, a much higher resolution than that of the FEM can be expected [3, 12]. However, in order to obtain a perceptible image on the screen, a single layer of desorbed ions would not be sufficient; a constant supply of imaging species should be provided instead. Therefore, Müller thought that by introducing in the vacuum chamber a sufficient amount of imaging species in the gas phase and by positively biasing the tip to high enough voltages, an adsorption-

desorption cycle could be maintained and a visible image of the apex surface would result [12, 73]. Müller's ideas directly lead to the invention of the field ion microscope and images with a noticeable improvement in resolution were successfully acquired in the early 1950's. It was found by Inghram and Gomer in 1954 that the actual mechanism responsible for the image formation was not an adsorption-desorption cycle, but rather the field ionization of gas atoms close above the tip surface [3, 12]; this phenomenon will be explained in detail in section 4.1.2. The following years were devoted to determining the parameters yielding an optimal performance of the FIM; under the right conditions, a resolution of 0.2 to 0.3 nm could finally be achieved and in 1956, the first atomically resolved FIM image was obtained [3, 12, 60].

4.1.2 Field Ionization and the Basics of Image Formation

The field ion microscope is quite remarkable for its simplicity and elegance, and for its numerous applications, some of which will be presented in section 4.2. As mentioned in the previous discussion, the FIM is operated in a UHV chamber which is back filled with an imaging gas, usually an inert gas such as helium, neon or argon, to partial pressures typically in the 10^{-5} mbar range. The specimen is a sharp tip, which is positively biased to high voltages of several kV and often cooled down to liquid nitrogen temperatures. A magnified, high resolution image of the tip apex surface is produced on a phosphorous screen placed some centimeters away from the specimen through the physical process called field ionization. More details regarding the FIM experimental setup will be given in section 4.1.4; the purpose of the current section is to provide a description of the mechanisms governing the formation of FIM images, starting by a theoretical overview of field ionization.

Understanding Field Ionization

Field ionization refers to the auto-ionization by electron tunneling of an atom placed under a strong external electric field, and was first suggested by Oppenheimer in 1928 [34]. Through a thorough quantum mechanical treatment of the problem, he demonstrated that the electron in a hydrogen atom could tunnel into free space if a

field of about 20 V/nm was applied [3]. The effect of the field is to lower the potential barrier seen by the electron in the atom so that the tunneling probability becomes appreciable [3, 73]. This can be better understood from a comparison between figures 4.2 and 4.3. Figure 4.2 shows the potential energy diagram for an electron of an atom in free space. As illustrated on this diagram, the valence electron of a neutral atom

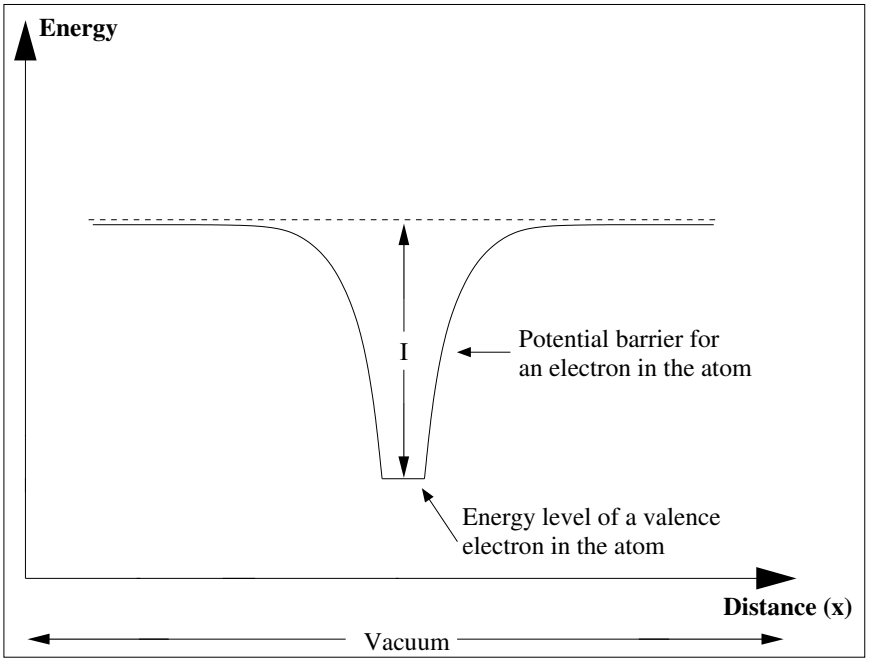

Figure 4.2: Potential energy diagram for an electron of an atom in free space. I is the ionization energy for a valence electron.

is trapped in a coulombic potential well of depth equal to the ionization energy I [2, 3]. The electron cannot escape from this potential well without the assistance of some external source of excitation. Figure 4.3 depicts the situation where an electric field F is now applied; the field causes a severe distortion of the potential barrier profile and the potential barrier width is much lowered on one side [2, 73]. For a high enough F, the barrier width becomes comparable to the uncertainty in the electron's position; the likelihood of the valence electron tunneling through the barrier greatly increases and field ionization of the atom is now possible [3, 73].

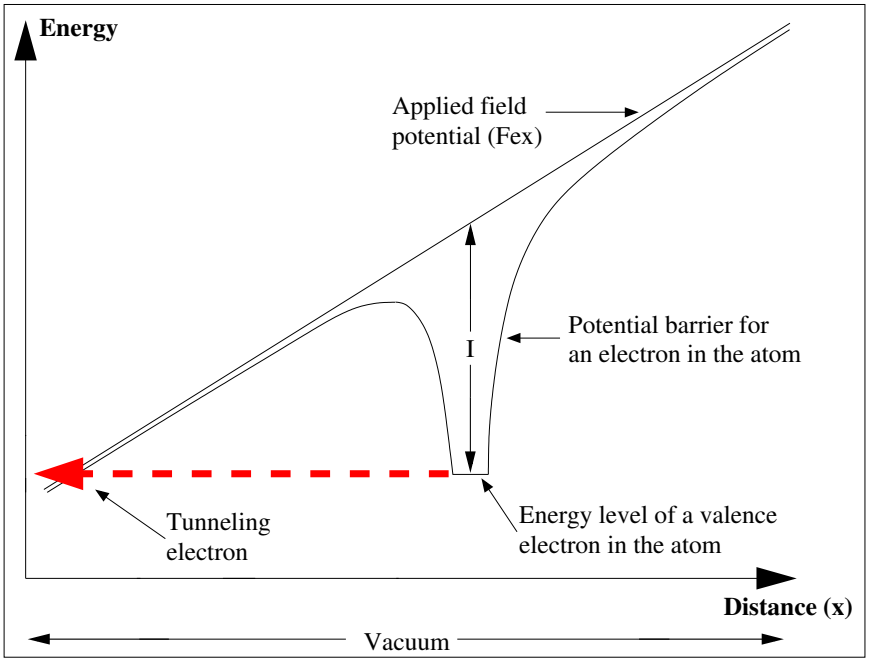

Figure 4.3: Potential energy diagram for an electron of an atom in the presence of an applied electric field F, in free space.

The finite potential barrier width seen by the valence electron of an atom when an external electric field is applied can be even further reduced if the atom is brought in close proximity to a metal surface of work function ϕ and Fermi level μ; this scenario is illustrated in figure 4.4. The interactions between the atom and the metal surface are responsible for the additional decrease in the barrier width and thus enhance the rate of electron tunneling from the atom to the metal surface [3, 13, 73]. A good approximation to the electron potential which takes into consideration the contributions arising from the presence of the metal surface is given by

$$U_{electron}(x) = -\frac{e^2}{|x_i - x|} + Fex - \frac{e^2}{4x} + \frac{e^2}{x_i + x} + \phi \tag{4.1}$$

where x_i is the distance from the center of the positive ion to the plane of the conductor [3, 12, 13]. The first term represents the Coulomb attraction of the electron by the positive ion, the second term is the electron potential due to the applied external electric field F, the third term describes the image potential of the electron and the

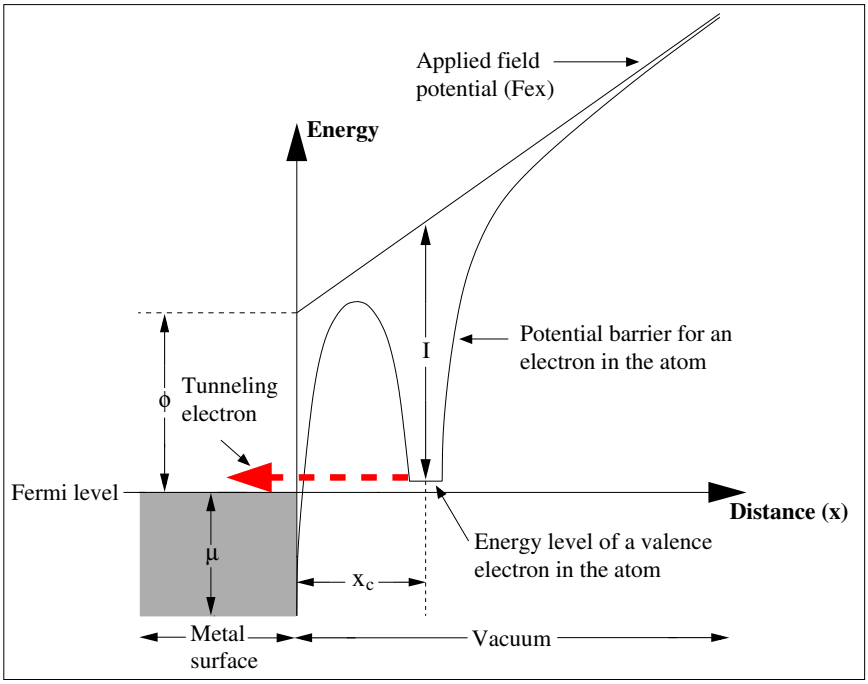

Figure 4.4: Potential energy diagram for an electron of an atom in the presence of an applied electric field F and close to a clean metal surface of work function ϕ and Fermi level μ.

fourth term is the repulsion of the electron by the image charge of the ion in the metal. The fifth term is simply an offset equal to the work function ϕ of the metal due to our choice of coordinates in figure 4.4. Equation 4.1 breaks down for $x = 0$ and $x = x_i$ since it predicts a diverging potential at these positions [13]; however, this one-dimensional expression for the potential can still be used in the calculation of a reasonable estimate of the barrier penetration probability [3]. It is clear from figure 4.4 and from equation 4.1 that the potential barrier strongly depends on the distance between the atom and the metal surface; in fact, it turns out that electron tunneling and thus field ionization of the atom is restricted to very specific distances from the conductor plane. To understand why the ionization region is spatially limited, one should remember that tunneling from the atom to the metal can only happen provided that there is a vacant energy level within the metal to receive the electron. Since for low temperatures, all the electronic levels of the metal below the Fermi

level μ are almost completely occupied, tunneling will be possible only if the ground state of the valence electron in the atom lies above the Fermi level μ of the metal [2, 12, 73]. As indicated in figure 4.4, there is thus a critical distance x_c below which tunneling is prohibited; the range $0 < x < x_c$ is often called the "forbidden zone" for field ionization since in this region of space, the atomic level falls under the Fermi level μ [12, 73]. From figure 4.4, an expression relating the critical distance x_c to the ionization energy I, the metal work function ϕ and the applied field F can be graphically estimated:

$$Fex_c + \phi \approx I \tag{4.2}$$

Equation 4.2 would be more accurate if an image potential and a polarization energy term were included; however, these contributions are usually negligible compared to I and ϕ and can thus be safely omitted [2, 3, 13, 73]. Now for distances x such that $x > x_c$, the field ionization probability quickly drops with increasing x, because the potential barrier becomes wider and the electron is less likely to tunnel through. Hence, the field ionization region for an atom in the vicinity of a metal surface is restricted to a very narrow zone above x_c called the "ionization disk" [3, 72].

Relating Field Ionization to FIM Imaging

The physical process of field ionization described above is of crucial importance in the formation of FIM images. One can readily relate the physical situation depicted in figure 4.4 to that which prevails in a FIM experiment by imagining that the metal surface is actually the tip apex, that the electric field is obtained through the high positive bias of the tip, and that the atoms undergoing field ionization are the imaging gas atoms located within the ionization disk surrounding the tip apex. The resulting positive ions are repelled along the field lines towards the fluorescent screen where a magnified image of the ionization zone is then produced. Figure 4.4 assumes that the kinetic energy of the gas atom is low enough so that it can be field ionized right as it enters the ionization disk; however, the following discussion will emphasize that this is not the case during FIM imaging and that other physical mechanisms are thus involved before field ionization can occur.

When a high positive voltage is applied to a FIM tip, the resulting inhomogeneous electric field F at the tip surface polarizes the imaging gas atoms. The polarized gas atoms are then attracted and accelerated to the tip surface by the electric field gradient [72]. Due to the field, these gas atoms strike the tip surface at a much greater rate than predicted by simple kinetic gas flux theory and the dominant gas flow has been experimentally determined to come from along the tip shank towards the tip apex [3, 13]. Upon arriving at the tip surface, the gas atoms of polarizability α and temperature T possess a fairly large kinetic energy, which is the sum of their polarization energy $\frac{1}{2}\alpha F^2$ and their thermal energy $\frac{3}{2}k_B T$ (where k_B is the Boltzmann constant) [3, 73]. It has been shown that these imaging atoms can greatly reduce their overall kinetic energy by thermal accommodation to the tip, which is usually kept at cryogenic temperatures [3, 72, 73]. The thermal accommodation process happens through a random hopping motion of the gas atoms [73], which is illustrated in figure 4.5. The hopping motion can be explained as follows [3, 13, 73]. The gas atom first

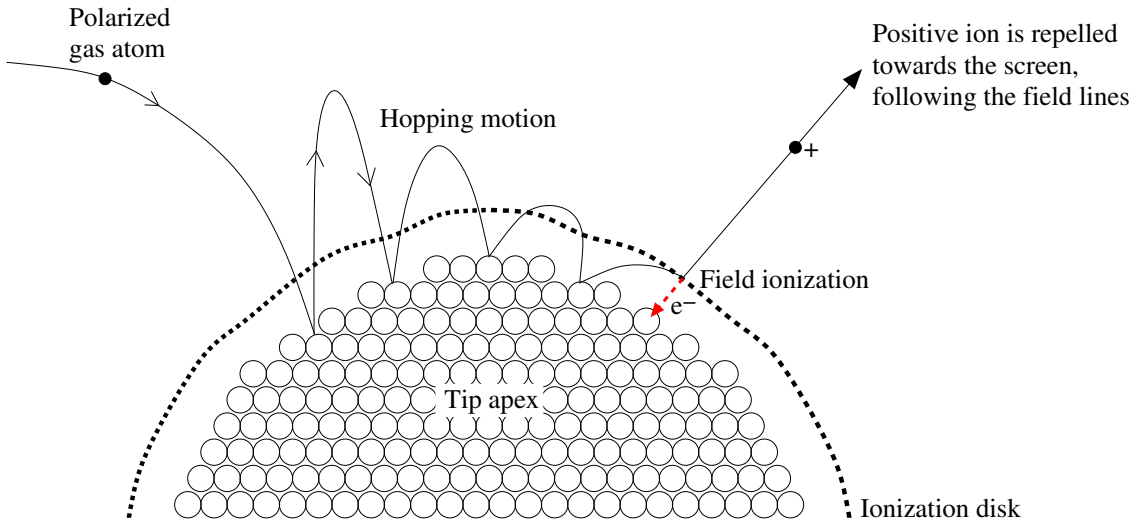

Figure 4.5: Diagram illustrating the mechanisms of image formation in field ion microscopy. The imaging gas atom is attracted towards the tip, then thermally accommodated through a random hopping motion and, finally, field ionized. The resulting positive ion is repelled towards the screen and a bright spot is produced upon impact.

strikes the tip apex with its full incoming kinetic energy and bounces back from the surface, loosing some of its energy to the lattice. Provided that enough energy has been shed during the impact, the decelerated gas atom will not be able to escape from the dipole attraction of the tip and will be drawn back to the tip surface by polarization forces. The gas atom will then execute a series of hops of decreasing amplitude, passing each time through the ionization disk with a reduced velocity and thus an increased chance of being field ionized. It is believed that 50 to over 200 jumps are usually required to thermally accommodate the gas atom to the tip temperature [3]. When this thermal accommodation process has sufficiently reduced the velocity of the gas atom, the latter lingers in the region of high ionization probability and is very likely to undergo, at some point, field ionization. To get an idea of the size of this ionization region, it should be noted that for most imaging gases and tip materials, equation 4.2 predicts that the ionization disk is located about 0.4 nm above the apex surface; studies of the energy distribution of the field ionized gas atoms have also shown that this disk is usually less than 0.02 nm thick when best imaging conditions prevail [3, 12, 73]. Therefore, as is summarized in figure 4.5, it is only after the imaging gas atoms have been polarized, thermally accommodated and field ionized that an image will be formed on the screen, by an almost radial projection of the positive ions from the tip apex surface.

In the early years of FIM, it was believed that the strong electric field at the tip surface would ionize *all* gas atoms in its vicinity, but it has been found later on that this was actually not the case [72, 73]. As was mentioned above, the hopping amplitude decreases with each hop due to the loss in kinetic energy and so if the gas atom has not been field ionized when the hopping height becomes less than the critical distance required for field ionization, it will be confined within the forbidden zone where it cannot be field ionized anymore [3]. It is thus interesting to understand what happens to these gas atoms which do not field ionize during their random hopping motion. A possibility is for them to escape along the tip shank back to free space; however, particularly at low tip temperatures, these well accommodated gas atoms are likely to

condense on the tip surface [3, 12, 73]. This is called field adsorption of gas atoms and it is characterized by a short-range, field induced dipole-dipole bond [73]. Therefore, during FIM imaging, the tip apex is not free of surface contamination; it is actually covered with a layer of field adsorbed gas atoms. It has been demonstrated that these adsorbed gas atoms greatly enhance the thermal accommodation and the tunneling probability of the hopping gas atoms [3], but a clear and quantitative understanding of the mechanisms by which field adsorption facilitates field ionization is still lacking [12]. Due to this coverage of the tip apex, the overall imaging process is a lot more complicated than that which is illustrated in figure 4.5 [12, 60]; however, the latter diagram provides a satisfying enough explanation of the basics of image formation. Note that these field adsorbed gas atoms desorb as soon as the tip voltage is turned off and only the zero-field surface concentration remains [73], which is negligible for temperatures significantly above the condensation temperature of the gas [3].

In field ion microscopy, the image contrast is basically determined by the variations in the field ionization rate across the tip apex surface [12, 71]. The field ionization probability is a sensitive function of the local electric field and for regions of the tip apex where the field is stronger, the following consequences are expected: a higher concentration of gas atoms will be locally attracted, the tunneling barrier width seen by the valence electrons will be lowered, and the number of field adsorbed gas atoms will be increased [3, 12]. Combining these three factors together, one can easily deduce that the field ion current will be much greater where the electric field is higher. Field enhancement happens above protruding atoms since they cause an abrupt change in curvature; therefore, the brightest features observed on a FIM image are atoms at step edges, as well as single atoms and clusters on a flat plane [71, 72]. In-plane atoms are usually not distinguishable on a FIM image because they have a lot of nearest neighbors which prevent the field from being locally intensified; this is particularly true for atoms in densely packed planes [2]. A typical FIM image is presented in figure 4.6; it exhibits a structured arrangement of concentric rings where each ring corresponds to the edge atoms of a particular plane and each set of concentric rings

belongs to a specific crystallographic orientation. In accordance with the previous discussion, most in-plane atoms are not imaged in this picture. Figure 4.6 actually

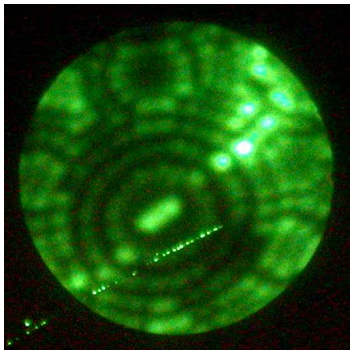

Figure 4.6: FIM image of a polycrystalline tungsten tip acquired at a helium pressure of 2×10^{-5} mbar, a tip temperature of 140 K and a tip bias of 5.4 kV. The typical ring-like structure formed by atoms at step edges is clearly illustrated. As expected, most in-plane atoms are not imaged.

represents the apex of a polycrystalline tungsten tip; it was imaged with a helium pressure of 2×10^{-5} mbar, at a tip temperature of 140 K and a tip bias of 5.4 kV [1]. The determination of the crystallographic orientation of the various planes displayed in our FIM images will be covered in section 4.2.1. As a side remark, it is interesting to compare the resolution observed in figure 4.6 to that of the FEM image presented in figure 4.1; single atoms are clearly distinguishable in the FIM picture, which shows a dramatic improvement over the FEM image where only smeared out field anisotropies can be seen.

As was explained in the above paragraph, an atom with relatively few nearest neighbors will look brighter in a FIM image, due to an enhancement in the local electric field. The effect of the number of nearest neighbors on the field ionization probability above a particular atom is nicely illustrated in figure 4.7. This figure shows two FIM images of a polycrystalline tungsten tip acquired consecutively under

[1] Since all our FIM images are acquired at the same helium pressure of 2×10^{-5} mbar, this detail will be omitted in the subsequent figure captions. Note that the bright line in the bottom left corner of all our FIM images is due to a crack in our screen assembly.

the same imaging conditions and for an identical exposure time. Each of the two atoms pointed out on the left image lost a nearest neighbor during the few seconds separating the acquisition of these images; as a result, they both appear significantly brighter on the right image. The increase in brightness means that a higher field

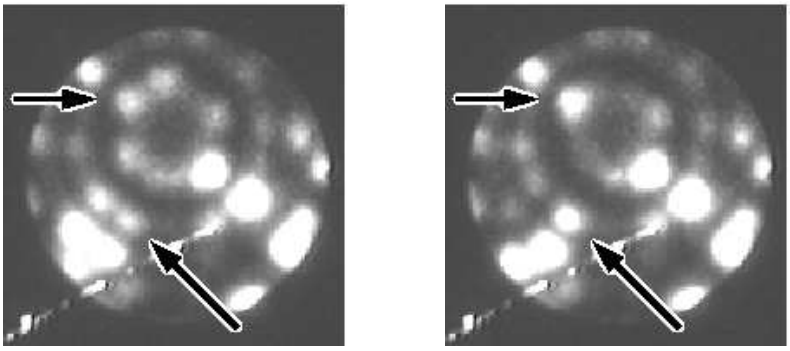

Figure 4.7: Consecutive FIM images of a polycrystalline tungsten tip acquired at 2.8 kV and 140 K. The two atoms identified in the left image both lose a nearest neighbor through field evaporation and thus appear much brighter on the right image, due to a local field enhancement.

ion current coming from these two atoms had reached the screen; this is a clear indication that the field ionization rate above these atoms was intensified upon the loss of nearest neighbors. One can wonder though why some tungsten atoms should suddenly "disappear" from the images; this happens through the physical process called field evaporation, which will be discussed in section 4.2.2. Note that the intensity of the three very bright atoms in the bottom left corner of the left image had already saturated the camera; this is why after the field evaporation of one of these atoms, the increase in the intensity of the two remaining atoms could not be recorded and thus cannot be observed in the right image.

There is a value of the electric field for which the contrast in a FIM image is best and maximum surface detail can be obtained; this value is called the best image field (BIF) and depends notably on the imaging gas used [3, 73]. Although the definition of a "best image" could be somewhat subjective, many investigators seemed to have agreed over the years that fields of 44 V/nm for helium, 37.5 V/nm for neon and 22 V/nm for argon and hydrogen would yield the clearest FIM images [3]. The

existence of a BIF implies that there must be a corresponding best image voltage (BIV) that has to be applied to the tip in order to get the sharpest FIM image [3, 13]. From equation 3.12, we can deduce that the BIV required to obtain the BIF depends on the tip radius; therefore, the BIV will be different for each FIM imaging experiment. Deciding on the BIV can prove to be quite a delicate task, since in reality, the BIV is non uniform over the tip apex surface. Because the BIV obviously depends on the work function, which displays crystallographic anisotropy, and on local variations in the tip apex geometry, a compromise must be made in the choice of its value [13]. If the applied voltage is too low, some planes might not be imaged and only regions of very high field enhancement can be seen [2, 13], provided the exposure time is long enough. On the other hand, if the applied voltage is too high, a blurring of the image occurs and the pattern loses structure [2, 13, 73]. As will be explained in section 4.2.1, some relevant information about the geometry of our tips can be obtained from the experimentally determined BIV value.

4.1.3 Magnification and Resolution of the Field Ion Microscope

The field ion microscope, like its predecessor the field emission microscope, is basically a point-projection microscope and so its magnification M can be obtained by simply considering the geometry of the tip-screen assembly. If the observed specimen and the screen were two concentric spheres, the positive ions would follow a perfectly radial trajectory from the tip surface to the screen; the magnification would then be equal to the ratio of the tip-to-screen distance Z to the apex radius R [12]:

$$M_{sphere} = \frac{Z}{R} \tag{4.3}$$

In practice however, the ion trajectories deviate from a purely radial projection, notably because of the presence of a tip shank [3, 73]. Since the ion trajectories tend to curve inwards in the direction of the screen [12, 74], an image compression factor β has to be included in equation 4.3 so that the image magnification of the FIM becomes

$$M_{FIM} = \frac{Z}{\beta R} \tag{4.4}$$

where $1.5 < \beta < 1.8$ for a conventional tip geometry [3, 73]. Figure 4.8 provides a schematic representation of the magnification process in field-ion microscopy [73]. As

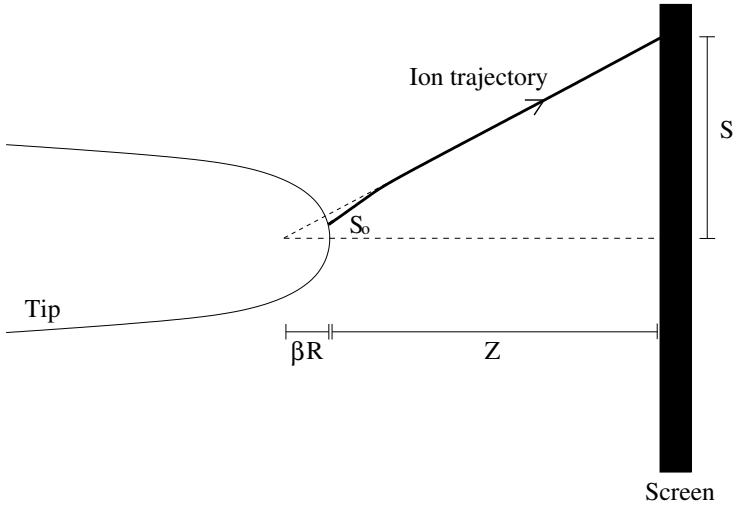

Figure 4.8: Schematic illustration of the magnification process involved in FIM. From geometrical considerations, the magnification M achieved by FIM is found to be $M_{FIM} = \frac{Z}{\beta R}$, where Z is the tip-to-screen distance, R is the apex radius and β is the image compression factor.

can be seen from this figure, the ion is projected almost radially from the tip apex; its flight path is then slightly bent towards the screen. If the quite linear ion trajectories in the vicinity of the screen are projected backwards, they seem to intersect inside the tip, at a distance βR from the apex surface. One can therefore think of the actual ion trajectories as the outcome of a radial projection from a sphere with an "effective radius" βR, which is larger than the measured apex radius R. From figure 4.8, it is then possible to calculate the FIM magnification from geometrical considerations [73]:

$$M_{FIM} = \frac{image}{object} = \frac{S}{S_o} \simeq \frac{Z + \beta R}{\beta R} \simeq \frac{Z}{\beta R} \tag{4.5}$$

which explains the result presented in equation 4.4. In our setup, $Z = 6$ cm; therefore, for tips with an apex radius of a few nanometers, a magnification of several million times can be reached.

From equation 4.4, one can see that the magnification is inversely proportional to the tip radius; the observed image of a sharp tip will thus appear more highly

magnified than that of a tip with a larger apex radius. Moreover, a sharp tip will require a lower BIV than a blunt tip since its high curvature will enhance the field at its apex. Consequently, a low BIV *and* a high image magnification are the signature of a sharp tip in a FIM experiment. This is clearly illustrated in figure 4.9, where two FIM images of the same polycrystalline tungsten tip are presented. The left

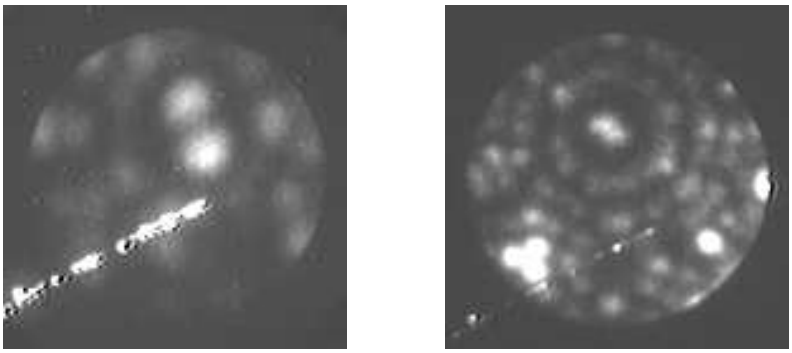

Figure 4.9: FIM images of a polycrystalline tungsten tip. The left image shows the tip when it was still very sharp; it was acquired at a low BIV of 2.4 kV and displays a high magnification. The right image shows the same tip after it got blunt by field evaporation; the increase in tip radius is confirmed by the higher BIV of 4.0 kV and the obvious decrease in magnification. Note that the left image was taken at room T and the right image, at 140 K; the temperature does not affect the magnification, but its effect on image intensity and resolution will be discussed later in this section.

image was acquired first, when the tip was very sharp, at the low BIV of 2.4 kV. The right image was taken later, after several layers of tungsten atoms had been removed from the tip by field evaporation (see section 4.2.2 for an explanation of this physical process) and a smoother, blunter tip apex was left behind. In this case, a higher BIV of 4.0 kV was required, due to the larger radius of curvature. The difference in magnification between these two images is quite impressive: a lot more atoms can be seen on the right image and their individual size is much smaller than on the left image. The very end of the tip apex is located at the center of the set of large concentric rings and on both images, it can be noticed that the tip most likely terminates in two atoms; however, the much higher magnification of the left image implies that the overall radius of the tip is a lot smaller there than it is on the right image.

It should be understood that equation 4.4 only provides an estimate of the average image magnification; in reality, the magnification is not uniform across the imaged apex surface because of regional variations in curvature [73]. It has been shown that the local magnification can vary up to a factor of two from one crystallographic region of the apex to another [12, 74]. However, using a method which will be described in section 4.2.1, it is possible to extract from the FIM image the local radius of curvature r between the center of two crystallographic poles separated by an angle θ, and thus to compute a more precise local magnification M_{local}, which is then given by

$$M_{local} = \frac{L}{r\theta} \tag{4.6}$$

where L is the distance between the two crystallographic poles measured directly on the FIM image [12]. Another approach allows the determination of the local magnification for planes in which all the atoms are resolved; in such cases, one can simply calculate the ratio of the distance between two adjacent bright spots on the FIM image to the known interatomic spacing for the particular plane [12]. However, one should be careful when using the latter technique since the high electric field used in a FIM experiment causes the atoms to adopt a configuration in which the interatomic spacings differ slightly from the tabulated zero-field values [73].

Coming back to figure 4.9, it should be noted that the left image was acquired at room temperature, whereas the right image was taken at a tip temperature of 140 K. While the tip temperature does not affect the magnification achieved by the microscope, it has an interesting effect on the image intensity; this will be briefly discussed here. As one can see on figure 4.9, the "crack" on our screen assembly appears much brighter on the left image; this is due to the use of a longer exposure time in the acquisition of this picture. We have repeatedly observed that FIM patterns obtained at room temperature were much more faint than those acquired at lower temperatures. At low temperatures, the atomic structure of the tip apex imaged on the screen is easily visible to the naked eye while at room temperature, only a long exposure time allows the pattern to be clearly revealed. For comparison purposes, we

should point out that the left image was taken with an exposure time of 8 s, whereas the right image only required an exposure time of 0.4 s.

To our knowledge, the relationship between tip temperature and image intensity is not explicitly treated in the FIM literature; however, we can offer the following explanation as to why a FIM image taken at room temperature invariably turns out to be faint. A faint image is due to a low field ion current and a low field ion current can be caused by a low concentration of gas atoms attracted to the prominent surface sites, a low field ionization probability, and a low population of field adsorbed gas atoms. Although the calculations involved in the determination of gas concentration variations across the tip surface under high fields are extremely tedious and, to date, no realistic models seem to exist, it is nonetheless believed that relative gas concentrations attracted above protruding atoms increase when the tip temperature decreases [12]. The gas concentrations thus tend to be lower at room temperature; a decrease in the gas supply undoubtedly yields a decrease in the field ion current since less imaging gas atoms are available. The second factor to be discussed, which is the ionization probability, is also temperature dependent. When a gas atom strikes a tip at room temperature, the temperature gradient between the gas atom and the tip lattice is quite low and the energy lost upon impact might not be sufficient to prevent the gas atom from escaping the dipole attraction of the tip. Therefore, a significant number of gas atoms might not undergo the hopping motion described in section 4.1.2 and might instead return to free space after a single collision [2]. These atoms have a high velocity and thus spend very little time in the ionization disk; their ionization probability becomes extremely small. The ion current then results from the ionization of atoms which actually perform a series of hops and we just saw that these atoms are not as abundant at room temperature as they are at low temperatures. Finally, we know that field ionization is enhanced by field adsorption of gas atoms on the tip apex surface; however, it has been shown that the likelihood of field adsorption of helium atoms on tungsten at BIF is very high for temperatures below ~ 120 K [3, 12], but drops with increasing temperature [72]. At

room temperature, adsorbed atoms are basically inexistent; this further reduces the ionization probability and thus the field ion current, yielding a fainter image on the screen.

The tip temperature, in addition to its effect on the FIM image intensity, also plays a very important role in determining the resolution of the microscope. By the time gas atoms are field ionized, they have usually lost a lot of their initial kinetic energy by thermal accommodation to the tip; however, they still possess some kinetic energy which, of course, cannot be less than the thermal energy of the tip temperature and is thus of the order of $k_B T$ [3, 73]. Part of this energy manifests as a velocity component parallel to the apex surface; the resulting statistical distribution of the ions' lateral velocities causes a spread in their trajectories and thus limits the resolution of the FIM. Lowering the tip temperature will dramatically improve the resolution of the FIM, as it will reduce the kinetic energy of the well accommodated gas atoms [3, 12, 73]. Remember that this was not the case in the FEM, since the imaging electrons, which are fermions, could not lower their energy by a simple cooling of the tip.

Another limitation on the resolution of the FIM comes from the uncertainty principle; diffraction effects from the finite de Broglie wavelength of the ions will induce a broadening of the ion trajectories exiting from above a particular atomic site. However, this effect will be much less noticeable than in the FEM, because ions are a lot heavier than electrons and their wavelength is thus significantly smaller.

The last main factor limiting the resolution of the FIM is the lateral localization of the ionization disk above imaged atoms [73]. If the applied field is too high, the spatial extent of the ionization zone above a particular atom will increase laterally and the image will appear blurred, whereas if the applied field is too low, the critical ionization distance x_c will be large and the field distribution at the ionization disk will not reflect the atomic details of the surface structure [12]. Only at BIF will the spatial variation of the ionization rate yield the highest resolution. Since the

resolution cannot be better than the size of the imaging gas atoms, it is common practice to take the limitation on the resolution caused by the ionization disk size to be of the order of the radius of the image gas atom [3, 12].

If we define the resolution δ to be the smallest possible distance between two surface atoms for which they can still be distinguished as two separate features on a FIM image, then δ can be expressed as the following vectorial combination of the three limiting factors described above [3]:

$$\delta = \left\{ 16 \left(\frac{\beta^2 k_B T R}{keF} \right) + 4 \left(\frac{\beta^2 R \, \hbar^2}{2keMF} \right)^{1/2} + \delta_o^2 \right\}^{1/2} \tag{4.7}$$

where β is the image compression factor, k_B is the Boltzmann constant, T is the temperature of the image gas atom immediately before ionization, R is the tip radius, k is the field reduction factor due to the tip geometry, F is the electric field at the tip apex, M is the mass of the image gas atom and δ_o represents the size of the image gas atom [3]. The first term in equation 4.7 refers to the broadening caused by the statistical distribution of lateral velocities, the second term calculates the spot size due to the uncertainty principle, and the third term takes into account the spatial extent of the ionization disk. It can be deduced from equation 4.7 that the highest resolution is obtained with image gas atoms which are well accommodated to a low tip temperature, with a small tip radius, a high electric field at BIV and a small gas atom size. Since helium is a very small gas atom and has a high BIF of 44 V/nm, it is thus the best choice for an imaging gas [3, 73]. Under the best experimental conditions, the resolution of the FIM should be ~ 0.2 nm; atomic displacements of ~ 0.05 nm should also be resolved [72]. The fact that we could reproducibly get FIM images with atomic resolution even at room temperature is most likely due to the small radius of our tips.

4.1.4 Our Field Ion Microscopy Instrumentation

The basics of FIM instrumentation have already been outlined in the previous discussion; the purpose of this short section is to point out some of the features which are specific to our FIM setup.

General Design

As explained in chapter 1, our field ion microscope is integrated to our STM/AFM system. This design conveniently allows us to image, characterize and engineer the tip with the possibility of using it immediately after as an atomically defined electrode in a single molecule conductivity experiment. Figure 1.1 shows that the tip holder is magnetically attached to a piezo tube; the latter controls the approach of the tip towards the molecule when the system is in the STM/AFM mode. In the FIM imaging configuration, the STM/AFM sample stage is retracted using piezoelectric motors so that the tip, which points down, faces a screen located 6 cm below. When a high positive bias is applied to the tip in presence of imaging gas atoms, a FIM image of the apex is formed on the screen and can be easily recorded by a camera from outside the chamber.

Imaging Gas

The UHV chamber which houses the FIM/AFM/STM system has a base pressure in the low 10^{-11} mbar range; however, during a FIM experiment, the chamber is back filled with helium to a pressure of 2×10^{-5} mbar. In order to get very pure helium in the chamber, the helium gas is introduced by diffusion through an electrically heated quartz glass leak valve [1]. This diffusion process ensures that only helium atoms can enter the vacuum system; the FIM imaging gas is then virtually free of impurities [73]. To reach and maintain the desired helium pressure, it is necessary to shut off the turbomolecular pump from the chamber by closing a valve [1]; this might however worsen the base vacuum of the chamber. A higher base pressure is not an issue during FIM imaging since the high electric fields prevent the adsorption of most contaminants on the tip surface [21]; only field adsorbed helium atoms cover the

tip surface, but as was mentioned earlier, they desorb when the field is removed. To avoid surface contamination of the tip after FIM imaging, it is important to recover a low base pressure *with the tip still under high fields*; this is done by re-opening the pump to the chamber before turning off the high FIM voltage applied to the tip [21].

Tip Temperature

Our FIM tips can be cooled down using liquid nitrogen. The cryostat consists of an outer vessel, which is filled with liquid nitrogen, and an inner vessel, which contains helium gas. (Note that the helium gas present in the cryostat should not be confused with the helium gas used for FIM imaging; they are in no way related.) The FIM/STM/AFM assembly is in thermal contact with the liquid nitrogen through the helium gas, which then acts as a thermal exchange medium. A detailed description of our cooling system is available in reference [1]. Provided that the liquid nitrogen supply is regularly renewed in the outer vessel, a tip temperature of about ~ 140 K is usually achieved.

Tip Bias

The maximum positive voltage that can be applied to our FIM tips is 7 kV; therefore, only tips which require a BIV lower than 7 kV will yield a useful FIM image. This limitation comes from the breakdown voltage of the insulation on the wire leading to the tip. A higher rated cable would be significantly thicker and rigid, which would increase the vibration coupling to the tip; this would be detrimental when using the tip in STM mode. By equation 3.12, one can relate the BIF to the BIV in the following manner:

$$BIF = \frac{BIV}{kR} \tag{4.8}$$

Knowing that the BIF for helium is 44 V/nm and that, in our case, the highest available BIV is 7 kV, then equation 4.8 predicts that our tips have to meet the condition $kR < 160$ nm in order to be clearly imaged with our FIM. This information about the geometry of our tips can be readily extracted from Fowler-Nordheim plots; in practice however, the quick sharpness test is sufficient to reveal whether or not

our tips are good candidates for FIM imaging. Note that within the FIM literature, it is not unusual to encounter FIM pictures taken at imaging voltages ranging up to 30 kV [12, 72]; under such conditions, tips with a kR value as high as 680 nm can be imaged with helium. This shows how stringent a restriction our FIM setup imposes upon our tip radius values. On the other hand, since molecular electronics studies do require the use of very sharp tips, our range of low BIV values is adequate for our tip characterization purposes.

Image Intensification

During FIM imaging, around 10^3 to 10^4 ions are projected every second from above each atomic site [3, 13]. For a typical tip, this corresponds to a total gas ion current of about 10^{-14} to 10^{-12} A [12, 21, 73]. If this small ion current is directly used to produce an image of the tip apex on the phosphorous screen, a very faint image will inevitably result. This is because heavy particles such as helium ions do not efficiently convert their energy into light upon impact with the phosphorous screen; their so-called "absolute phosphor efficiency" is usually only about 1 % [12, 13]. Moreover, phosphor damage may possibly occur due to this bombardment of heavy particles [60]. Some form of image intensification is thus highly desirable and in our FIM, this is achieved by letting the ions strike a microchannel plate (MCP) located just above the phosphorous screen. A MCP is a thin circular glass plate which consists of a well ordered array of many millions of very fine pores. Our MCP is 4 cm in diameter and 0.5 mm thick; each pore has a diameter of 10 μm and the center-to-center spacing between each pore is 12 μm. To illustrate the typical honey-comb structure of a MCP, three pictures showing an intact region of one of our old and damaged MCPs were taken with an optical microscope under three different magnifications and are presented in figure 4.10. A conductive coating made of nichrome covers both sides of our MCP and when a voltage of 1 kV is applied between these two electrodes, each pore acts as an electron multiplier tube. When the helium ions hit the MCP, they generate secondary electrons which are accelerated down the pores; during their descent, these electrons quickly multiply by undergoing several collisions with the

walls of the pores [12, 13, 73]. For each incident ion on the front surface of the MCP, about 10^3 to 10^4 electrons are obtained at the opposite end [12, 73]. Note that the high magnification of the FIM ensures that ions repelled from adjacent atoms on the tip apex are separated by several pore diameters upon arrival at the MCP surface [73]. By applying a voltage of 4 kV between the bottom surface of our MCP and our phosphorous screen, the emerging electrons are accelerated and focused on the screen. The absolute phosphor efficiency of electrons is much higher than that of ions; it can reach a value up to 50 % [12]. Since our MCP yields a gain in light intensity of $\sim 10^4$, clear and bright FIM patterns can be formed on our screen. With the aid of a mirror placed below our MCP-screen assembly, the FIM images can be recorded through a window port with either a CCD camera or a digital camera. The best imaging conditions are obtained when the lab lights are turned off, when a black cloth surrounds the space between the camera and the window, and when the other window ports of the UHV chamber are covered. Once the FIM experiment is finished, a shutter can be conveniently brought above our MCP in order to protect its fragile structure.

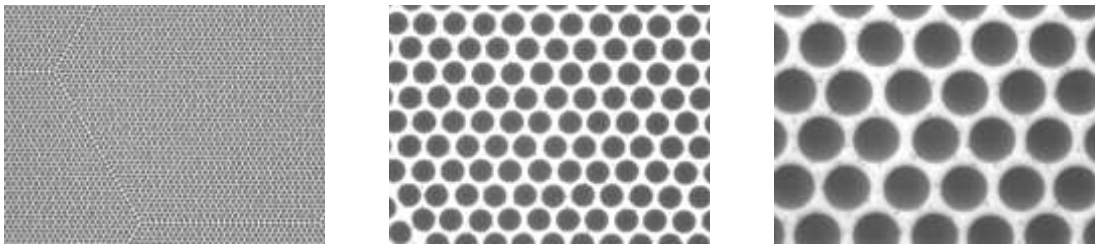

Figure 4.10: Optical microscope pictures showing the honey-comb structure of a MCP. From left to right, these images were taken at a 10X, 50X and 100X magnification respectively. Each dark circle is a pore which, under a voltage of 1 kV, acts as an electron multiplier tube. The diameter of each pore is 10 μm and the center-to-center spacing is 12 μm.

4.2 Useful Applications of the Field Ion Microscope

With a good understanding of the working principles of the field ion microscope, it is now possible to turn our attention to the capabilities of this instrument, in particular those which prove useful in the final stages of tip preparation and characterization. The atomic resolution of the FIM allows the extraction of an apex radius value from the FIM images and can even lead to the three-dimensional, atom by atom reconstruction of the tip apex; this will be discussed in section 4.2.1. Ultimate control on the tip apex shape can also be achieved with the FIM through field evaporation of tip atoms; an explanation of this physical process, along with examples showing how it can be used to atomically engineer the tip apex, will be given in section 4.2.2.

4.2.1 Atomic Characterization of the Tips

Useful information regarding the tip geometry can be obtained from an analysis of FIM images, provided that the image features can be correctly interpreted. As was mentioned in section 4.1.2, a FIM image is composed of sets of concentric rings, each set corresponding to a particular crystallographic orientation and each ring representing the edge atoms of an atomic layer. Therefore, a set of concentric rings should be interpreted as a stack of flat atomic layers, where successive layers are separated by an atomic step whose size depends on the crystallographic orientation of the set. The smallest ring, which is at the center of the set, represents the topmost layer of atoms of that crystallographic orientation on the tip surface. Note that due to the discrete and ordered atomic structure of the apex, each ring is in fact a polygon composed of straight rows of atoms [13]. To understand and characterize this atomic structure of the tip apex surface, which is composed of many different crystal planes, the first step in the analysis of a FIM image thus lies in the correct crystallographic identification of the various planes visible on the image.

Crystallographic Orientation of the Tips

Before attempting to index the various crystal planes imaged on a FIM picture, it is useful to examine the orientation of the wire used to electrochemically etch

the tip, since the plane corresponding to the tip orientation should appear as the central reference pole on the FIM image. As was mentioned in section 2.1.1, our tips were made either from polycrystalline tungsten wire or from single crystal, (111) oriented tungsten wire. Polycrystalline wire is composed of many differently oriented crystallites but since the size of the tip apex is most likely smaller than the size of individual crystallites, the apex is usually part of a perfect single crystal [2, 73]. One might think that the orientation of this single crystal is quite unpredictable due to the polycrystalline nature of the wire. However, as was pointed out in section 3.2.3, the wire fabrication technique results in a preferred grain orientation along the wire axis; in the case of tungsten, the (110) orientation turns out to be the favored orientation. All our tungsten tips made from polycrystalline wire which were imaged with our FIM indeed showed an atomically smooth (110) plane at their apex. Of course, tungsten tips resulting from the etching of a (111) oriented wire invariably displayed a (111) oriented apex.

As an aside, it is interesting to note that although both polycrystalline and (111) oriented tungsten tips have a single crystal apex, the difference between their overall structure is quite striking and can be readily observed through SEM imaging; this is illustrated in figures 4.11 and 4.12. Figure 4.11 shows SEM pictures of two polycrystalline tungsten tips taken from above the tip apex; one can see that the tip surface is rough due to the presence of variously oriented crystallites. Even if the macroscopic tip shape is determined by the necking phenomenon and the drop-off method described in section 2.1.2, it should be pointed out that, at the microscopic level, tip etching generally removes material in a selective way, which means that a local etching rate exists for each crystallographic orientation [15]; since polycrystalline wire is made of grains of different orientations, what starts out as a smooth cylindrical wire quickly develops into a ragged surface as the electrochemical etching progresses. For comparison, figure 4.12 presents two SEM images of a single crystal, (111) oriented tungsten tip showing a top view of the tip. Here the tip surface is much smoother and more uniform than in figure 4.11; this is because a single crystal wire has a constant

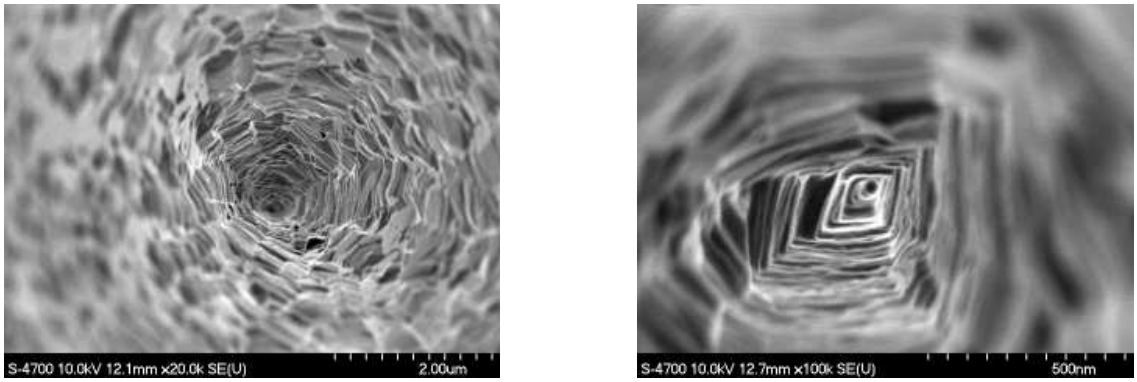

Figure 4.11: SEM images showing a top view of two polycrystalline tungsten tips. The tip surface is very rough, since the tip is composed of differently oriented crystallites.

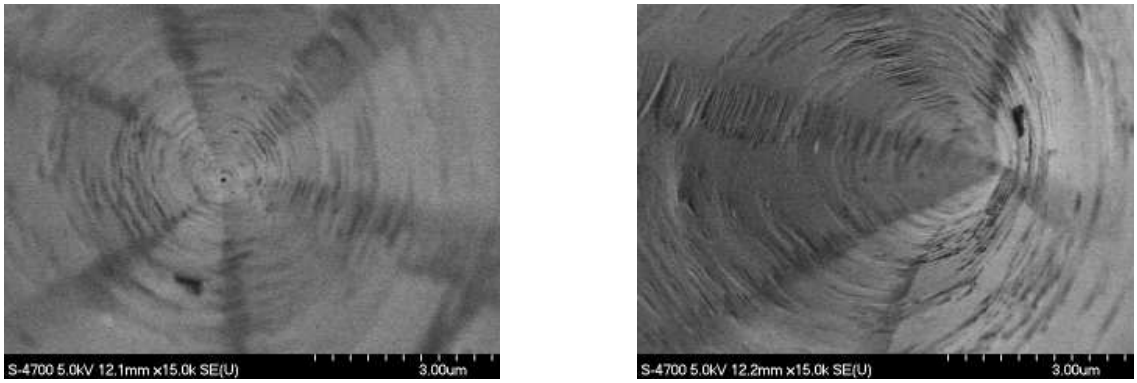

Figure 4.12: SEM images showing top views of a single crystal, (111) oriented tungsten tip. The surface is smooth and uniform due to the constant orientation of the wire. A clear three-fold symmetry can be observed about the (111) direction.

orientation throughout its entire length. The faceting that can be observed on these two pictures is most likely determined by the intersection of the families of planes which have the fastest etching rates. A clear three-fold symmetry about the (111) direction is displayed in figure 4.12; it will be shown later from FIM images that the (111) plane actually exhibits a three-fold symmetry with some families of planes. This is a nice example illustrating that crystallographic information about the tips can be extracted from SEM measurements [51, 75].

Indexing the FIM images

Assuming that the tip apex has a nearly spherical shape and that the field ionized gas atoms follow an almost radial trajectory from the apex surface, it would seem reasonable to compare a FIM image to a geometrical projection of the expected crystal symmetry corresponding to the particular tip orientation in order to assign the correct Miller indices to the various sets of rings present on the FIM image [3, 73]. The standard crystallographic projections which are commonly used to approximately represent a FIM image are the gnomonic, stereographic and orthographic projections; these projections are illustrated in figure 4.13 for a point P on the tip apex surface [12, 76]. As can be seen from figure 4.13, the tip apex has a constant radius of

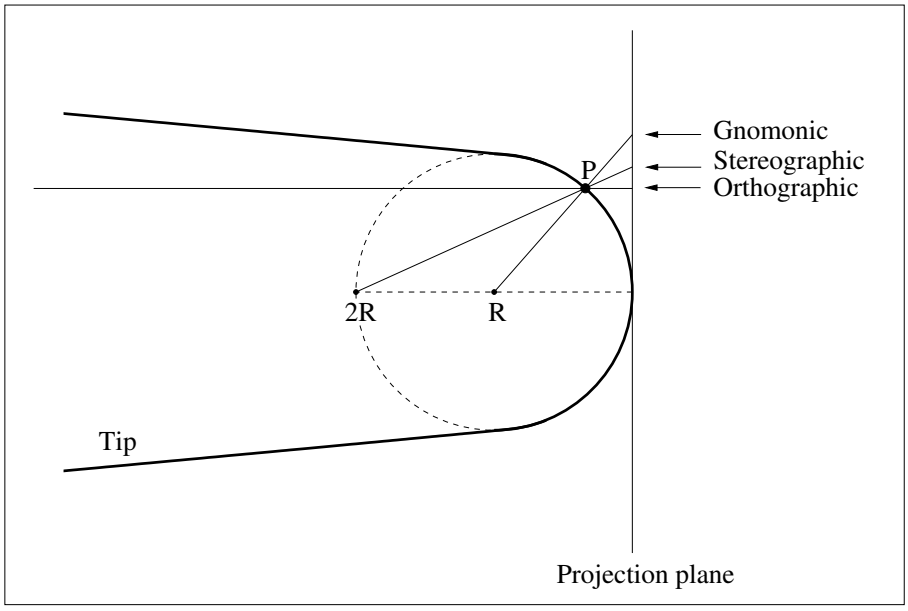

Figure 4.13: Schematic representation of the standard gnomonic, stereographic and orthographic projections of a point P located on the tip apex onto a planar surface.

curvature R, and the projection plane is tangent to the very end of the apex. The gnomonic projection is simply a radial projection of the point P, the stereographic projection is given by the linear projection of P from a distance $2R$ away from the end of the apex, and the orthographic projection is a projection of P from infinity

[12, 76]. However, none of these projections perfectly coincides with the positions of the crystal planes on a FIM image; this can be understood from the complexity of the ion trajectories and their marked dependence on the exact tip apex, tip shank, and tip-screen geometries [12, 13]. It appears that the actual FIM projection of a point on the tip apex surface lies somewhere between the orthographic and the stereographic projections [13, 76]; some intermediate projections have thus been suggested [76, 77], but in reality, a FIM image cannot be accurately described by any particular projection due to the intricacies of the image formation process [12, 13]. However, it has been shown that the stereographic projection provides the most reasonable approximation to a FIM image for points which are located on the apex surface at a radial angle below 45^o [13, 76]; this projection is thus conventionally used for a quick crystallographic identification of the planes on a FIM image [3, 12, 13].

To illustrate the usefulness of a stereographic projection in the analysis of a FIM image, figure 4.14 shows a FIM image of a (110) oriented tungsten tip along with a stereographic projection map for a (110) oriented bcc crystal; both images come from reference [3]. The interpretation of a stereographic map is as follows: each dot indicates the relative position of a particular plane on a FIM image with respect to adjacent planes and thus represents the center of a concentric set of rings; the size of the dots refers to the relative size of the planes as they appear on the FIM image. The size of a plane is related to its atomic step height; planes with the largest interplanar spacings will be more prominent on a FIM image [3, 12]. This is because planes with a large atomic step height are necessarily closely packed planes with a high work function; it will be explained in section 4.2.2 that since atoms belonging to such planes have a lower evaporation field, they will then be preferentially field evaporated when the tip is imaged with FIM, thus exposing larger facets on the tip surface [3, 13]. Note that in figure 4.14, the stereographic map represents a larger area than that which is actually imaged on the FIM picture; some major planes have then been identified on the FIM image to show which part of the map should be considered for an adequate crystallographic identification of the remaining planes on

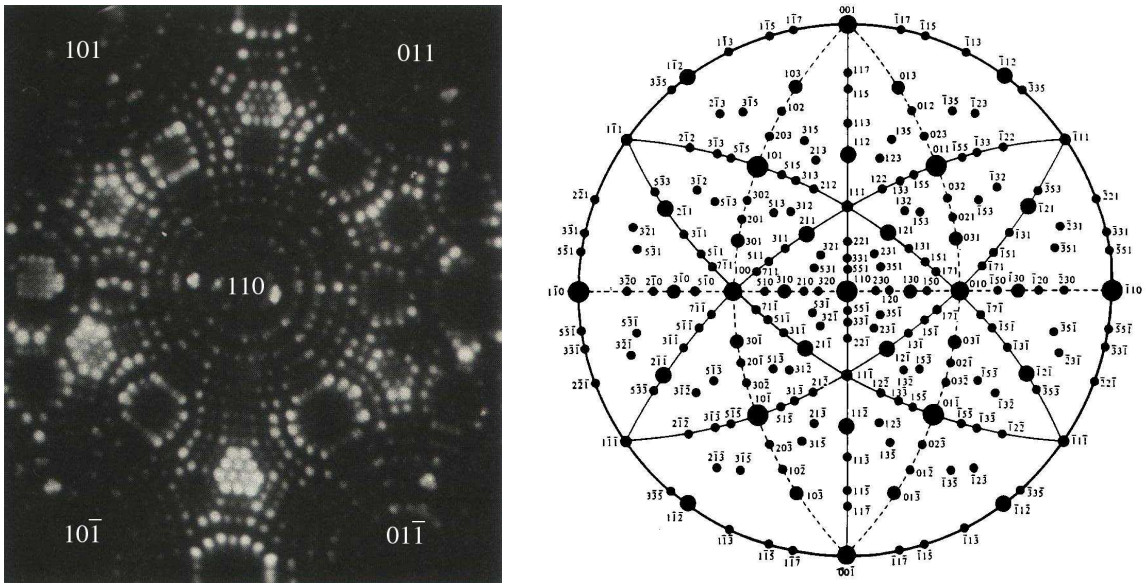

Figure 4.14: FIM picture of a (110) oriented tungsten tip with its corresponding stereographic projection map allowing the crystallographic identification of the imaged planes (from reference [3]). Some planes are indicated on the FIM picture to illustrate the concordance with the map.

the FIM image. The easiest way to assign the Miller indices to the sets of rings is to relate the symmetry elements in the FIM picture to those in the stereographic map and to use the expected prominence of planes to resolve ambiguities [12]. Since the stereographic map has been found to be less accurate for higher index planes, the latter might be harder to correctly identify on the FIM image [12]; to index these planes, other methods involving direct linear measurements on the FIM image can be applied [12, 77].

Upon comparison between the FIM image displayed in figure 4.14 and our own FIM images which were presented earlier in this chapter, one can readily see that our FIM images are much more highly magnified due to the sharpness of our tips and possibly to the geometry of our microscope. Therefore, only a small number of planes are imaged on our pictures, which makes the recognition of symmetric patterns a lot harder. However, higher index planes are not visible on our FIM images and a so-called "reduced projection map" can thus be used to identify the imaged facets

[21]. A reduced projection map is basically a small portion of the stereographic map from which all the high index planes have been removed. As can be seen in figures 4.15 and 4.16, these reduced maps allow for a straightforward characterization of the crystallographic structure of the tips. Figure 4.15 shows the reduced projection map for a (110) oriented bcc crystal [21], along with two fully indexed FIM pictures of distinct polycrystalline tungsten tips; a direct correspondence between the FIM pictures and the reduced projection map can be easily observed. It can also be noticed that the expected prominence of planes indicated on the reduced projection map is pretty well respected on these FIM images. Note that the crystallographic

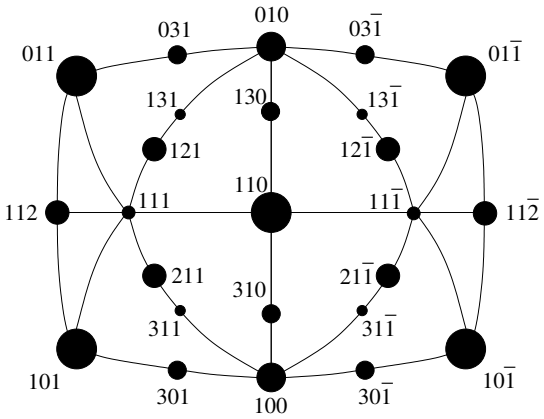

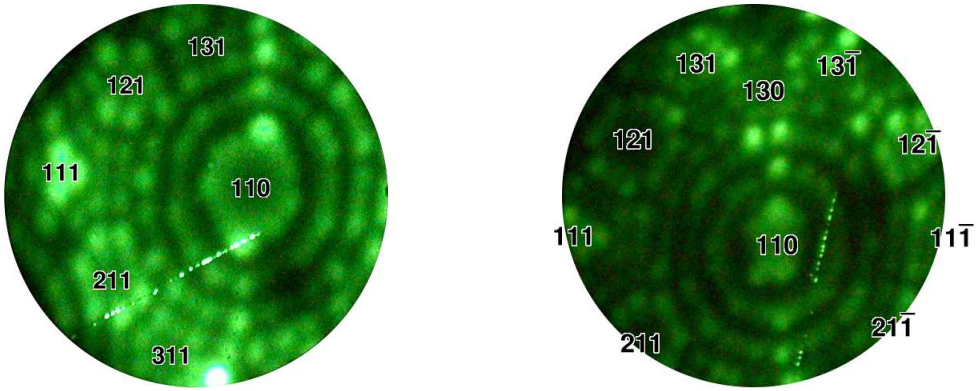

Figure 4.15: Reduced projection map for a (110) oriented bcc crystal along with two fully indexed FIM pictures of distinct polycrystalline tungsten tips. The left FIM image was acquired at 140 K, at a BIV of 4.9 kV; the right image was also acquired at 140 K, but at a BIV of 5.9 kV; note that in both cases, the apex has a (110) orientation.

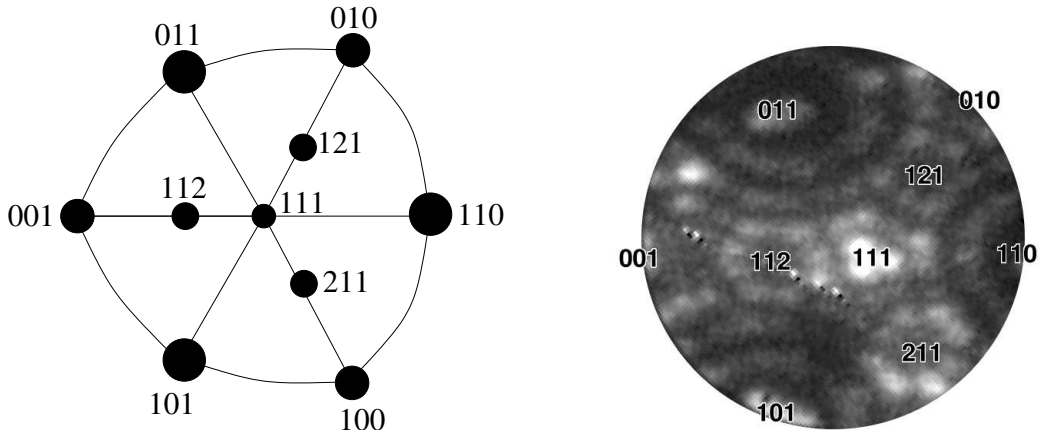

Figure 4.16: Reduced projection map for a (111) oriented bcc crystal along with a fully indexed FIM picture of a single crystal, (111) oriented tungsten tip. The FIM image was acquired at 140 K, at a BIV of 5.9 kV. Three-fold symmetries can be clearly observed about the (111) pole.

identification of the planes in these FIM pictures confirms that the apex of these polycrystalline tungsten tips is really (110) oriented. Figure 4.16 presents the reduced projection map for a (111) oriented bcc crystal [21], as well as a crystallographically indexed FIM picture of a single crystal, (111) oriented tungsten tip. Again, the concordance between the reduced map and the FIM image is evident. From this FIM picture, one can see that the (111) pole has an obvious three-fold symmetry with the {211} planes, and also with the {110} planes; this offers a nice parallel to the three-fold symmetries observed in the SEM pictures of figure 4.12.

Estimating the Radius of the Tips

Knowing the crystallographic structure of the tip apex, it is now possible to calculate in a straightforward manner the average local radius of curvature between the centers of two neighbouring poles. Since the tip apex surface is not a perfectly spherical cap, its local radius varies from point to point; computing the local radii corresponding to different pairs of poles will thus reflect the regional variations in surface curvature. This information is crucial in the characterization of our tips for molecular electronics studies, since it allows the determination of the surface area of the tip which will be in contact with the molecule.

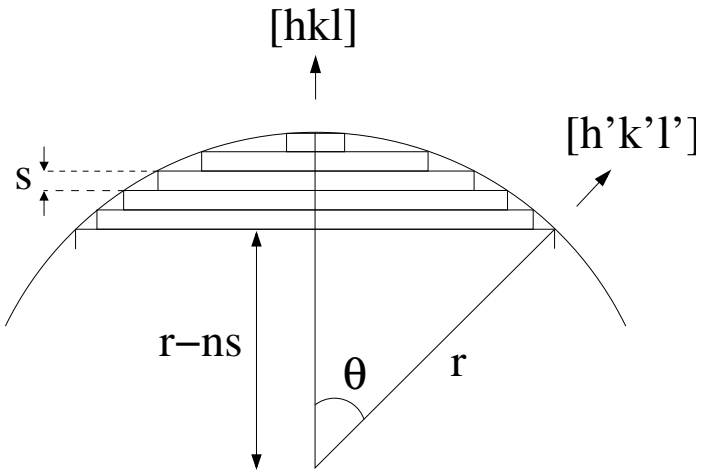

Figure 4.17: Illustration of the "ring counting method" used to determine the local radius of curvature r between two crystallographic poles of Miller indices $[hkl]$ and $[h^{'}k^{'}l^{'}]$ separated by an angle θ. According to the simple geometrical considerations shown on this diagram, the local radius can be found by counting on the FIM image the number of rings n of step height s which can be seen between the centers of the two poles.

To calculate the local radius of curvature between two crystallographic poles, a "ring counting method" is employed, which is illustrated in figure 4.17 [3, 12, 73]. As can be seen from this diagram, a local radius of curvature r can be found between the center of a reference pole of Miller indices $[hkl]$ and the center of a neighbouring pole of Miller indices $[h^{'}k^{'}l^{'}]$, assuming that the local surface between these two poles is spherically shaped. If the two poles are separated by an angle θ and if n rings of atomic step height s can be counted on the FIM image between the centers of these poles, then the following relationship holds true:

$$rcos\theta = r - ns \tag{4.9}$$

Rearranging equation 4.9, the local radius of curvature r can be expressed as follows:

$$r = \frac{ns}{1 - cos\theta} \tag{4.10}$$

In order to calculate r from equation 4.10, the values of $cos\theta$ and s must first be determined. For the cubic lattice, the angle θ between two crystallographic poles is

simply obtained from the definition of the scalar product of the two vectors $[hkl]$ and $[h'k'l']$, and is thus given by [3]

$$cos\theta = \frac{hh' + kk' + ll'}{(h^2 + k^2 + l^2)^{1/2}(h'^2 + k'^2 + l'^2)^{1/2}} \tag{4.11}$$

For a cubic crystal of lattice constant a ($a_{tungsten} = 3.16$ Å [50]), the step height s shown in figure 4.17, which represents the interplanar spacing for the reference pole $[hkl]$, is equal to

$$s = \frac{a}{\delta(h^2 + k^2 + l^2)^{1/2}} \tag{4.12}$$

Note that in the case of a bcc lattice such as tungsten, $\delta = 1$ when $h + k + l$ is an even number and $\delta = 2$ when $h + k + l$ is an odd number [3, 13, 73]. Once r and θ are known, the local magnification M_{local} corresponding to this region of the apex can also be calculated using equation 4.6; to this end, the distance L between the centers of the two poles needs to be directly measured on the FIM image and the angle θ has to be expressed in radians.

Tables 4.1, 4.2 and 4.3 summarize the results of the ring counting method when applied to the three FIM images presented in figures 4.15 and 4.16. Each table shows the analysis for a particular FIM image and displays the local radius of curvature r for several pairs of crystallographic planes separated by an angle θ. According to the previous discussion, $[hkl]$ corresponds to the reference plane with respect to which the n rings are counted and the step height s is calculated. For the sake of completeness, the local magnification M_{local} of the apex region characterized by a local radius r has also been included in these tables. Note that the length L used to compute M_{local} was measured on the FIM images as they appear in this thesis; since, in order to facilitate their analysis, these images have been enlarged compared to the actual size of the screen, the local magnification stated in these tables is slightly larger than that which is achieved by the microscope alone.

$[hkl]$	$[h'k'l']$	$cos\theta$	s	n	r	L	M_{local}
110	111	0.816	2.23 Å	6	7.3 nm	2.5 cm	5.6×10^6
110	121	0.866	2.23 Å	5	8.3 nm	2.2 cm	5.1×10^6
110	211	0.866	2.23 Å	5	8.3 nm	2.2 cm	5.1×10^6

Table 4.1: Results of the ring counting method as applied to the FIM image of the polycrystalline tungsten tip presented in the bottom left of figure 4.15, along with the calculated local magnification.

$[hkl]$	$[h'k'l']$	$cos\theta$	s	n	r	L	M_{local}
110	111	0.816	2.23 Å	7	8.5 nm	2.7 cm	5.2×10^6
110	121	0.866	2.23 Å	6	10.0 nm	2.4 cm	4.6×10^6
110	211	0.866	2.23 Å	5	8.3 nm	2.2 cm	5.1×10^6
110	$12\bar{1}$	0.866	2.23 Å	5	8.3 nm	2.2 cm	5.1×10^6
110	131	0.853	2.23 Å	7	10.6 nm	2.7 cm	4.6×10^6

Table 4.2: Results of the ring counting method as applied to the FIM image of the polycrystalline tungsten tip presented in the bottom right of figure 4.15, along with the calculated local magnification.

$[hkl]$	$[h'k'l']$	$cos\theta$	s	n	r	L	M_{local}
011	111	0.816	2.23 Å	5	6.1 nm	2.3 cm	6.1×10^6
112	111	0.943	1.29 Å	2	4.5 nm	1.4 cm	9.2×10^6
121	111	0.943	1.29 Å	3	6.8 nm	1.3 cm	5.6×10^6
011	112	0.866	2.23 Å	5	8.3 nm	2.0 cm	4.6×10^6

Table 4.3: Results of the ring counting method as applied to the FIM image of the single crystal, (111) oriented tungsten tip presented in figure 4.16, along with the calculated local magnification.

As expected, it can be observed from tables 4.1, 4.2 and 4.3 that the local radius of curvature differs substantially from one crystallographic region of the apex to another; this is particularly striking for the (111) oriented tip analyzed in table 4.3, where the curvature varies by up to a factor of almost 2. Such large variations in the local radius of curvature are commonly encountered in the FIM literature and are mostly due to the crystallographic anisotropy in the work function and in the step height [12, 13]. This confirms that the overall shape of the apex is not hemispherical and that the apex surface cannot be described by a simple analytical function [13]. It should be mentioned however that there is some uncertainty in the number of rings that should be counted on a FIM image; it is sometimes difficult to decide which outer ring of the $[hkl]$ plane coincides with the center of the $[h'k'l']$ plane. We estimate the error on n to be of the order of one ring, which leads to an uncertainty of up to approximately one nanometer on the calculated local radius r.

The ring counting method is a quick and straightforward way to obtain an estimate of the local radii of curvature across the apex surface, provided that the FIM image is clear and that the rings can be easily distinguished. The major drawback is that the method cannot be applied to very sharp tips due to the extremely high magnification of the apex; in such cases, only a very small number of rings belonging to the central pole are imaged and most neighbouring planes are invisible. An example of a FIM picture of a polycrystalline tungsten tip for which the ring counting method cannot be used is given in figure 4.18. As can be seen on this picture, only a few atoms are imaged. The apex terminates in a single atom, and the ring below this atom most likely belongs to the (110) plane. However, since most neighbouring planes are missing and thus symmetric elements cannot be recognized, it is impossible to correctly index this image. It follows that the radius cannot be computed from equation 4.10.

As a side comment concerning the tip geometry, it is interesting to note that FIM imaging can also provide a way to compute, using equation 4.8, the kR value of the tip; it is then possible to compare this kR value to the one extracted from field emission measurements. For example, the tip shown in figure 4.18 was imaged (at

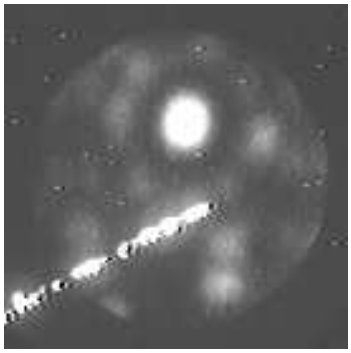

Figure 4.18: FIM picture of a polycrystalline tungsten tip which is so sharp that only a few atoms are imaged; the ring counting method is thus impossible to apply for this tip apex. This FIM image was acquired at room temperature, at a BIV of 2.4 kV.

room temperature) at a BIV of 2.4 kV; since the BIF for helium is 44 V/nm, equation 4.8 yields a kR value of 55 nm. The Fowler-Nordheim plot for this tip was presented in figure 3.8 (this tip corresponds to "Tip 4" in the legend of the graph) and the kR value obtained from the slope was 72 nm. These two kR values differ by about 25% and the discrepancy is probably mostly caused by the quite arbitrary choice of the BIV, which is particularly hard to determine at room temperature due to the lower FIM image intensity and resolution. Even if we know from the variations in the local radius of curvature that the tip apex does not have a perfect hemispherical surface of radius R, it is still useful to make this approximation in order to calculate kR from field emission and field ionization data and to get a quick estimate of the overall sharpness of the tip.

Three-Dimensional Atom by Atom Reconstruction of the Tips

Although the calculation of the various local radii of curvature of a tip from a FIM image provides some very useful insight into its apex geometry, there is no better way to atomically characterize a tip than by reconstructing its apex atom by atom. A careful interpretation of a FIM image can lead to a three-dimensional reconstruction of the tip apex; however, since only a few atoms are present on a FIM picture and because of the two-dimensional nature of the image, this task represents quite a challenge.

To reconstruct our tungsten tips from FIM images, we used a computer program [78] which allows the user to edit a database of atomic positions in space; the available atomic sites are those of a bcc crystal structure with the lattice parameters of tungsten. The user can navigate through various crystallographic planes and through successive layers of a particular plane in order to add or delete atoms; additions and deletions are done by a simple click of the mouse on the selected atomic sites. The progress of the reconstruction can be viewed at any time and from any plane chosen by the user. Since only edge atoms are visible on the FIM image, it is usually easier to start the reconstruction with the smaller planes for which the atoms can be clearly distinguished and counted on the FIM image; once these planes are reconstructed, it becomes possible to infer the size and position of the rings belonging to larger, more open planes. The program outputs a file containing the spatial coordinates of the apex atoms; this file can be fed to the freely available software POVRAY [79] which then produces the three-dimensional rendering of the apex reconstruction.

An example of a three-dimensional, atom by atom reconstruction of a polycrystalline tungsten tip apex from a FIM image is given in figure 4.19. In this figure, the FIM image of the apex, which was acquired at 140 K, at a BIV of 4.9 kV, is presented along with three views of the reconstruction. Only the portion of the tip which appears on the FIM picture has been reconstructed; no attempts have been made to extrapolate the position of atoms located further away from the apex. On the upper right corner, the top view shows a direct correspondence to the FIM image; this strongly suggests that our reconstruction accurately represents the actual geometry of the tip apex. Note that the different shades displayed on this reconstruction reflect the brightness of each atom on the FIM image. Below the FIM image is a side view of the tip, and next to the side view is the apex as seen from an angle. It is interesting to point out that schematic drawings of STM tips often assume an overly sharp, angular tip apex; from a comparison with our reconstruction, it can be deduced that the usual cartoon-like representations of STM tips are not realistic [80].

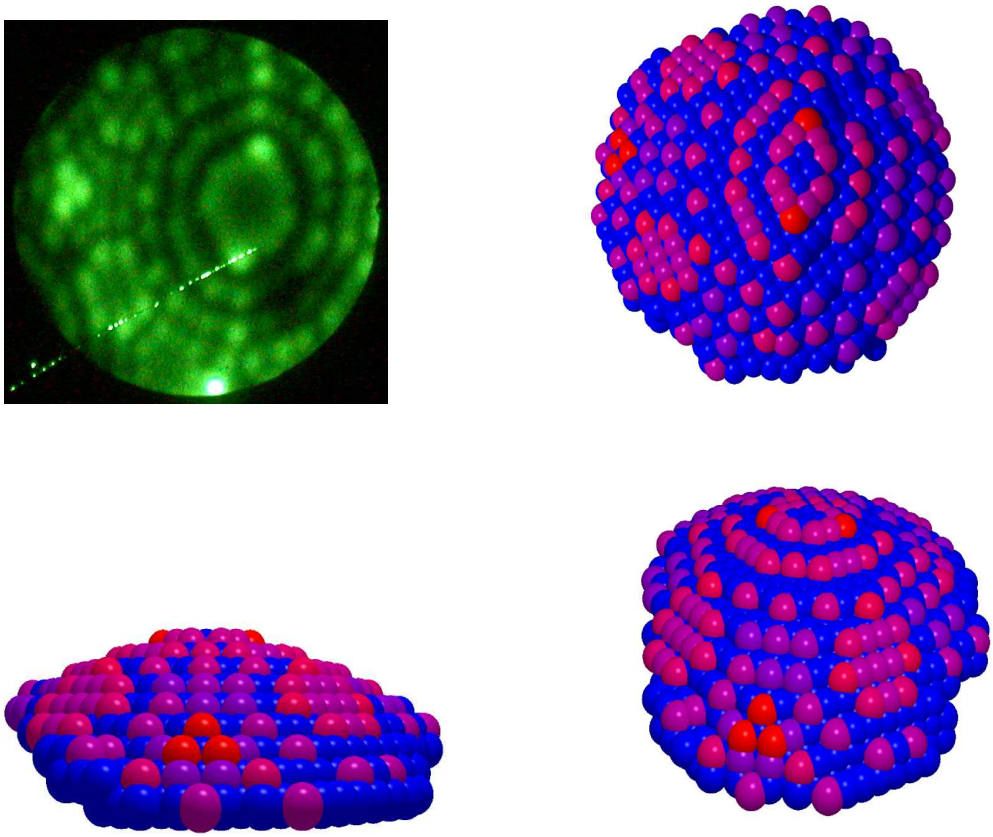

Figure 4.19: FIM image of a polycrystalline tungsten tip acquired at 140 K, at a BIV of 4.9 kV, along with the corresponding three-dimensional, atom by atom reconstruction of the apex presented from three different viewing angles.

From a three-dimensional reconstruction, it is possible to calculate the local radius of curvature between two planes; the results can then be compared to those obtained with the ring counting method. Calculating the local radius of curvature between two planes from the reconstruction is done as follows: by inspection of the reconstruction, the center point of the reference plane is determined and, using the computer program, a normal to that plane passing through its center is dropped; the same is done for the neighbouring plane and the point where these two normals intersect can then be calculated. The radius is obtained by computing the distance between the intersection point and the top of each plane. For example, applying this technique to the (110) and

(111) planes of the reconstruction shown in figure 4.19, one finds that the distance between the intersection point and the top of the (110) plane is 6.0 nm, and the distance between the intersection point and the top of the (111) plane is 5.5 nm. That these two values differ from one another indicates that the surface between these two planes is not spherically shaped, and talking about a "radius" becomes less relevant in this case. This points out a clear limitation of the ring counting method, since the latter assumes that the surface between two neighbouring planes can actually be described by an arc of a circle. Note that for the FIM image shown in figure 4.19, the ring counting method yields a local radius of 7.3 nm between the (110) and the (111) planes, which is larger than both values obtained from the reconstruction. Another limitation of the ring counting method is that there is not always a ring belonging to the reference plane which passes through the center of the neighbouring plane; this is illustrated in the FIM image of figure 4.19, where it is not clear whether 2 or 3 rings should be counted between the (112) and the (111) planes. In this case, taking $n = 2$ gives $r = 4.5$ nm, whereas taking $n = 3$ yields $r = 6.8$ nm; it is expected that the actual radius should be somewhere in the middle. It turns out that the radius obtained from the reconstruction is 5.4 nm with respect to the (112) plane, and 5.5 nm with respect to the (111) plane; these values both fall in between the results obtained from the ring counting method for $n = 2$ and $n = 3$. Therefore, analysis of the reconstruction allows the determination of a more refined radius value than that which is found from the ring counting method.

From the previous discussion, we can conclude that the radius of curvature varies continuously across the apex surface, even between two adjacent crystallographic planes; departures from the spherical approximation will most likely become more apparent for sharper tips. Therefore, the most accurate and reliable characterization of the tip apex is obtained through a three-dimensional, atom by atom reconstruction; this method will prove very useful in our future molecular electronics experiments since the exact atomic structure of the top electrode is believed to be a critical parameter.

As a closure to this section, two more reconstructions are shown in figure 4.20. These reconstructions correspond to the polycrystalline tungsten tip which was presented in figure 4.19, but with slight changes in the atomic structure of its apex, as can be observed from a comparison between the FIM pictures.

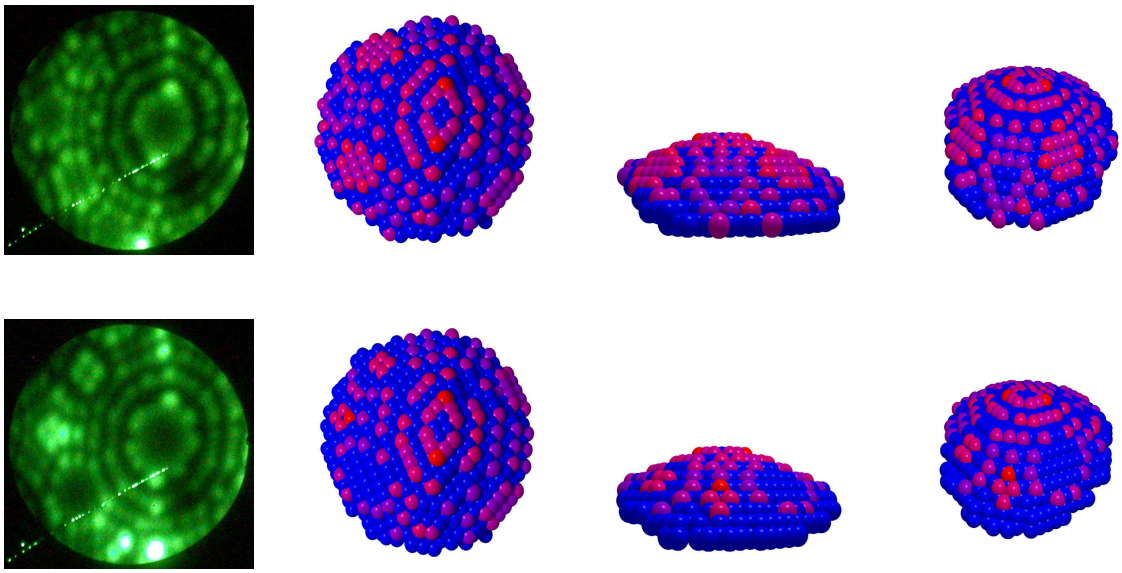

Figure 4.20: Two additional FIM pictures (140 K, 4.9 kV) of the polycrystalline tungsten tip presented in figure 4.19, along with their corresponding three-dimensional, atom by atom reconstructions from three different viewing angles. Note the changes in the atomic structure of the apex in going from one FIM picture to the other.

4.2.2 Atomic Engineering of the Tips

Another useful application of the FIM regarding the preparation and characterization of our tungsten tips is the possibility of engineering the atomic structure of the apex through the physical process called field evaporation. If properly mastered, field evaporation can lead to a controlled removal of individual tungsten atoms from the tip; a stable apex terminating in very few atoms can then be achieved, which is a highly desirable configuration for the top electrode of a two-terminal molecular device.

Understanding Field Evaporation

Under the influence of a strong electric field, atoms bound to the tip surface may escape into vacuum in the form of ions. If the emitted ions were lattice atoms, the phenomenon is called field evaporation; if, on the other hand, these ions were adsorbates on the tip, then the process is referred to as field desorption. There is, however, no theoretical distinction between these two cases; field evaporation is often thought of as a particular type of field desorption [3, 12, 73].

Field evaporation is an extremely complex phenomenon and several theoretical models have been suggested to describe it [2, 3, 13, 72]; as an attempt to outline its basic principles, a simple potential diagram is presented in figure 4.21.

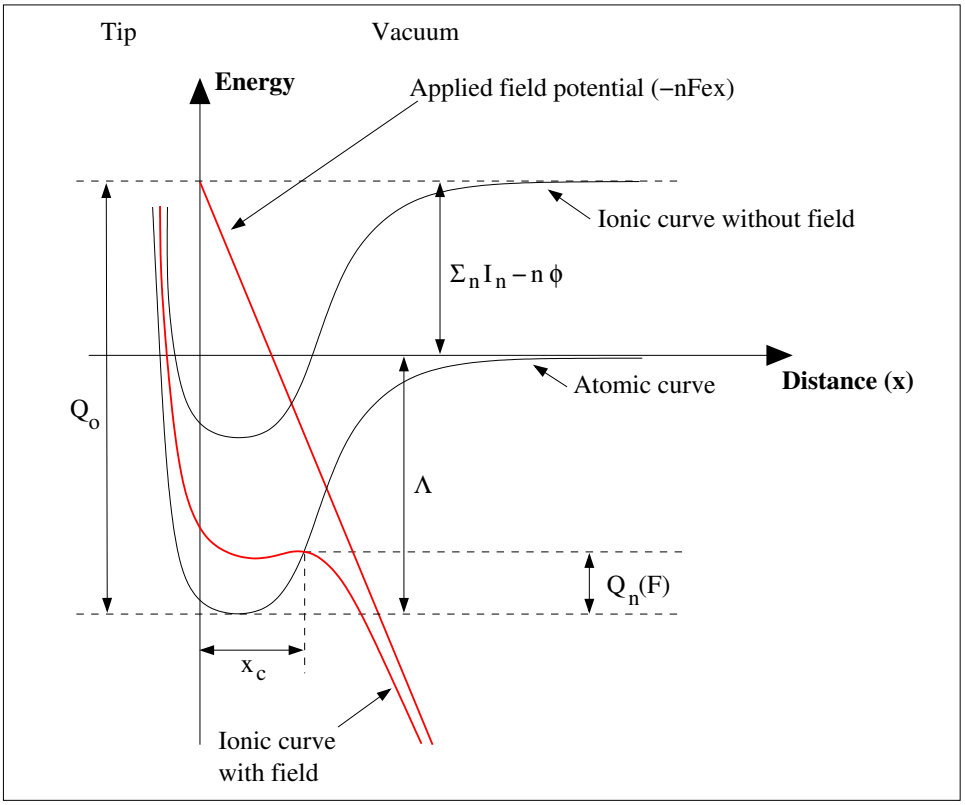

Figure 4.21: Potential energy diagram governing the physical process of field evaporation for an atom bounded to the tip surface. When a high electric field F is applied, the ionic state becomes energetically favorable at distances above x_c and field evaporation can thus occur.

In this diagram, the atomic curve refers to the potential energy of a tip surface atom, whereas the ionic curve represents the binding state of an n-fold charged positive ion on the tip surface. In the absence of an electric field, the ionic curve lies above the atomic curve; in this case, the activation energy Q_o required by an atom to emit out of the surface as an n^+ ion is then given by

$$Q_o = \Lambda + \Sigma_n I_n - n\phi \tag{4.13}$$

where Λ is the heat of sublimation of a neutral atom, I_n is the n^{th} ionization energy of the atom and ϕ is the work function of the tip. Equation 4.13 can be understood as follows: for the neutral atom to be removed from the tip surface, an energy equal to its binding energy must be supplied which is accounted for by the term Λ; then, some energy is required to ionize the atom into an n^+ ion and this energy corresponds to the sum of the ionization potentials $\Sigma_n I_n$ for n electrons; finally, an energy $n\phi$ is released when the n electrons return to the metal [3, 13]. Such ionic evaporation cannot occur by vibrational excitation to an upper state since the atom would thermally desorb before being ionized; therefore, the activation energy Q_o can only be provided by a non-vibrational phenomenon such as photoexcitation [2].

When a high electric field F is applied at the tip surface, the ionic curve is greatly reduced by a potential $-nFex$, as can be observed in figure 4.21. Due to the field, the atomic curve is also slightly shifted to a lower energy [2, 3, 12]; for simplicity, these small polarization effects have been neglected on this diagram. At a critical distance x_c, the atomic curve and the ionic curve intersect and at distances greater than x_c, the ionic state is energetically favorable. Therefore, if an atom gathers enough energy to reach a distance x_c, it may undergo an electronic transition into an ionic state and accelerate into vacuum, away from the tip [3, 12, 13]; the atom is then said to be field evaporated from the tip surface. The activation energy $Q_n(F)$ required for the atom to field evaporate is provided by thermal vibration of the lattice; field evaporation is thus a thermally activated process. The value of $Q_n(F)$ is further reduced when the field is increased since for higher fields, the ionic curve crosses the atomic curve closer to the equilibrium distance of the surface atom. The field evaporation rate is

then dependent on both the applied field and the tip temperature. Note that the exact determination of the critical distance x_c and the activation energy $Q_n(F)$ relies on a detailed mathematical description of the complicated atomic and ionic potential curves, which, to date, seems to be still lacking [3, 12].

Mass spectrometry measurements revealed that the ions emitted from the tip by field evaporation of surface atoms can have various charge states; it has been determined that, for tungsten, the triply charged state (W^{3+}) was the most abundant ionic species [3]. It is believed that thermal activation of the atom yields the initial, singly charged ion and that post-ionization to a higher charge state occurs by field ionization [73]. The probability of such multiple ionization by field ionization is directly related to the strength of the applied field since, as was illustrated in figure 4.4, the magnitude of the electric field establishes the width of the tunneling barrier.

Because of field evaporation, care must be taken in the choice of the imaging gas when planning a FIM experiment. If the BIF of the imaging gas happened to be above the evaporation field of the tip atoms, then the lattice would dissolve before it can even be imaged [73]. Since the average evaporation field of tungsten is 57 V/nm [3] and, as was pointed out earlier, the BIF of helium is 44 V/nm, helium is obviously an appropriate imaging gas for our tungsten tips. (Note that the evaporation field depends to some extent on the work function; this is why the cited value is an average.) Helium cannot be used to image metals such as iron (F_{evap} = 35 V/nm), cobalt (F_{evap} = 36 V/nm), nickel (F_{evap} = 35 V/nm), copper (F_{evap} = 30 V/nm), silver (F_{evap} = 25 V/nm) and gold (F_{evap} = 35 V/nm); for these materials, imaging gases like argon and hydrogen, with a low BIV of 22 V/nm, would be a suitable alternative.

Consequences of Field Evaporation on the Tip Structure

Before demonstrating how controlled field evaporation steps can lead to the engineering of a particular tip apex configuration, it is worth briefly discussing the implications of field evaporation on the tip cleanliness and shape.

An interesting and useful side effect of field evaporation is the removal of contaminants from the tip apex surface [3, 12, 13, 53]; note however that since contaminants are adsorbed atoms, the process by which they leave the tip surface should rather be called field desorption. It has been shown that oxide protrusions on tungsten tips have a desorption field strength significantly lower than the BIF of most imaging gases (as low as 9 V/nm for highly oxidized and loosely bound WO_x [81]); this implies that by the time our tungsten tips are observed at helium BIF, their apex is virtually free of oxide contamination. FIM thus provides a very convenient way to perfect the tip cleaning process started by the high temperature annealing treatment described in chapter 2. One might think that due to the low surface curvature gradient of the tip shank, the electric field at its surface may not reach a high enough value to induce the desorption of contaminants [53] and that the latter might then migrate towards the apex during FIM imaging; however, since a low tip temperature prevents contaminants from diffusing along the shank, the apex surface should stay clean during a low temperature FIM imaging experiment [3].

Another consequence of the field evaporation process is the development of an atomically smooth tip surface as the voltage is gradually raised towards the BIV. Since the local electric field is enhanced above protrusions and sharp edges, the most prominent surface atoms will field evaporate at a lower voltage than the atoms belonging to smooth regions of the apex [12]; a uniform apex surface composed of various well resolved crystallographic poles is thus exposed at BIV. Since the resulting apex shape has a nearly hemispherical end-form, the image distortion is minimal [3] and the surface can look as ordered as the bulk lattice [73]; only under such conditions can a meaningful atomic characterization of the apex be performed. An example of a smooth field evaporated end-form can be observed on our three-dimensional reconstructions presented in figures 4.19 and 4.20.

The major drawback related to the smoothing of the tip shape by field evaporation is the rather poor resolution of the STM images obtained with these tips. Atomic resolution usually results from the presence of some sharp asperity at the apex surface,

but as was explained above, such asperities must field evaporate in order for the underlying atomic structure of the tip to be clearly revealed at BIV. From the atom by atom reconstruction displayed in figure 4.19, one can count 14 atoms on the topmost layer of the apex; an apex terminating in so many atoms can obviously not yield atomic resolution when scanned over a surface. One can then conclude that while FIM is a unique tip characterization tool, it induces substantial blunting of the tip apex which compromises the ultimate resolution achieved by the STM. However, since our tips will be used to locate single molecules on the substrate by STM imaging and to perform conductivity measurements on the selected molecules, their apex must be sharp to yield a high STM resolution *and* atomically characterized so that their structure can be related to the observed $I - V$ properties. To satisfy both of these requirements, a smooth and stable field evaporated end-form should first be obtained at BIV, followed by careful successive field evaporation of single atoms until a sharp apex configuration is achieved; this technique will be explained and illustrated below.

Atomic Manipulation of the Tip Apex by Field Evaporation

Since the evaporation field of the tip material is higher than the BIF of the imaging gas, field evaporation of a single atom from a stable and atomically smooth apex surface is experimentally achieved as follows: while carefully observing the "live" FIM image, one increases the tip voltage very slowly above the BIV until the onset of field evaporation; once an apex atom "disappears" from the FIM image, the voltage must then be quickly lowered back to its BIV value to prevent further field evaporation of lattice atoms. These field evaporation steps are repeated until the desired apex configuration is obtained.

We have successfully applied this technique to a (111) oriented tungsten tip; an example of such atomic manipulation of the apex by controlled field evaporation is presented in figure 4.22. As can be observed from these successive FIM images, the field evaporation steps reduce the number of atoms on the topmost layer of the apex from 5 to 3. The resulting (111) trimer is the sharpest apex we could obtain. We did not manage to engineer an apex terminating in a single atom since the trimer field

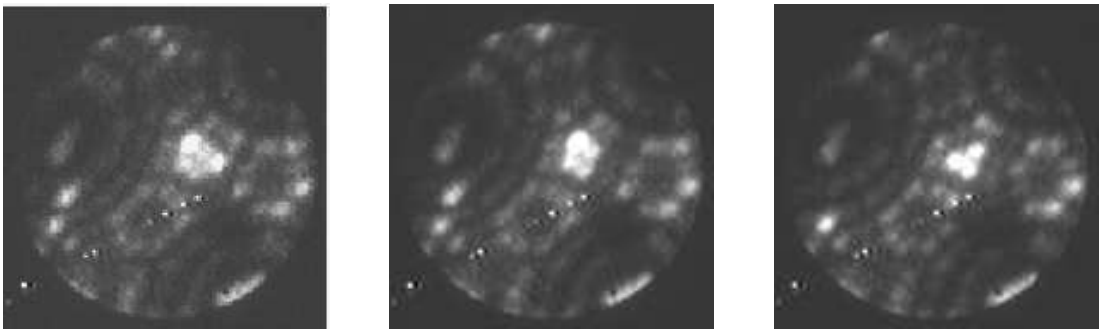

Figure 4.22: FIM images of a (111) oriented tungsten tip showing atomic engineering of its apex by successive field evaporation of single atoms. The images were acquired at 140 K, at a BIV of 5.9 kV. In between each picture, an atom was field evaporated by momentarily increasing the voltage to 6.2 kV.

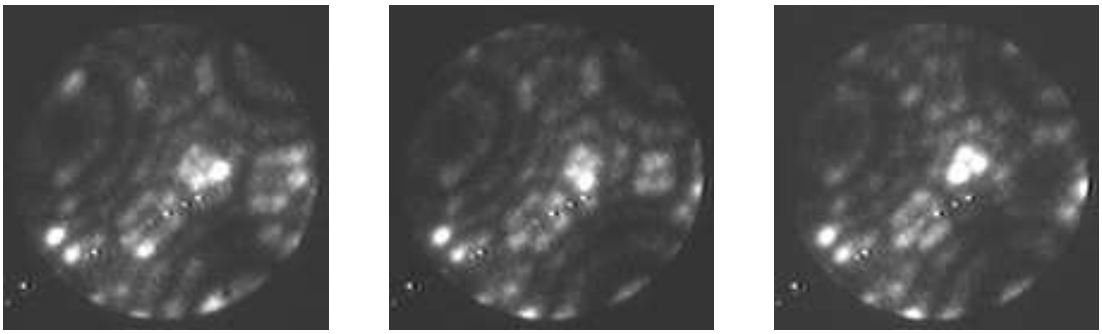

Figure 4.23: FIM images showing another sequence of field evaporation steps for the tip presented in figure 4.22; note that the order in which the apex atoms are field evaporated is different in this case.

evaporated as a single unit; such simultaneous field evaporation of the three remaining atoms on the apex had also been reported before [71]. If the trimer is accidentally field evaporated, it is possible to resume the controlled field evaporation process on the freshly exposed (111) layer in order to recover a sharp apex. This is illustrated in figure 4.23, where another sequence of field evaporation steps for the same tip is shown. This time however, the order in which the apex atoms are field evaporated is different than that which is observed in figure 4.22. While engineering the apex, it is somewhat possible to predict which atom will field evaporate next; since preferential field evaporation happens for atoms above which the local field strength is highest and for which the binding energy to the tip surface is lowest, the brightest edge atom

is then the most likely to leave the surface during the subsequent field evaporation step. However, since the process of field evaporation is statistical in nature, it is very difficult to predict the exact order of the evaporation sequence for more than a couple of steps. Note also that because field evaporation is thermally activated, the field evaporation rate will depend notably on the vibrational amplitude of the surface atoms; controlled removal of single atoms will thus be much easier at low temperatures, due to the higher stability of the atomic structure above BIV. For tips imaged at room temperature, we repeatedly observed that a slight increase of the voltage above its BIV value would cause several atoms to field evaporate.

When planning a molecular electronics experiment, some thought should be given to the choice of the crystallographic orientation of the top electrode, since the ease with which it can be atomically engineered and the stability of the resulting apex configuration depends on the work function of the apex plane and on its activation energy for surface diffusion; the importance of these two parameters is examined below.

Since planes with a higher work function have a slightly lower evaporation field due to the details of their electronic structure and to the larger amount of energy returned to the lattice upon reentering of the electrons in the tip surface [3, 12, 13], and since these planes are closely packed and thus have a larger interplanar spacing which enhances the field at their edges, atoms belonging to these planes will be preferentially evaporated at lower voltages. This explains why the {110} planes, which have the highest work function (ϕ_{110} = 5.25 eV) for tungsten and a large step height s of 2.23 Å, always develop into larger, more open facets on all our FIM images taken at BIV. These planes are quite difficult to engineer in a controlled fashion, due to the lower energy required to field evaporate the atoms. The onset of field evaporation tends to happen at a voltage too close to BIV to allow field evaporation of single atoms; if the voltage is slightly raised above BIV, an entire layer of (110) atoms quickly field evaporates. It has been our experience that any apex configuration obtained on a (110) plane is not stable for more than a couple of minutes at BIV.

The (111) orientation, with a lower work function $\phi_{111} = 4.47$ eV, a more loosely packed structure and a smaller interplanar spacing ($s = 0.91$ Å), is much easier to engineer, as is illustrated in the FIM sequences shown in figures 4.22 and 4.23. Since the gap between the BIV value and the field evaporation voltage is greater for the (111) plane than it is for the (110) plane, the (111) trimer remains very stable at BIV.

Another advantage of the (111) trimer is its high stability against surface diffusion; the diffusion rate of single atoms on the (111) plane is basically negligible even at room temperature [12, 80], since the activation energy for single atom self-diffusion is $\sim$ 1.8 eV for the tungsten (111) plane [71]. Atoms on the (110) plane are much more mobile and surface diffusion on this plane is quite rapid; the activation energy for surface diffusion on the (110) plane is about $\sim$ 0.9 eV [3]. In order to minimize the movement of apex atoms while scanning over a surface or performing STM spectroscopy measurements, a (111) trimer should thus be chosen over a (110) apex configuration.

From the above discussion, we can conclude that a (111) oriented tungsten tip is suitable for molecular electronics studies, since it can be quite easily engineered into a sharp and stable apex terminating in 3 atoms. Since this atomic manipulation is done under FIM imaging, a detailed atomic characterization of the resulting apex can be performed. Moreover, a single atom tip could be obtained by vapour deposition of an atom onto the (111) trimer; this technique has already been successfully developed by Fink [71]. Due to the loosely packed structure of the trimer and the high activation energy for surface diffusion on the (111) plane, the vapour deposited atom creates a very stable protrusion [12]. This single-atom protrusion could be made of a different metal than the underlying tungsten tip, and could even have a lower evaporation field (bulk property) than the BIF of helium, as was experimentally demonstrated by the imaging of gold atoms deposited on a (111) tungsten tip [21]. This would allow a comparative study of the electrical properties of a two-terminal molecular device as a function of the chemical nature of the top electrode's apex atom.

5

Conclusions

A multi-stage tip preparation and characterization technique was studied with the aim of fabricating well defined tungsten electrodes which can be used for contacting single molecules and probing their electrical properties. Using this technique, sharp polycrystalline tungsten tips with apex radii of a few nanometers were reproducibly obtained; furthermore, a single crystal, (111) oriented tungsten tip was engineered into a stable apex configuration terminating in three atoms.

The various parameters influencing the success of the electrochemical etching of tungsten wire in a KOH solution were investigated, and the following conclusions can be drawn. In order to create a sharp tip using the drop-off method, the time required to stop the electrochemical reaction after the lower part of the wire breaks off must be as short as possible to avoid overetching of the tip; an automatic shutting off system monitoring the etching current is thus necessary. A symmetric looking tip with a small aspect ratio can be obtained if the meniscus surrounding the wire at the air-liquid interface is symmetric and short; care should then be taken to avoid disturbing the meniscus while the wire is etching. To this end, the etching station should be isolated from external vibrations, a low DC voltage should be used to limit gas bubble formation at the counter electrode, and the electrolyte concentration should be chosen so that the etching reaction is fast but not violent. It was also found that a pre-etching step improved the reliability of the overall etching process. Since the most problematic issue we encountered concerned the migration of bubbles from the counter electrode towards the meniscus, a possible improvement to our etching setup would be to partially shield the tip from the counter electrode.

Since various contaminants were present on the tip surface after the electrochemical etching, a thorough cleaning procedure was required. Rinsing the tip with distilled water, acetone and ethanol, and drying it with compressed nitrogen gas helped removing some of the contamination, but an oxide layer inevitably remained after this treatment. For further cleaning of our tips, we introduced them into our UHV system, where high temperature annealing of the tips was performed. Since we estimate the annealing temperature to be around 1300 K, most of the oxide layer covering the tip sublimated during this treatment. We found that the drawback of the annealing technique is the substantial blunting of the tips it can induce due to the surface diffusion of tungsten atoms from the apex to the shank. To limit these effects, we chose a low annealing temperature and a short annealing time (2 seconds); we preferred to perfect the tip cleaning with the FIM rather then to take the risk of blunting our tips with a longer annealing time at a higher temperature. A better control on the annealing procedure could be achieved if the temperature was properly monitored; interesting tip sharpening methods for which the tip temperature is a critical parameter, such as annealing the tip in oxygen atmosphere and in presence of an electric field, could also be successfully applied to our tips. We can suggest two techniques which would allow such temperature control. The tip temperature could be obtained from a pyrometer [57], which should be combined with a proper combination of lenses in order to focus the measurement area directly on the tip, or it could be measured from the variations in the resistance of the heating loop, taking into account the temperature gradient along the tip [52, 56].

We examined the field emission behaviour of our etched and annealed tips in order to gain some insight into the sharpness of their apex. We found that field emission data can be used as a quick sharpness test to determine which tips are suitable for FIM studies. A more detailed analysis of field emission characteristics through the construction of Fowler-Nordheim plots lead to the extraction of a kR value for each tip, which can be conveniently used to compare the sharpness of different tips. However, a precise radius value R could not be obtained from such plots, since the

k value strongly depends on the exact tip geometry, which is unknown when field emission measurements are performed.

Sufficiently sharp tips were transferred to the STM/AFM/FIM chamber for further preparation and characterization. From FIM images of our tips, a full atomic characterization of their apex could be obtained. A radius of a few nanometers was calculated using the ring counting method; however, this radius was found to differ between various pairs of crystallographic planes, thus confirming that the apex surface is not perfectly hemispherical. A three-dimensional, atom by atom reconstruction of the apex was achieved using a computer program; such representation of the atomic structure of the apex will prove very useful for our molecular electronics studies, since it allows the calculation of the surface area in contact with the molecule. From the value of this surface area and the force measurements obtained by the deflection of the cantilever beam on which the molecule sits, the pressure exerted by the tip on the molecule can be deduced; since force and current can be measured simultaneously with our combined AFM/STM setup, the conductivity of the molecule as a function of the applied pressure can thus be determined. Such electromechanical measurements should make a significant impact in the field of molecular electronics.

Atomic manipulation of the apex was demonstrated using controlled field evaporation of individual atoms. This powerful technique allows the engineering of our tips into a desired atomic configuration; measurements of the conductivity of a molecule as a function of the atomic arrangement of the top electrode's apex will thus be possible. We determined that (111) oriented tungsten tips were easier to manipulate at the atomic level than the (110) oriented tips. The trimer configuration of the (111) tungsten tips seems particularly interesting for molecular electronics experiments due to its sharpness and stability; it also offers a template on which a single atom of a different material can be vapour deposited. Although it is encouraging that the (111) trimer is stable under FIM imaging, it will be important to ascertain its stability when it is exposed to experimental conditions such as being in electromechanical contact with a molecule. Fortunately, FIM allows the structural integrity of the tips

to be compared before and after a single molecule conductivity experiment has been performed. In the future, tips of different crystallographic orientations will also be investigated, as well as other tip materials.

The natural extension of this work will be to use these atomically defined tips as top electrodes in single molecule conductivity experiments, and to compare the observed electrical properties of the molecule to theoretical predictions. To this end, a close collaboration with Dr. Hong Guo's group at McGill University, which specializes in electron transport theory in nanoscopic systems, has already been initiated. Their expertise in modelling such systems, combined with our experimental results, will enable us to reach a more complete understanding of the electronic properties of molecules.

Bibliography

[1] A. Stalder. *Mechanics and Electronics on the Atomic Scale: A Study using Scanning Probe Methods*. PhD thesis, University of Freiburg, Switzerland, 1995.

[2] R. Gomer. *Field Emission and Field Ionization*. Number 9 in Harvard Monographs in Applied Science. Harvard University Press, 1961.

[3] T. T. Tsong. *Atom-Probe Field Ion Microscopy*. Cambridge University Press, 1990.

[4] C. Joachim, J. K. Gimzewski, and A. Aviram. *Nature*, 408:541, 2000.

[5] P. Samorí and J. P. Rabe. *J. Phys.: Condens. Matter*, 14:9955, 2002.

[6] D. Goldhaber-Gordon, M. S. Montemerlo, J. C. Love, G. J. Opiteck, and J. C. Ellenbogen. *Proceedings of the IEEE*, 85(4):521, 1997.

[7] W. Fritzsche, K. Böhm, E. Unger, and J. M. Köhler. *Nanotechnology*, 9:177, 1998.

[8] K. W. Hipps. *Science*, 294:536, 2001.

[9] X. D. Cui et al. *Science*, 294:571, 2001.

[10] X. D. Cui et al. *Nanotechnology*, 13:5, 2002.

[11] J. J. Palacios, A. J. Pérez-Jiménez, E. Louis, and J. A. Vergés. *Nanotechnology*, 12:160, 2001.

[12] M. K. Miller, A. Cerezo, M. G. Hetherington, and G. D. W. Smith. *Atom Probe Field Ion Microscopy*. Oxford University Press, 1996.

[13] K. M. Bowkett and D. A. Smith. *Field-Ion Microscopy*, volume 2 of *Defects in Crystalline Solids*. North Holland Publishing Company, 1970.

[14] L. E. Murr. *Electron and Ion Microscopy and Microanalysis: Principles and Applications*. Marcel Dekker, Inc., 2nd edition, 1991.

[15] A. J. Melmed. *J. Vac. Sci. Technol. B*, 9(2):601, 1991.

[16] A. I. Oliva, A. Romero G., J. L. Peña, E. Anguiano, and M. Aguilar. *Rev. Sci. Instrum.*, 67(5):1917, 1996.

[17] L. Ottaviano, L. Lozzi, and S. Santucci. *Rev. Sci. Instrum.*, 74(7):3368, 2003.

[18] H. Lemke, T. Göddenhenrich, H. P. Bochem, U. Hartmann, and C. Heiden. *Rev. Sci. Instrum.*, 61(10):2538, 1990.

[19] J. P. Ibe, P. P. Bey Jr., S. L. Brandow, R. A. Brizzolara, N. A. Burnham, D. P. DiLella, K. P. Lee, C. R. K. Marrian, and R. J. Colton. *J. Vac. Sci. Technol. A*, 8(4):3570, 1990.

[20] I. Ekvall, E. Wahlström, D. Claesson, H. Olin, and E. Olsson. *Meas. Sci. Technol.*, 10:11, 1999.

[21] A. Schirmeisen. *Metallic Adhesion and Tunneling at the Atomic Scale*. PhD thesis, McGill University, Canada, 1999.

[22] R. Zhang and D. G. Ivey. *J. Vac. Sci. Technol. B*, 14(1):1, 1996.

[23] U. J. Quaade and L. Oddershede. *Europhys. Lett.*, 57(4):611, 2002.

[24] R. Nicolaides et al. *J. Vac. Sci. Technol. A*, 6(2):445, 1988.

[25] R. Morgan. *J. Sci. Instrum.*, 44(9):808, 1967.

[26] Y. Chen, W. Xu, and J. Huang. *J. Phys. E: Sci. Instrum.*, 22(7):455, 1989.

[27] S. M. Lindsay, T. Jing, Y. L. Lyubchenko, and A. A. Gall. United States Patent '5,630,932', May 20, 1997.

[28] P. J. Bryant, H. S. Kim, Y. C. Zheng, and R. Yang. *Rev. Sci. Instrum.*, 58(6):1115, 1987.

[29] M. Fotino. *Rev. Sci. Instrum.*, 64(1):159, 1993.

[30] M. Fotino. *Appl. Phys. Lett.*, 60(23):2935, 1992.

[31] A. J. Nam, A. Teren, T. A. Lusby, and A. J. Melmed. *J. Vac. Sci. Technol. B*, 13(4):1556, 1995.

[32] L. Libioulle, Y. Houbion, and J.-M. Gilles. *Rev. Sci. Instrum.*, 66(1):97, 1995.

[33] J. Lindahl, T. Takanen, and L. Montelius. *J. Vac. Sci. Technol. B*, 16(6):3077, 1998.

[34] R. Wiesendanger. *Scanning Probe Microscopy and Spectroscopy: Methods and Applications*. Cambridge University Press, 1994.

[35] D. Bonnell, editor. *Scanning Probe Microscopy and Spectroscopy: Theory, Techniques, and Applications*. Wiley-VCH, 2nd edition, 2001.

[36] C. J. Chen. *Introduction to Scanning Tunneling Microscopy*. Oxford University Press, 1993.

[37] G. W. Stupian and M. S. Leung. *Rev. Sci. Instrum.*, 60(2):181, 1989.

[38] A. Cricenti, E. Paparazzo, M. A. Scarselli, L. Moretto, and S. Selci. *Rev. Sci. Intrum.*, 65(5):1558, 1994.

[39] A. J. Melmed, R. D. Shull, C. K. Chiang, and H. A. Fowler. *Science*, 239(4836):176, 1988.

[40] G. Binning, H. Rohrer, Ch. Gerber, and E. Weibel. *Phys. Rev. Lett.*, 49(1):57, 1982.

[41] R. J. Colton, S. M. Baker, J. D. Baldeschwieler, and W. J. Kaiser. *Appl. Phys. Lett.*, 51(5):305, 1987.

[42] T. S. Ravi, R. B. Marcus, T. Gmitter, H. H. Busta, and J. T. Niccum. *Appl. Phys. Lett.*, 57(14):1413, 1990.

[43] Y. Akama, E. Nishimura, A. Sakai, and H. Murakami. *J. Vac. Sci. Technol. A*, 8(1):429, 1990.

[44] D. K. Biegelsen, F. A. Ponce, J. C. Tramontana, and S. M. Koch. *Appl. Phys. Lett.*, 50(11):696, 1987.

[45] J. Garnaes, F. Kragh, K. A. Mørch, and A. R. Thölén. *J. Vac. Sci. Technol. A*, 8(1):441, 1990.

[46] E. Paparazzo, L. Moretto, S. Selci, M. Righini, and I. Farné. *Vacuum*, 52(4):421, 1999.

[47] J. Méndez, M. Luna, and A. M. Baró. *Surf. Sci.*, 266:294, 1992.

[48] L. A. Hockett and S. E. Creager. *Rev. Sci. Instrum.*, 64(1):263, 1993.

[49] S. W. H. Yih and C. T. Wang. *Tungsten: Sources, Metallurgy, Properties, and Applications*. Plenum Press, 1979.

[50] K. C. Li and C. Y. Wang. *Tungsten: Its History, Geology, Ore-Dressing, Metallurgy, Chemistry, Analysis, Applications, and Economics*. Reinhold Publishing Corporation, 3rd edition, 1955.

[51] H. S. Kim, M. L. Yu, U. Staufer, L. P. Murray, D. P. Kern, and T. H. P. Chang. *J. Vac. Sci. Technol. B*, 11(6):2327, 1993.

[52] V. T. Binh, A. Piquet, H. Roux, R. Uzan, and M. Drechsler. *J. Phys. E: Sci. Instrum.*, 9(5):377, 1976.

[53] U. Staufer, L. P. Muray, D. P. Kern, and T. H. P. Chang. *J. Vac. Sci. Technol. B*, 9(6):2962, 1991.

[54] J. L. Boling and W. W. Dolan. *J. Appl. Phys.*, 29(3):556, 1958.

[55] V. T. Binh and R. Uzan. *Surf. Sci.*, 179:540, 1987.

[56] V. T. Binh, A. Piquet, H. Roux, R. Uzan, and M. Drechsler. *Surf. Sci.*, 44(2):598, 1974.

[57] O. Albrektsen, H. W. M. Salemink, K. A. Mørch, and A. R. Thölen. *J. Vac. Sci. Technol. B*, 12(6):3187, 1994.

[58] R. Harris. *Nonclassical Physics: Beyond Newton's View.* Addison-Wesley, 1998.

[59] M. P. Marder. *Condensed Matter Physics.* Wiley-Interscience, 2000.

[60] A. T. Hubbard, editor. *The Handbook of Surface Imaging and Visualization.* CRC Press, 1995.

[61] R. H. Fowler and L. Nordheim. *Proc. Roy. Soc. (London) A*, 119(781):173, 1928.

[62] W. Qian, M. R. Scheinfein, and J. C. H. Spence. *J. Appl. Phys.*, 73(11):7041, 1993.

[63] D. Atlan, G. Gardet, V. T. Binh, N. García, and J. J. Sáenz. *Ultramicroscopy*, 42-44:154, 1992.

[64] J. A. Meyer, S. J. Stranick, J. B. Wang, and P. S. Weiss. *Ultramicroscopy*, 42-44:1538, 1992.

[65] G. N. Fursey and D. V. Glazanov. *J. Vac. Sci. Technol. B*, 16(2):910, 1998.

[66] V. T. Binh and J. Marien. *Surf. Sci. Lett.*, 202:L539, 1988.

[67] V. T. Binh and N. García. *Ultramicroscopy*, 42-44:80, 1992.

[68] H. Wengelnik and H. Neddermeyer. *J. Vac. Sci. Technol. A*, 8(1):438, 1990.

[69] V. T. Binh. *J. Microsc.*, 152:355, 1988.

[70] Y. Kuk and P. J. Silverman. *Appl. Phys. Lett.*, 48(23):1597, 1986.

[71] H.-W. Fink. *IBM J. Res. Develop.*, 30(5):460, 1986.

[72] T. Sakurai, A. Sakai, and H. W. Pickering. *Atom-Probe Field Ion Microscopy and Its Applications.* Advances in Electronics and Electron Physics. Academic Press, Inc., 1989.

[73] J. A. Panitz. *J. Phys. E: Sci. Instrum.*, 15(12):1281, 1982.

[74] J. M. Hyde, A. Cerezo, R. P. Setna, P. J. Warren, and G. D. W. Smith. *Appl. Surf. Sci.*, 76/77:382, 1994.

[75] K. Kuroda, S. Hosoki, and T. Komoda. *Scanning Microscopy*, 1(3):911, 1987.

[76] D. G. Brandon. *J. Sci. Instrum.*, 41:373, 1964.

[77] R. W. Newman, R. C. Sanwald, and J. J. Hren. *J. Sci. Instrum.*, 44:828, 1967.

[78] The computer program for the 3-D reconstruction of the tips was written by Mark Orchard-Webb. McGill University, Canada, 2003. orchard@physics.mcgill.ca.

[79] www.povray.org.

[80] O. Nishikawa, M. Tomitori, and F. Katsuki. *Journal of Microscopy*, 152(3):637, 1988.

[81] U. Schmidt, H. Rasch, Th. Fries, F. W. Röllgen, and K. Wandelt. *Surf. Sci.*, 266:249, 1992.